2018

Advanced Controls Of Cyber Physical Energy Systems

Jiajun Duan
Lehigh University

ADVANCED CONTROLS OF CYBER PHYSICAL ENERGY SYSTEMS

by

Jiajun Duan

A Dissertation

Presented to the Graduate and Research Committee

of Lehigh University

in Candidacy for the Degree of

Doctor of Philosophy

in

Electrical Engineering

Lehigh University

May 2018

Approved and recommended for acceptance as a dissertation of Jiajun Duan in partial fulfillment of the requirements for the degree of Doctor of Philosophy.

_____

Date

_____

Dissertation Director

_____

Accepted Date

Committee Members:

_____

Name of Committee Chair

_____

Name of Committee Member

_____

Name of Committee Member

_____

Name of Committee Member

_____

Name of Committee Member

ACKNOWLEDGMENTS

This study would not have been accomplished with the support of many people. I would like to thank my advisor, Dr. Liu, for his continuous and constructive instruction, and for his huge effort on modifying papers with me. I would like to thank my co-advisor Dr. Xu who inspired me to pursue along the line of research, and for his patient teaching me of control theories. I am very thankful for my committee members, Dr. Cheng, Dr. Decker and Dr. Kishore, for their valuable service and guidance.

I would like to thank my family and my friends. I really appreciate the unwavering supports from my parents, Mr. Duan and Ms. Wu, and I am very lucky to be their child. I would like to thank my lover, Ms. Tian, who has be always staying with me for the past five years.

Lastly but certainly not least, I would like to thank everyone in my life that helped me get through difficulties. This work would not be possible without you.

TABLE OF CONTENTS

LIST OF TABLES

LIST OF FIGURES

ABSTRACT

Cyber system is a fairly important component of the energy systems. The network imperfections can significantly reduce the control performance if not be properly treated together with the physical system during the control designs. In the proposed research, the advanced controls of cyber-physical energy systems are explored in depth. The focus of our research is on two typical energy systems including the large-scale smart grid (e.g. wide-area power system) and the smart microgrid (e.g. shipboard power system and inverter-interfaced AC/DC microgrid). In order to proactively reduce the computation and communication burden of the wide-area power systems (WAPSs), an event/self-triggered control method is developed. Besides, a reinforcement learning method is designed to counteract the unavoidable network imperfections of WAPSs such as communication delay and packet dropout with unknown system dynamics. For smart microgrids, various advanced control techniques, e.g., output constrained control, consensus-based control, neuro network and game theory etc., have been successfully applied to improve their physical performance. The proposed control algorithms have been tested through extensive simulations including the real-time simulation, the power-hardware-in-the-loop simulation and on the hardware testbed. Based on the existing work, further research of microgrids will be conducted to develop the improved control algorithms with cyber uncertainties.

INTRODUCTION

1.1 Cyber-Physical Energy Systems

Both cyber and physical systems are fairly important components of the energy systems. The network imperfections can significantly reduce the control performance if not be properly treated together with the physical system uncertainties during the control designs. In the proposed research, the advanced controls of cyber-physical energy systems are explored in depth. The focus of our research is on two typical energy systems including the large-scale smart grids (e.g. wide-area power systems) and the smart microgrids (e.g. shipboard power system and inverter-interfaced AC/DC microgrids). Based on the different characteristics, various advanced control algorithms are developed to improve the overall control performance as well as to address the specific problems of the energy systems.

Traditional damping controllers of wide-area power systems (WAPSs) are not able to solve the inter-area oscillation problem effectively due to lack of global vision. It decreases the power transfer capability and even the stability of WAPSs. The installation of a large number of phasor measurement units (PMUs) brings about system-wide synchronized real-time measurements, which makes the advanced closed-loop control of WAPSs possible. In this research, various advanced control algorithms are developed specifically for wide-area damping control using the globally synchronized PMU data. In order to proactively reduce the communication burden, the event-triggered and self-triggered control algorithms are designed for WAPS. Then, considering unavoidable network imperfections, a reinforcement learning based control algorithm is developed to passively counteract the cyber as well as physical uncertainties.

Considering the complexity and expenses of the large-scale power systems, it is quite challenging to evaluate the proposed control solution on the physical systems. Therefore, the pulsed power loads problem of the shipboard power system (SPS) is studied in the next research. The non-cooperative control problem of onboard pulsed power load is formulated as a two-player zero-sum game. One player is the optimal controller which is designed to

optimize a predefined cost function. The other player is the disturbance that represents the overall damping effect of the system, including that of unmodeled system dynamics. Neurodynamics programming based control design is developed to solve the nonlinear optimal control problem under disturbance. The neural network based control algorithm can achieve the near-optimal control without acknowledge of system dynamics. In addition, the control design can relax the requirements for initially admissible control conditions and predetermined control references. The effectiveness of the proposed algorithm is demonstrated through both software simulation as well as multiple-converter based power hardware-in-the-loop experimentation.

However, the previous research is focused on the secondary control, which produces the system references based on the consideration of stability and economy. The problem of how primary control can track the reference generated by secondary control is ignored. Therefore, the primary control and the secondary control problems of the microgrids are explored. Starting from the simplest microgrid application, i.e. DC microgrids, a decentralized control solution is proposed. Based on the proposed output constrained control algorithm, the terminal bus voltage can always stay within the user-defined time-varying bounds. Next, several different distributed control solutions are proposed for AC microgrid. Conventional localized controllers of microgrid unavoidably introduce large transient line currents, which may trigger false protection even under normal operating conditions. The proposed primary controller cannot only realize a promising voltage and frequency regulation, but also suppress line current surge during the transient time. And the secondary controller can realize the fair load sharing in a distributed way.

1.2 Thesis Outline

The contents are organized as follows: In chapter 2, several wide-area damping control algorithms are developed for WAPS using PMU data. In chapter 3, the pulsed power load problem of SPS is solved using the neuro-network based zero-sum game theory under unknown system dynamics. In chapter 4, a performance guaranteed control method is developed for DC microgrids to realize the output constraint control performance. In chapter 5, the control problems of inverter-interfaced AC microgrids are studied to better improve the overall system performance. Finally, remarks are concluded in chapter 6.

WIDE-AREA POWER SYSTEM CONTROL

2.1 Problem Description

With the expansion of power grid, Wide-Area Power Systems (WAPSs) are established by interconnecting the regional power systems of different areas [1]. Typical examples of WAPSs include the Western Electricity Coordinating Council (WECC) system in the US [2], [3] and the South and Central China Grids [4]. The main advantages of the WAPSs include the establishment of mutual backup, the enhancement of redundancy, and increased capability and efficiency of generation allocation [3, 5]. However, the WAPSs are difficult to manage due to complexity and uncertainty.

In the past years, considerable investment has been used to develop the Wide-Area Measurement Systems (WAMS). A massive number of Phasor Measurement Units (PMUs) have been deployed in WAPSs all over the world [5, 6]. The systematic installation of synchronized PMUs makes the advanced real-time control of WAPSs possible. However, the complexities of physical and cyber systems of WAPS make the hardware investment hard to accommodate the application of advanced wide-area control sufficiently [7]. Instead of closed-loop control, open-loop monitoring remains to be the major application of the PMUs at present [5]. WAMS still has large room and potentials to be exploited.

As one of the most important problems with WAPSs, the inter-area oscillations degrade the power transfer capability and even cause system instability. Insufficient damping effort could result in system collapse with severe economic losses, such as the large-scale power outage accident of the WECC system on August 10, 1996 [3]. The traditional solution to this problem has been to install power system stabilizers (PSSs). Conventional PSSs (CPSSs) are designed based on phase compensation theory and introduced as lead-lag compensators [8]. Due to the lack of global vision and difficulty with the parameter tuning, such CPSSs cannot provide satisfactory damping performance [9]. The deployment of WAMS provides control center with the real-time global synchronized measurements that can be used to perform advanced damping control. In this section, in order to proactively reduce the communication burden, the event-triggered and self-triggered control algorithms are designed for WAPS. Then, considering unavoidable network imperfections,

a reinforcement learning based control algorithm is developed to passively counteract the cyber as well as physical uncertainties.

2.2 Introduction to Wide-Area Power System

The interconnected WAPSs have several advantages. First, the reliability of the overall system can be improved. If some contingencies occur in one subsystem, it has a better chance to survive under supports of another subsystem(s) [2]. Second, the energy efficiency of the overall system can be enhanced. Since a subsystem could receive low-cost power supply from other subsystems, the overall operation cost of the system can be reduced [10]. Third, the flexibility of the power grid can be increased. Because subsystems can work autonomously similar to micro-grid power systems, the inter-connected tie lines can be intentionally disconnected under extreme conditions to avoid the spreading of wide-area blackouts [3].

However, WAPSs are difficult to control due to the wide coverage area and complex interactions among subsystems. Traditional power systems are controlled based on local information and tend to make myopic decisions. The installation of phasor measurement units (PMUs) brings the real-time global vision to control centers for wide-area monitoring and controlling. Due to the difficulty with closed-loop control of the complex WAPS, the development of wide-area control schemes has been lagging the hardware investment. So far the major application of PMUs is still on the open-loop wide-area monitoring and diagnosis. It is necessary to study the challenging closed-loop control problems of the WAPS and to unlock the potentials of the installed PMUs.

2.3 Linearized Modeling of Wide-Area Power Systems

Effective modeling of WAPS is challenging due to its complexity. To simplify wide-area control design, a subsystem (regional power system) can be modeled as an aggregated generator based on the coherent theory [11]. Multiple such subsystems are then connected together to form a WAPS. Extensive phasor measurement units (PMUs) are deployed for grid-wide synchronized measurement, which is used for wide-area monitoring and control.

The WAPS model used in the control design is modified based on the small-signal model proposed by Chakraborty et al. [3, 5]. This WAPS model integrates the dynamics of synchronous generators (SGs), static loads, and transmission lines. An SG i^{th} with statistic governor and exacter can be presented as

$$\dot{\delta}_i(t) = \omega_i(t) - \omega_s \tag{1.1}$$

$$\dot{\omega}_i(t) = \frac{1}{M_i}\left[P_{Mi} - T_{di}(\omega_i(t) - \omega_s) - \frac{E_i V_i}{X'_{di}+X_{Ti}}\sin(\delta_i - \theta_i)\right] \tag{1.2}$$

$$\dot{E}_i(t) = \frac{1}{\tau_i}\left[-\frac{X_{di}}{X'_{di}}E_i - \frac{X_{di}-X'_{di}}{X'_{di}-X_{Ti}}V_i\sin(\delta_i - \theta_i) + E_{fi}\right] \tag{1.3}$$

where: δ_i, ω_i and E_i are the rotor angle, rotor speed and quadrature-axis electrical magnetic flew of the generator, respectively; X_{di} and, X_{di}' are salient and transient reactance of generator along the direct-axis; X_{Ti} is the impedance of generator transformer. M_i , T_{di}, and τ_i are the constant of generator inertia, generator damping and excitation time; the control variables are the field voltage E_{fi}; P_{Mi} is the mechanical power input of turbine; ω_s is the synchronous rotor speed. At bus i, the voltage is denoted as $V_i\angle\,\theta_i$ where V_i is the voltage and θ_i is the angle.

By using Kirchhoff Current Law (KCL) at the load bus and the generation bus respectively

$$YV = Y_E E + LI_L \tag{1.4}$$

where I_L=*col*(I_{Li}) is the column of load currents (col means column), E=*col*(E_i) and V=*col*(V_i). Y is the admittance matrix; Y_E=*diag*(X_{di}'+X_{Ti})$^{-1}$ is the diagonal matrix of internal admittances of SGs and transformers; L is the vector of load connection, the element is 1 if the load is connected, otherwise 0. Furthermore, V can be represented as

$$V = Y^{-1}(Y_E E + LI_L) \tag{1.5}$$

Actually, each component in (1.5) can be represented by a real part and imaginary part as

$$\begin{cases} V = V_R + jV_I \\ E = E_R + jE_I \\ I_L = I_{LR} + jI_{LI} \end{cases} \tag{1.6}$$

If linearize (1.6), one can have

$$\begin{cases} \Delta V_{Ri} = \Delta V_i\cos(\theta_{i0}) - \Delta\theta_i V_{i0}\sin(\theta_{i0}) \\ \Delta V_{Ii} = \Delta V_i\sin(\theta_{i0}) + \Delta\theta_i V_{i0}\cos(\theta_{i0}) \\ \Delta E_{Ri} = \Delta E_i\cos(\delta_{i0}) - \Delta\delta_i E_{i0}\sin(\delta_{i0}) \\ \Delta E_{Ii} = \Delta E_i\sin(\delta_{i0}) + \Delta\delta_i E_{i0}\cos(\delta_{i0}) \end{cases} \tag{1.7}$$

Substituting (1.6) and (1.7) back into (1.5), the linearized terminal bus voltage ΔV and its phase angle $\Delta\theta$ can be represented as

$$\begin{cases}\Delta V_i = F_{1i}\Delta E + F_{2i}\Delta\delta + I_{1i} \\ \Delta\theta_i = F_{3i}\Delta E + F_{4i}\Delta\delta + I_{2i}\end{cases} \tag{1.8}$$

where F_i is the matrix associated with initial values (E_{i0}, δ_{i0}, V_{i0} and θ_{i0}) and its accurate expression can be found in [7], while L_i is a linear function of the load current deviation ΔI_L.

Then, linearize (1.1)-(1.3) and substitute (1.8), one can have

$$\Delta\dot{\delta}_i(t) = \Delta\omega_i(t) \tag{1.9}$$

$$\Delta\dot{\omega}_i(t) = \frac{1}{M_i}\begin{bmatrix}\Delta P_{Mi}(t) - T_{di}\Delta\omega_i(t) - C_{1i}\Delta E_i(t) + (C_{2i}F_{1i} + C_{4i}F_{3i})\Delta E(t) \\ -C_{3i}\Delta\delta_i(t) + (C_{2i}F_{2i} + C_{4i}F_{4i})\Delta\delta(t) + C_{2i}L_1 + C_{4i}L_2\end{bmatrix} \tag{1.10}$$

$$\Delta\dot{E}_i(t) = \frac{1}{\tau_i}\begin{bmatrix}a_i\Delta E_i(t) - (b_iF_{1i} + c_iF_{3i})\Delta E(t) - c_i\Delta\delta_i(t) \\ +(b_iF_{2i} + c_iF_{4i})\Delta\delta(t) + \Delta E_{fi}(t) + b_iL_1 + c_iL_2\end{bmatrix} \tag{1.11}$$

where

$$\begin{cases} C_{1i} = (V_{i0}/X'_{di})\sin(\delta_{i0} - \theta_{i0}) \\ C_{2i} = (E_{i0}/X'_{di})\sin(\delta_{i0} - \theta_{i0}) \\ C_{3i} = (E_{i0}V_{i0}/X'_{di})\cos(\delta_{i0} - \theta_{i0}) \\ C_{4i} = -C_{3i}\end{cases}, \begin{cases} a_i = -(X_{di}/X'_{di}) \\ b_i = [(X_{di} - X'_{di})/(X'_{di} - X_{Ti})]\cos(\delta_{i0} - \theta_{i0}) \\ c_i = V_{i0}[(X_{di} - X'_{di})/(X'_{di} - X_{Ti})]\sin(\delta_{i0} - \theta_{i0})\end{cases}$$

Finally, the whole system of (1.9)-(1.11) can be represented by a state space function (eq. 1.1-1.3 in the paper) as

$$\Delta\dot{x}(t) = A\Delta x(t) + B\Delta u(t) + D(t) \tag{1.12}$$

where D is unknown disturbances due to the load current (L_1 and L_2).

Since an SG's internal states ($\Delta\delta$ and ΔE) are not directly measurable, PMUs are usually deployed on generator terminal buses to measure V, θ, and f. According to the [7], the following relationship exists between the PMUs measurements ($\Delta\theta$, Δf and ΔV) and SG's states ($\Delta\delta$, $\Delta\omega$, and ΔE).

$$y(t) = \begin{bmatrix}\Delta V(t) \\ \Delta\theta(t) \\ \Delta f(t)\end{bmatrix} = \begin{bmatrix}F_1 & F_2 & 0 \\ F_3 & F_4 & 0 \\ 0 & 0 & \omega_s G\end{bmatrix}\begin{bmatrix}\Delta E(t) \\ \Delta\delta(t) \\ \Delta\omega(t)\end{bmatrix} = C\Delta x(t) \tag{1.13}$$

where $C = \begin{bmatrix}F_1 & F_2 & 0 \\ F_3 & F_4 & 0 \\ 0 & 0 & \omega_s G\end{bmatrix}$ is a non-singular square matrix with F_i and G being constant blocks calculated based on the equilibrium operating point x_0 and parameters of SGs. The detailed expressions of C is omitted in this paper due to the limitation in space, interested

readers can refer to the papers [5, 7]. Because the square matrix C is constant and invertible, the states $\Delta x(t)$ can be estimated by using output multiplying a constant gain as $\Delta x(t) = C^{-1}\Delta y(t)$. Thus, the state space representation in equation (1.12) can be rewritten using outputs $\Delta y(t)$ as

$$\Delta \dot{y}(t) = A_y \Delta y(t) + B_y \Delta u(t) + D_y \tag{1.14}$$

where $A_y = CAC^{-1} \subset \mathbb{R}^{n\times n}$ and $B_y = CB \subset \mathbb{R}^{n\times m}$.

In addition, the linearized dynamics of a non-reheat steam turbine is also considered with second-order functions as [12]

$$\Delta \dot{P}_{Mi}(t) = \frac{1}{T_{CHi}}[\Delta P_{Mi}(t) + \Delta P_{SVi}(t)] \tag{1.15}$$

$$\Delta \dot{P}_{SVi}(t) = \frac{1}{T_{SVi}}[-\Delta P_{SVi}(t) + \Delta P_{Ci}(t) - \Delta \omega_i(t)/R_{Di}\,\omega_s] \tag{1.16}$$

where R_{Di} is the speed regulation quantity; P_{Ci} is the control input of the governor, namely the power change setting; P_{SVi} is the steam valve position; T_{SVi} and T_{CHi} are the re-heater main inlet volumes and steam chest time constants, respectively.

Based on the dynamics in (1.15) and (1.16), a compensator can be designed to counteract the delay of the turbine response as shown in figure 2.1.

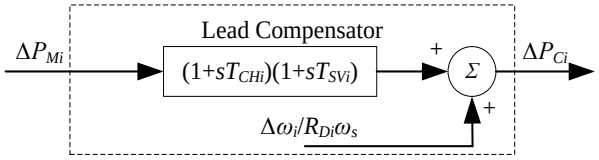

Figure 2.1 Lead compensator for the turbine

2.4 Event-Triggered and Self-Triggered Controls

Currently, the periodic control schemes are widely used in the traditional power systems [13-16]. Such periodic control schemes require expensive computation cost and large communication bandwidth to support the data exchanges among PMUs, controllers, and actuators. To meet the ever-increasing expectations and requirements of the smart grid, more and more control functions will be added. If periodic control schemes continue to be used, WAPSs might eventually be overloaded due to its limited computation and network resources [17].

In order to reduce the communication requirements, the aperiodic control techniques, i.e. the event-triggered and the self-triggered controls, can be introduced. The flow chart of the

two control techniques is illustrated in figure 2.2. The basic idea behind them is to update control signals only when certain conditions are triggered. Certain conditions are designed to strictly maintain the system stability [18]. During the time period without control updating, previously applied control signal in the actuator is kept being used. In this way, only necessary communications are incurred between the control center and the actuators.

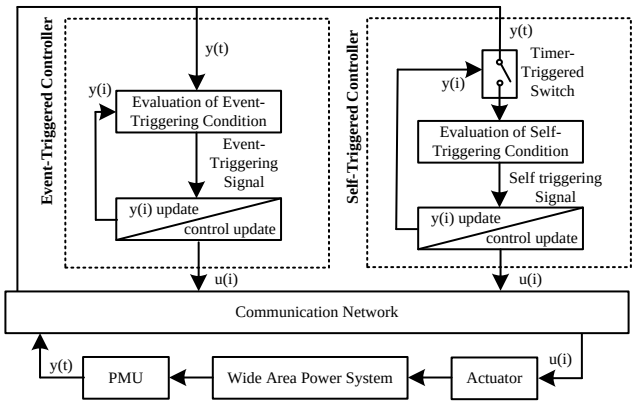

Figure 2.2 Illustration of ZOH event-triggered or self-triggered controls systems

As shown in figure 2.2, both controllers use measurements of PMUs to generate control signals for the actuators implementation. For event-triggered control, a previous system measurement $y(i)$ is recorded and compared with the real-time measurement $y(t)$ continuously. If the deviation between the two signals is larger than a predefined threshold, an event will be triggered. Under such conditions, both system output $y(i)$ and control signal $u(i)$ will be updated. For self-triggered control, the triggering signal is a timer, whose setting is calculated based on the previous system measurement $y(i)$ and the stability requirement. The operations after the self-triggering condition being triggered are similar to that of event-triggered control.

The objectives of both control techniques are to maintain the stability of system while minimizing computation and communication requirements. The major difference is with confidence or assumptions of systems operating conditions. Self-triggered control assumes system's operating condition does not change abruptly and tries to maximize updating intervals. In comparison, event-triggered control does not make assumptions about operating conditions but takes action whenever necessary. Statically, self-triggered control has lower requirements for communication but might not adapt to severe changes in system operating conditions in a timely manner. While event-triggered control can provide a

timely response but requires continuous monitoring of systems operating conditions. For the specific wide-area damping control application that assumes the availability of WAMS, the requirement of online monitoring of event-triggered control can be easily accommodated. Based on above analysis, one can see that the event-triggered and the self-triggered control techniques have certain advantages and disadvantages of themselves.

Because the inaccuracies introduced during modeling, linearization and measurement approximation are unavoidable, they should be addressed properly. During the control design, the following linearized dynamic model for wide-area control design can be represented as

$$\Delta\dot{y}(t) = \left[A_y + \Delta A(t)\right]\Delta y(t) + \left[B_y + \Delta B(t)\right]\Delta u(t) + D(t) \tag{1.17}$$

where $D(t)$ denotes the time-varying disturbances, $\Delta A(t)$ and $\Delta B(t)$ represent the time-varying uncertainties in the system. It should be mentioned that the formulation of equation (1.17) has been widely used to present parameter uncertainties in many physical systems [19]. Besides, uncertainties and disturbances are assumed to be bounded, i.e. $\|\Delta A(t)\| \leq a_u$, $\|\Delta B(t)\| \leq b_u$ and $\|D(t)\| \leq D_M$ [18]. The introduction of uncertainties and disturbances makes the linearized model applicable to a wider range of operating conditions. However, due to uncertainties, the control design becomes more difficult and challenging. To overcome this deficiency, novel ZOH event-triggered and self-triggered control designs will be developed.

2.5 WAPS with ZOH Event-Triggered and Self-Triggered Controls

In this section, novel ZOH event-triggered and self-triggered wide-area control algorithms which can maintain WAPS stability under uncertainties and disturbances are presented. First, the event-triggering condition under ideal case (i.e. system without uncertainties and disturbances) is derived. Then, a more realistic case (i.e. a system with uncertainties and disturbances) are considered to design event-triggered control and self-triggered control separately.

The proposed ZOH control law can be formulated as

$$\Delta u(t) = \begin{cases} K\Delta y(i) & \text{event or time condition is not triggered} \\ K\Delta y(t) & \text{event or time condition is triggered} \end{cases}, \; 0 < iT_s \leq t \tag{1.18}$$

where T_s is the sampling time, and K is the feedback control gain so that the closed-loop system matrix $(A_y - B_y K)$ are negative definite. If the event triggering condition or time triggering condition is activated, control signals will be adjusted using the most recent measurements. Otherwise, previously updated control is used until the condition is triggered again. For linear systems with known system dynamics, K can be obtained by solving the following Lyapunov equation (1.19) as proposed by [20].

$$(A_y + B_y K)^T P + P(A_y + B_y K) = -Q \tag{1.19}$$

where Q and P are positive definite matrices.

Theorem 1 (Event-triggering Condition under Ideal Case): Under the ideal situation, i.e. the system dynamics are precisely known, the event-triggering condition can be designed as

$$\|e(t)\| < \gamma_{ideal} \|\Delta y(t)\| \tag{1.20}$$

where $e(t) = \Delta y(i) - \Delta y(t)$ is the error between the previously recorded output deviation $\Delta y(i)$ and the current output deviation $\Delta y(t)$, $\gamma_{ideal} = \sigma \frac{q}{2[\|K^T B_y^T P\|]}$ is the threshold coefficient with $q = \lambda_{min}(Q)$ being the minimum eigenvalues of Q. σ is designed parameter which satisfy $0 < \sigma < 1$. Also, Q and P can be obtained by solving Lyapunov equation given in (1.19)

Proof of Theorem 1: For the simplicity, the subscript of time t is omitted in this part. Besides, some derivation processes are excluded due to the page limit. Consider the Lyapunov function candidate given as $L(\Delta y) = \Delta y^T P \Delta y$ where P satisfies the Lyapunov equation (1.19). Taking the first derivative, we have

$$\dot{L}(\Delta y) = \Delta \dot{y}^T P \Delta y + \Delta y^T P \Delta \dot{y} \tag{1.21}$$

According to the system state space representation derived in (1.14) without considering disturbances D_y, (1.21) can be represented as

$$\dot{L}(\Delta y) = \left[A_y \Delta y + B_y \Delta u\right]^T P \Delta y + \Delta y^T P \left[A_y \Delta y + B_y \Delta u\right] \tag{1.22}$$

Recall the event-triggered control designed in (1.18), (1.22) can be expressed as

$$\dot{L}(\Delta y) = \left[A_y \Delta y + B_y K(e + \Delta y)\right]^T P \Delta y + \Delta y^T P \left[A_y \Delta y + B_y (e + \Delta y)\right]$$
$$\leq \Delta y^T \left(A_y + B_y K\right)^T P \Delta y + \Delta y^T P \left(A_y + B_y K\right) \Delta y + e^T K^T B_y^T P \Delta y + \Delta y^T P B_y K e$$

$$\leq \Delta y^T \left[\left(A_y + B_y K\right)^T P + P\left(A_y + B_y K\right) \right] \Delta y + e^T K^T B_y^T P \Delta y + \Delta y^T P B_y K e$$

$$\leq \Delta y^T Q \Delta y + e^T K^T B_y^T P \Delta y + \Delta y^T P B_y K e$$

$$\leq -q\|\Delta y\|^2 + \left\|2Pe^T B_y K\right\| \|\Delta y\| \|e\| \quad (1.23)$$

According to the event-triggering condition derived in (1.20), we have

$$\dot{L}(\Delta y) \leq -q\|\Delta y\| + \gamma_{ideal}\left\|2Pe^T B_y K\right\| \|\Delta y\|^2 \leq -q\|\Delta y\|^2 + \sigma q\|\Delta y\|^2 \leq -(1-\sigma)\|\Delta y\|^2 \quad (1.24)$$

Since $0 < \sigma < 1$, the derived event-triggering condition can guarantee that the system is asymptotically stable. ◊

However, in practical, system uncertainties and disturbances always exist. They could affect the system performance and complicate the event-triggering condition design significantly. Therefore, the bounds of system uncertainties and disturbances (a_u, b_u and D_M) are used to design the event-triggering and self-triggering conditions. For linear systems subjecting to disturbances and uncertainties, i.e. those can be represented with equation (1.17), the event-triggering condition defined as equation (1.20) has to be updated to maintain stability.

2.5.1 Design of Event-Triggering Condition under Uncertainties and Disturbances

Theorem 2 (Event-triggering Condition under Realistic Case): Inspired by the stability analysis in [21], the ZOH event-triggered control in equation (1.18) for WAPS formulated as equation (1.17) can guarantee the system state deviations being uniformly ultimately bounded (UUB) under the event-triggering condition of equation (1.25) as

$$\|e(t)\| < \gamma_T \|\Delta y(t)\| \quad (1.25)$$

where $\gamma_T = \sigma \frac{(q-\Phi)}{2[\|K^T B_y^T P\| + \|K^T b_u P\|]}$ is the proposed threshold coefficient with Φ and q defined according to $\Phi = 2\|P\|(a_u + b_u \|K\|)$ and $q = \lambda_{min}(Q)$, respectively. To maintain the stability of control system, the following condition in terms of $P, Q, K, a_u, and\ b_u$ should be satisfied:

$$\Phi < q \quad (1.26)$$

The boundedness of $\Delta y(t)$ is represented as equation (1.27),

$$\|\Delta y(t)\| \leq \sqrt{\frac{b_e}{(1-\sigma)(q-\Phi)}} \tag{1.27}$$

where $b_e > 0$ is defined as $b_e = \frac{2}{\sigma(q-\Phi)} D_M \|P\|$.

Proof of Theorem 2: Selecting the Lyapunov function candidate as $L(\Delta y) = \Delta y^T P \Delta y$ where P satisfies the Lyapunov equation (1.19). According to the system state space representation derived in (1.17), taking the first derivative, we have

$$\begin{aligned} \dot{L}(\Delta y) &= \left[\left(A_y + \Delta A\right)\Delta y + \left(B_y + \Delta B\right)\Delta u + D\right]^T P \Delta y \\ &+ \Delta y^T P\left[\left(A_y + \Delta A\right)\Delta y + \left(B_y + \Delta B\right)\Delta u + D\right] \end{aligned} \tag{1.28}$$

Recall the event-triggered control designed in (1.18) in the paper, (1.28) can be expressed as

$$\begin{aligned} \dot{L}(\Delta y) &= \left[\left(A_y + \Delta A\right)\Delta y + \left(B_y + \Delta B\right)Ke + \left(B_y + \Delta B\right)K\Delta y + D\right]^T P \Delta y \\ &+ \Delta y^T P\left[\left(A_y + \Delta A\right)\Delta y + \left(B_y + \Delta B\right)Ke + \left(B_y + \Delta B\right)K\Delta y + D\right] \\ &\leq \Delta y^T Q \Delta y + \Delta y^T (\Delta A + \Delta B K)^T P \Delta y + \Delta y^T P (\Delta A + \Delta B K)\Delta y + e^T K^T \left(B_y + \Delta B\right)^T P \Delta y \\ &+ \Delta y^T P\left(B_y + \Delta B\right)Ke + 2D_M\|P\| \\ &\leq -q\|\Delta y\|^2 + 2\|P\|(a_u + b_u\|K\|)\|\Delta y\|^2 + \left\|2PB_yK\right\|\|\Delta y\|\|e\| \\ &+ \|2P\Delta BK\|\|\Delta y\|\|e\| + 2D_M\|P\| \end{aligned} \tag{1.29}$$

According to the event-triggering condition derived in (1.25) in the paper, we have

$$\begin{aligned} \dot{L}(\Delta y) &\leq -q\|\Delta y\|^2 + 2\|P\|(a_u + b_u\|K\|)\|\Delta y\|^2 + \gamma_T\left(\left\|2PB_yK\right\| + \|2P\Delta BK\|\right)\|\Delta y\|^2 \\ &\quad + 2D_M\|P\| \\ &\leq -(q-\Phi)\|\Delta y\|^2 + \gamma_T\left(\left\|2PB_yK\right\| + \|2P\Delta BK\|\right)\|\Delta y\|^2 + 2D_M\|P\| \\ &\leq -(1-\sigma)(q-\Phi)\|\Delta y\|^2 + b_e \end{aligned} \tag{1.30}$$

Since $0 < \sigma < 1$ and $\Phi <$ q, the derived event-triggering condition can guarantee that the uncertain system is UUB with bounds given in (1.27) in the paper. ◊

2.5.2 Design of Self-triggering Condition under Uncertainties and Disturbances

Based on equation (1.17), the relationship between $\Delta y(t)$ and$\Delta y(i)$ can be represented as equation (1.31).

$$e(t) = \Delta y(i) - \Delta y(t) = -\int_i^{i+\Delta t} \{ [A_y + \Delta A(s)]\, \Delta y(s) + [B_y + \Delta B(s)]\, \Delta u(s) + D(s) \}\, ds$$

$$\cong \{ [A_y + \Delta A(i)]\, \Delta y(i) + [B_y + \Delta B(i)]\, \Delta u(i) + D(i) \} \Delta t \tag{1.31}$$

According to equation (1.31), one can have

$$\begin{cases} \|e(t)\| = \| \{ [A_y + \Delta A(i)]\, \Delta y(i) + [B_y + \Delta B(i)]\, \Delta u(i) + D(i) \} \| \|\Delta t\| \\ \|\Delta y(t)\| = \|\Delta y(i)\| - \| \{ [A_y + \Delta A(i)]\, \Delta y(i) + [B_y + \Delta B(i)]\, \Delta u(i) + D(i) \} \| \|\Delta t\| \end{cases}$$

Based on the event-triggering condition of equation (1.25), the self-triggering condition can be derived as

$$\Delta t < \frac{\gamma_T \|\Delta y(i)\|}{(1-\gamma_T) \| [A_y + a_u]\, \Delta y(i) + [B_y + b_u]\, \Delta u(i) + D_M \|} \tag{1.32}$$

Due to the existence of model uncertainties and disturbances, asymptotic stability cannot be realized. The control accuracy, i.e. the bound of $\Delta y(t)$, is decided by the extent of model accuracy and magnitude of disturbance. During control implementation, the designed parameters P and Q can be selected based on the estimation of $\Delta A(t)$ and $\Delta B(t)$ firstly. Then, control gain K is calculated according to (1.19) together with selected P and Q, practical $\Delta A(t)$ and $\Delta B(t)$ can be used to check the validity of equation (1.26). If needed, P, Q and K can be redesigned.

Because the difficulty with bound estimation of $\Delta A(t)$ and $\Delta B(t)$, it is not easy to decide the best triggering condition accurately, i.e. the maximum interval between instants of time when the two sequential conditions get triggered. In order to maintain the stability over a wide range of operating conditions, more stringent triggering condition (smaller triggering interval) can be selected. The triggering interval increases with the increase of certainty and accuracy of model. The design of event-triggering and self-triggering conditions are trade-off between stability confidence and communication requirement. The existence of nonzero lower bound of the event-triggering interval can be proven similar as the work of [22].

2.6 Simulation Studies of Event-Triggered and Self-Triggered Controls

It is a common sense that the actual model of a large-scale power system is very complex and highly nonlinear. Due to the complexity, it is difficult to obtain an accurate model of

such system. An accurate model is desirable for simulation study but might be inconvenient for controller design. To design a simple yet effective algorithm, model simplification is necessary. However, the algorithm based on the simplified model must be tested with more accurate and detailed model to estimate its real-world performance.

In order to evaluate the performance of the linear-based control designs, they are tested with both linearized model and detailed nonlinear WAPS models, i.e. the Kundur model [11]. As introduced earlier, this model has been extensively used to test new algorithms and to analyze practical power systems. The implementation diagram of the proposed control algorithm is illustrated in figure 2.3. Wide-area measurements (i.e. voltage phase angle θ, rotor speed f and generator terminal voltage V) are measured using PMUs. The sampling interval T_s is 0.1s. The central controller, which implements the event-triggered or self-triggered algorithm separately, decides when to update the global measurements and the control signals.

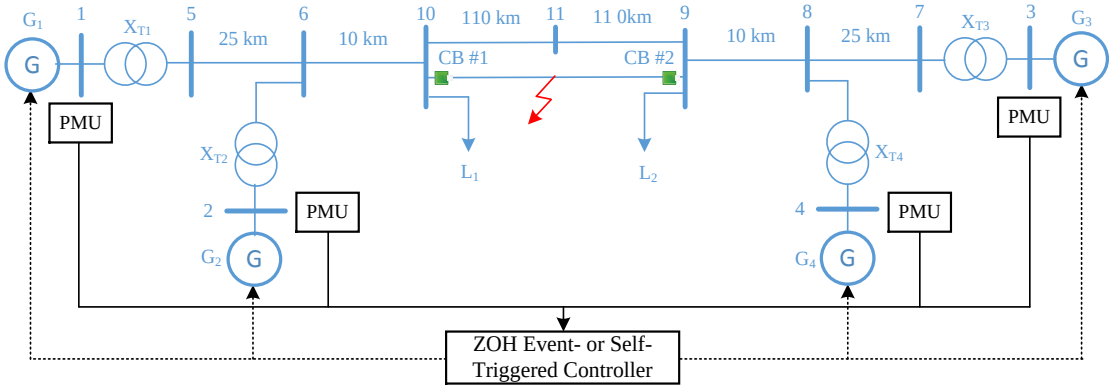

Figure 2.3 Implementation of the proposed controller with the 4 generator model

2.6.1 Simulation Results with Linearized Model

The control algorithm is designed based on the linearized model. However, the designed controller uses real-world measurements during implementation. Due to the limited accuracy of the linearized model, the real-world measurements deviate from the controller's expectation predicted from the linearized model. To counteract the mismatch between the predicted and measured data (the inaccuracy of the linearized model), up to 5% parameter deviations ($\Delta A(t)$ and $\Delta B(t)$) of the linearized system parameter matrixes are simulated. In addition, up to 5% disturbance ($D(t)$) is simulated to investigate the effectiveness of the designed algorithm under small and continuous load fluctuations. For

initialization, small random noises are also added to system states to further disrupt the system.

The damping performance of the event-triggered control design under such conditions is illustrated in Figure 2.4. Among the three plots, Figure 2.4(a) shows the response of bus voltage phase angle deviation ($\Delta\theta$), Figure 3(b) shows the response of frequency deviation (Δf), and Figure 2.4(c) shows the response of terminal bus voltage deviation (ΔV), all in per-unit values. Due to the time-varying system uncertainties and load changes, there are always small oscillations in the bus voltage phase angel deviations, frequency deviations, and terminal bus voltage deviations. Considering the units used in figures are per unit values, the oscillations are reasonably small and acceptable.

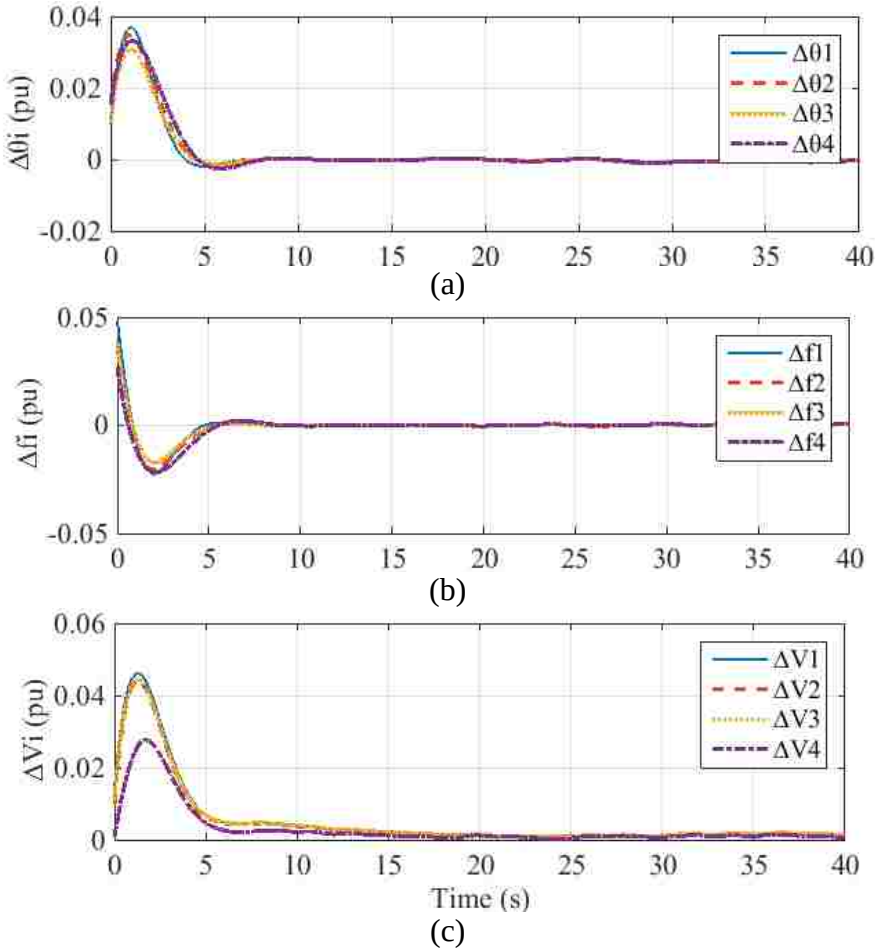

Figure 2.4 Simulation results of the proposed event-triggered controller with linearized model: (a). Phase angle deviation ($\Delta\theta$); (b). Frequency deviations (Δf); (c). Terminal bus voltage deviations (ΔV)

The control signal responses of event-triggered control are illustrated in figure 2.5. Since the control responses of the four SGs are similar, only the control signals (ΔE_{f1} and ΔP_{m1}) of SG #1 are plotted. It can be seen that the control signals also oscillate around zero due to model parameter inaccuracy and continuous load fluctuations. Because of the small size of disturbance, the control actions are not triggered continuously. Previous control signals are held fixed until control is triggered again. It is the reason that step changes of the control signals can be observed.

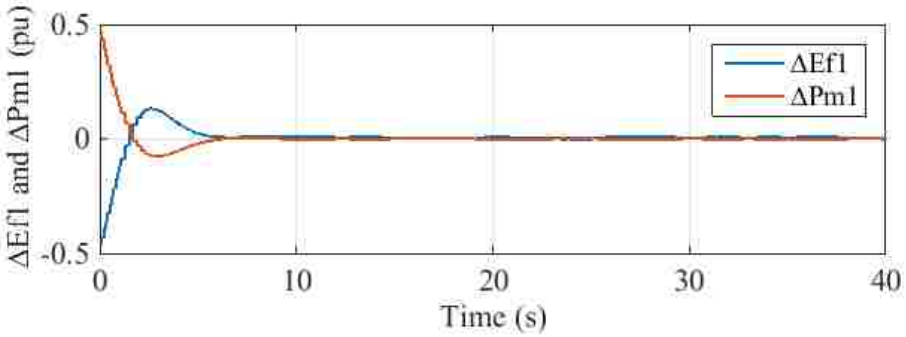

Figure 2.5 Wide-area damping control signals of generator #1 with event-triggered controller (adjustments of field voltage and mechanical power input)

Similarly, the damping performance of the self-triggered control design under same conditions is presented in Figure 2.6. Among the five plots, Figure 2.6(a) shows the response of voltage phase angle deviation ($\Delta\theta$), Figure 2.6(b) shows the response of frequency deviation (Δf), and Figure 2.6(c) shows the response of terminal bus voltage deviation (ΔV), all in per-unit values. The control signal responses of SG #1 are illustrated in Figure 2.7.

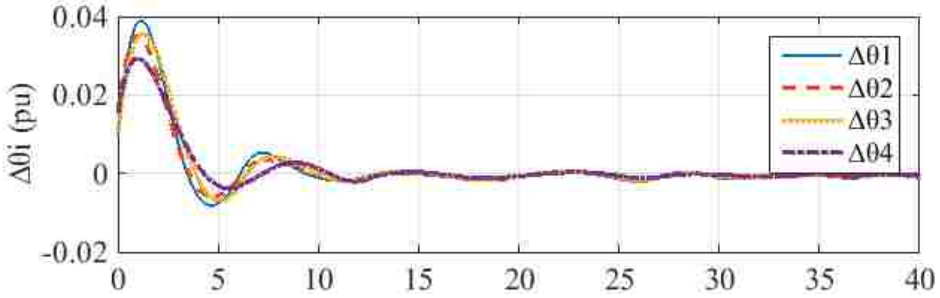

(a)

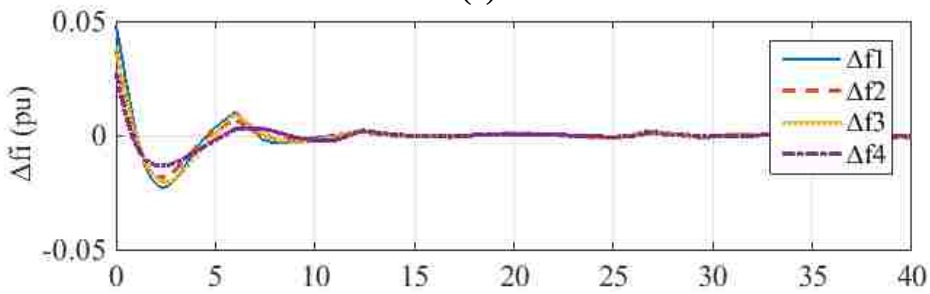

(b)

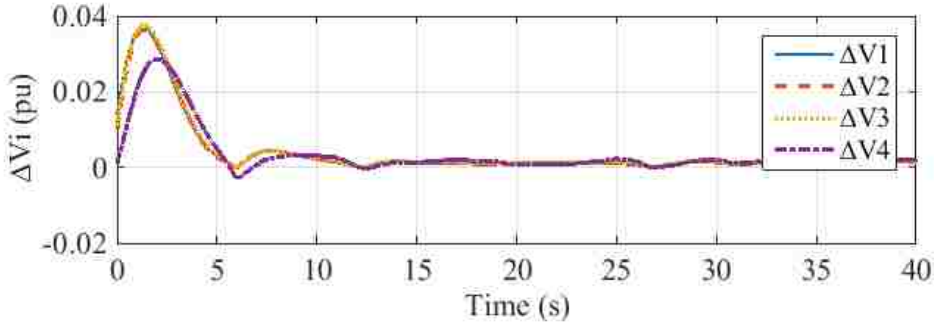

(c)

Figure 2.6 Simulation results of the proposed self-triggered controller with linearized model: (a). Phase angle deviation ($\Delta\theta$); (b). Frequency deviations (Δf); (c). Terminal bus voltage deviations (ΔV)

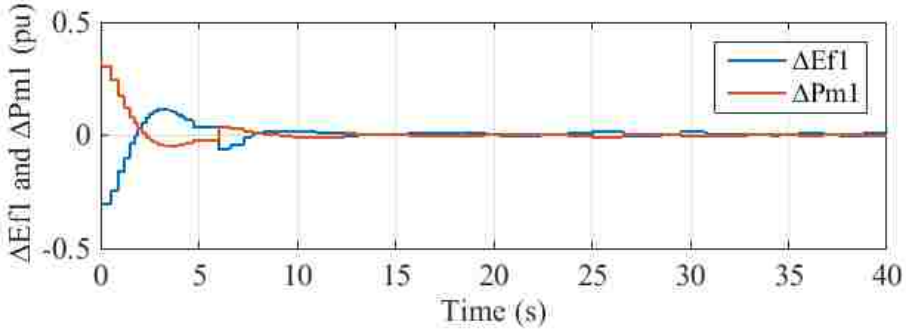

Figure 2.7 Wide-area damping control signals of generator #1 with self-triggered controller (adjustments of field voltage and mechanical power input)

The computational effort comparison among continuously-updated control scheme, the event-triggered control scheme and self-triggered control scheme is visualized in figure 2.8,

which shows the accumulated numbers of control updates at different instants of time. Since the time interval T_s is set up as 0.1 seconds for periodic control, the total numbers of control updates of the continuously-updated control increase linearly from 0 to 400 after 40 seconds. In comparison, the response of event-triggered control increases slowly after the control system is stabilized within a small region from figure 2.8, it is clear to see the benefit of event-triggered or self-triggered control designs in term of communications savings. It should be noted that because the self-triggered controller calculates the next triggering time based on a predefined system model, it can usually save more communications than an event-triggered controller. But the damping performance of self-triggered controller may degrade if the system is suffering big time-varying disturbances.

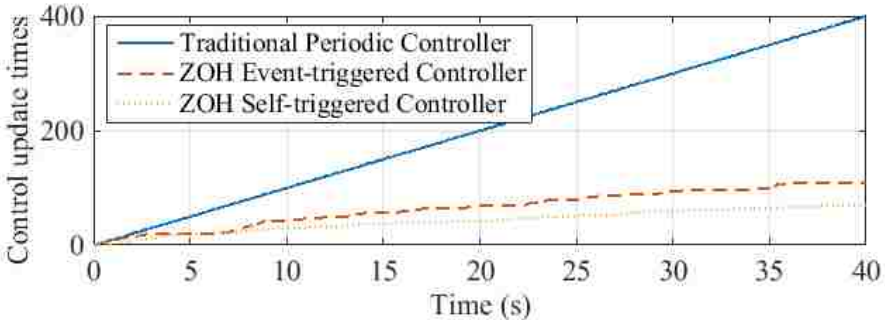

Figure 2.8 The accumulated numbers of control updates of continuously-updated control, event-triggered control and self-triggered control

2.6.2 Simulation Results with Nonlinear Detailed Model

To evaluate the performance of the proposed event-triggered and self-triggered controllers in a real application, the algorithms are tested with the detailed model of WAPS. The specific objectives include testing the algorithm under large disturbance and comparing its performance against well-tuned CPSSs. The Simulink model that comes with the SimPowerSystem™ toolbox for inter-area oscillations is used for simulation studies. The implantation diagram of the proposed control algorithms with the detailed WAPS model is illustrated in figure 2.9.

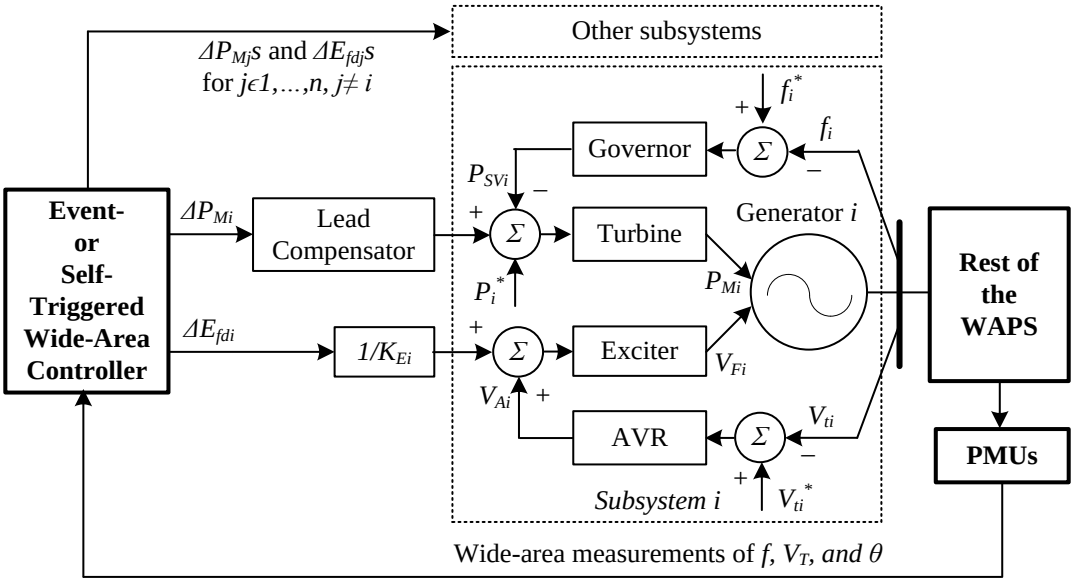

Figure 2.9 Illustration of the implantation of ZOH event-triggered and self-triggered control for WAPSs

The event-triggered or self-triggered centralized controller takes the wide-area measurements from PMUs, and then generates the corresponding control signals ΔE_{fi} and ΔP_{mi} aperiodicaly based on certain triggering conditions. It is known that these two control signals ΔE_{fi} and ΔP_{mi} (physical quantities) have to be realized by the physical components (exciters and turbines). Because the electrical controller (exciter) has a fast response speed and the inertial delay can be ignored, only a gain $1/K_{Ei}$ is added before the exciter. However, the inertial of mechanical controller (turbine) introduces significant delay to ΔP_{mi}. Thus, a simple lead compensator is used based on the turbine dynamics to counteract the delay. Because the generator internal states ($\Delta\delta$ and ΔE) are not directly measurable, the generator terminal bus measurements ($\Delta\theta$ and ΔV) are used to estimate the states. Since model inaccuracies and disturbances have been considered during controller design, the impact of using terminal voltage on control performance can be minimized.

For the simulation of the proposed event-triggered or self-triggered controller, other inter-area damping controllers (e.g. CPSSs) are not used, but the frequency controller (governor) and voltage controller (automatic voltage regulator - AVR) are still applied. To better evaluate the performance of the proposed control algorithms, the same power system model

and the same disturbances are simulated again under the control of CPSSs. During the simulation, four well-tuned CPSSs are deployed to four generators respectively.

In the simulation study, a series of operating condition changes are simulated. Initially, the simulation is running stable. At 3 second, a step load increase (from 967 MW to 1167 MW) at bus #10 is performed. At 5 second, the load at bus #10 is changed back to its original value (967 MW). At 10 second, a 3-phase short-circuit fault is simulated on the transmission line connecting buses #9 and #10. After 6-cycles, the fault is cleared by opening the two circuit breakers located at the ends of the transmission line, as shown in figure 2.3.

The simulation results of frequency responses (f) under aforementioned circumstances are shown in figure 2.10, among which figure 2.10(a) presents the control performance using the event-triggered controller, figure 2.10(b) is the damping result using self-triggered controller and figure 2.10(c) is the control performance under CPSSs, all in per units.

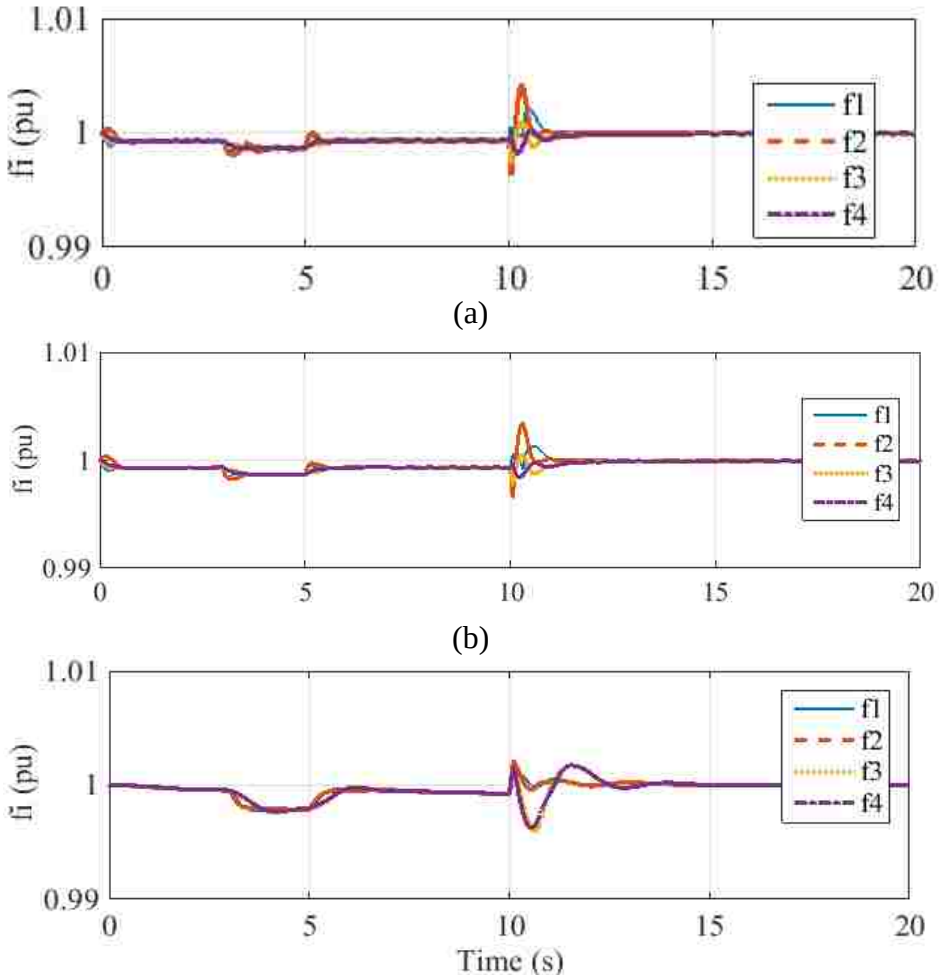

Figure 2.10 Frequency responses (f) under system disturbances, (a). The event-triggered controller; (b). The self-triggered controller; (c) CPSS.

Similarly, the terminal voltages responses (V) are shown in figure 2.11, among which figure 2.11(a) presents the control performance using the event-triggered controller, figure 2.11(b) is the damping result using self-triggered controller and figure 2.11(c) is the control performance under CPSSs, all in per units.

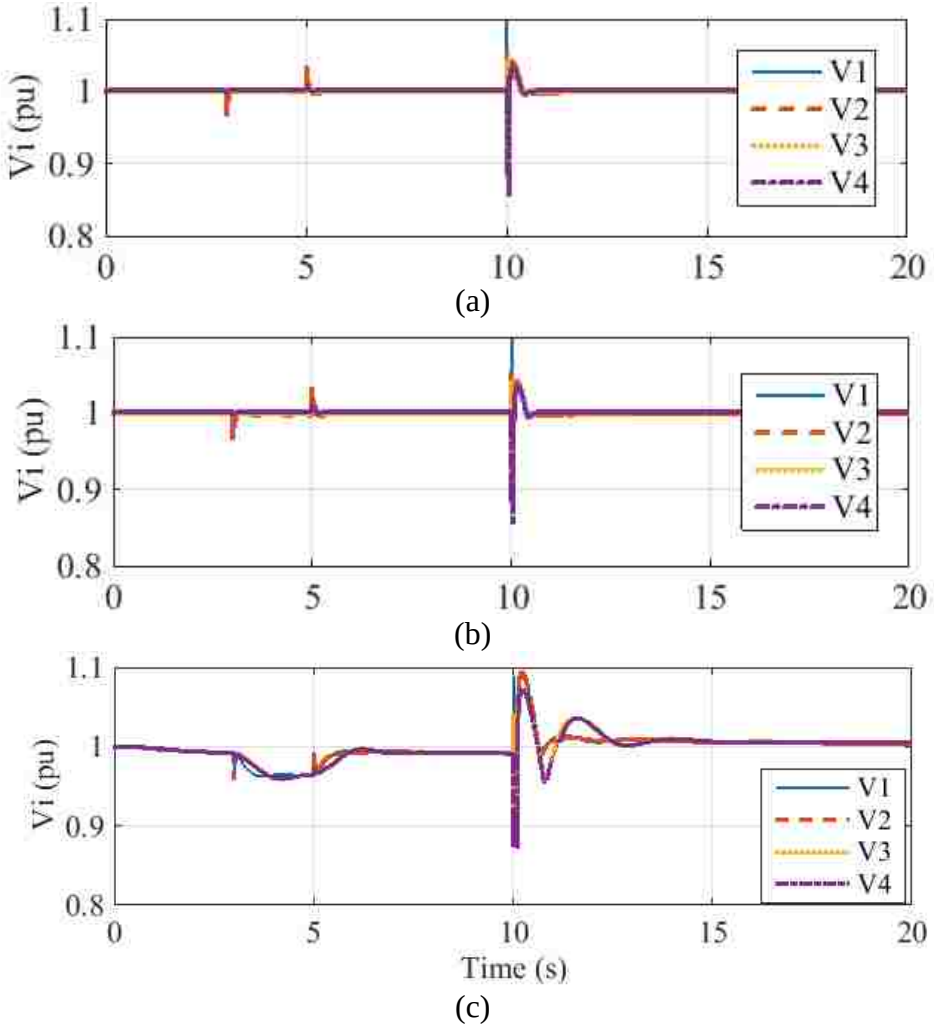

Figure 2.11 Terminal voltages responses (V) under system disturbances, (a). The event-triggered controller; (b). The self-triggered controller; (c) CPSS.

From figure 2.10 and figure 2.11, one can see that measurements from the detailed model do not have much impact on the performance of the designed control algorithm based on the linearized model. This is because the system parameter uncertainties and disturbances have been addressed during modeling.

Even if the CPSSs shown in figure 2.10(c) and figure 2.11(c) can also stabilize system under load change and fault situation, it takes 5 seconds to damp out oscillations caused by the line fault. While the proposed event-triggered or self-triggered controller only takes less than 3 seconds to realize the system stabilization. It is because that the proposed wide-area damping controller considers the overall system model and uses the synchronized wide-area data from PMUs [23-24].

The mechanical control outputs (ΔP_{m1}) of the event-triggered and self-triggered controller for generator #1 are shown in the figure 2.12. Among two plots, figure 2.12(a) shows the mechanical input power adjustments (ΔP_{m1}) using to event-triggered control while figure 2.12(b) is under self-triggered controller. From Figure11, one can see that the both controllers do not require continuous communications and control updates. In addition, the durations of control activation are decided by the severities of disturbances. The duration is smaller under smaller disturbances (load changes) and larger under larger disturbances (3-phase short-circuit fault). For protection purpose, ramp rates and bounds are applied to the overall control inputs. The control constraints actually introduce more system uncertainties. Obviously, the control constraints do not degrade control performance significantly.

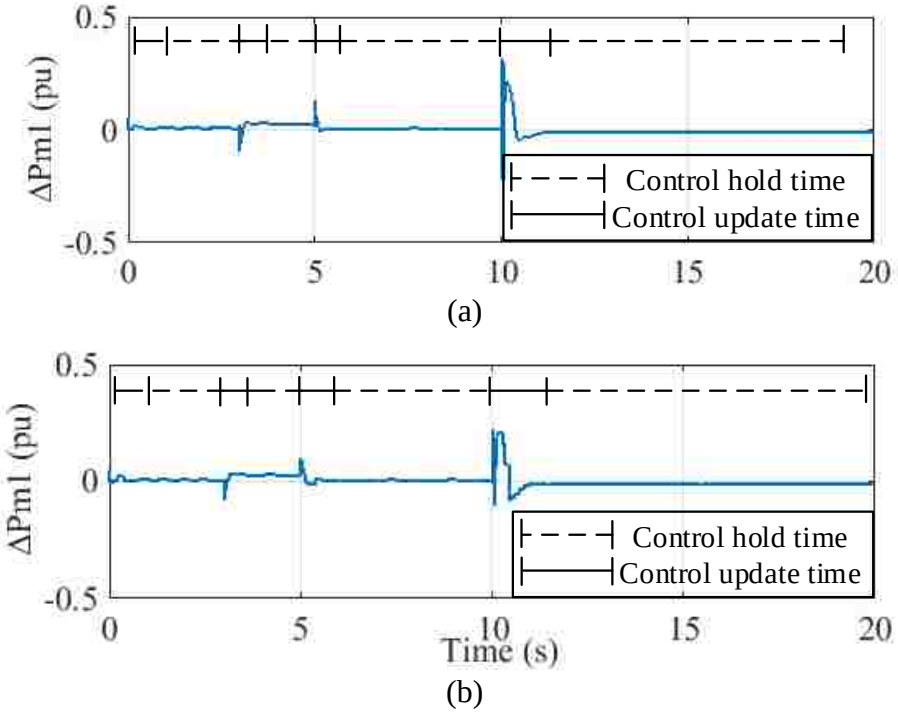

Figure 2.12 Mechanical Control output Adjustments ΔP_{m1} of generator #1, (a) Event-triggered control; (b). Self-triggered control

Above simulation results demonstrate the effectiveness of the proposed wide-area damping control algorithm. Even though the algorithm is designed based on the linearized model, the obtained performance is not compromised. Practical control applications prefer such simple yet effective algorithms.

2.7 Reinforcement Learning under Network Imperfections

Reinforcement learning (RL) includes a class of learning methods, which can approach optimal control iteratively through online learning without requiring system model. An actor involving in RL method usually interacts with system or environment and adjusts its behavior or policies to solve the optimization problems. A critic is responsible for executing the policy evaluation by assessing the results of applying current control signals into the system. Based on the assessment, the policy improvement is performed by the actor to yield an improved performance value compared to the previous one [20].

As one of the popular RL methods, Q-learning method is applied in this paper to solve the wide-area damping control problem of WAPSs. The optimal action-value function of the Q-learning method is defined in term of Bellman equation as [20],

$$Q_k^*(x,u) = E_\pi\{[r_k + \gamma V_{k+1}^*(x')]|x_k = x, u_k = u\} \tag{1.33}$$

where r_k is the stage cost, and $V_{k+1}^*(x') = \min_u Q_{k+1}^*(x',u')$ is the next-step value function. $0 \le \gamma \le 1$ is the discount rate and shows the importance of the future reward in the decision making process. The action-value function shows the expected return $E_\pi(\cdot)$ in state x and taking an action u under an arbitrary policy $\pi(x,u)$, and performing optimal policy $\pi^*(x,u)$ thereafter, until the optimal value of Q-function $Q_k^*(x,u)$ is reached [20]. In terms of the Q-function, the Bellman optimality equation has a simple form for a given state x, and selects the smallest value as

$$\begin{cases} V_k^*(x) = \min_u Q_k^*(x,u) \\ u_k^* = \arg\min_u Q_k^*(x,u) \end{cases} \tag{1.34}$$

The block diagram of WAPS under networked control in presence of network imperfections is illustrated in figure 2.13. Such a closed-loop system is referred to be a Networked Control System (NCS). In such NCS, network imperfections might occur when PMUs send the wide-area measurements to the control center, and when control center sends the control signals back to actuators for control implementation [25]. Without considering the network imperfections, the control system may not even maintain stability under severe situations [26].

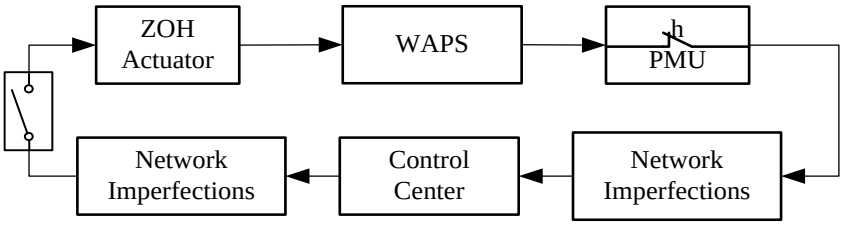

Figure 2.13 Block diagram of NCS under network imperfections

Due to the complexities of cyber uncertainties, it is impossible to consider all scenarios. This research considers two types of most common network imperfections, random communication delay and package dropout [26]. For a discrete-time WAPS with a sampling period of h, assuming that PMUs outputs y_k at time step k take a time of $\tau_{pc,k}$ to be transmitted to the central controller. In addition, it takes a time of $\tau_{ca,k}$ to be transmitted from the central controller to the actuators. Thus, the total communication delay during signal transmission is $\tau_k=\tau_{pc,k}+\tau_{ca,k}$. According to the concept of Zero-Order Hold (ZOH) controller, the system under control keeps using previous control signal until the new control signal is successfully delivered to actuators. If $\tau_k<h$, the delay is called short-term delay. Otherwise, the delay is called long-term delay [27]. Meanwhile, package dropout can be treated as an extreme scenario of communication delay. Two cases of delays can be classified as package dropouts. The first case is that the delay is larger than a certain threshold. The second case is that the newer control signal arrives before the older one. This paper only considers reasonable delays and package dropouts that can be effectively counteracted through control design. In another word, reasonable successful package delivery rate is required. Mathematically, the requirement can be described as, at least one among l consecutive packages is successfully delivered. It should be noted that short-term delays are normal and unavoidable, while long-term delays and package dropouts create major control difficulties.

The random communication delays and package dropouts in a discrete-time system are illustrated in figure 2.14, where the time for control calculation is neglected. In the figure, scenarios #1 and #4 are short-term delays, scenario #2 is a long-term delay, and scenarios #3 and #5 are package dropouts.

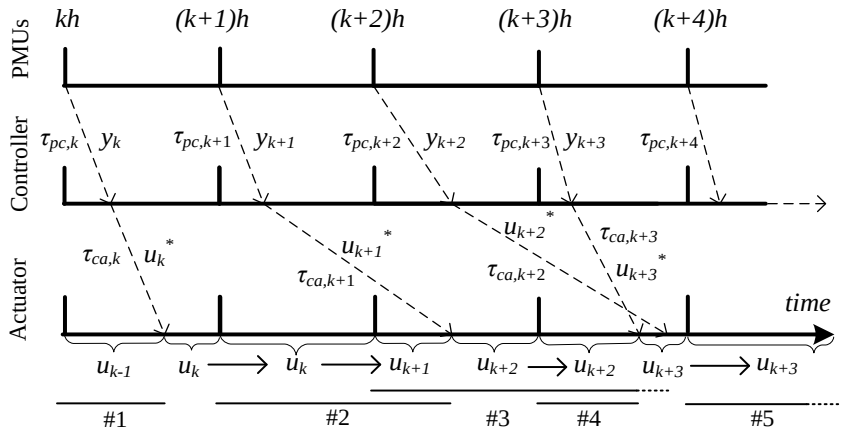

Figure 2.14 Illustration of various communication delays and package dropouts

In this research, the implementation of the proposed Q-learning method on wide-area damping control of WAPSs under network imperfections will be studied.

2.8 The Proposed RL Wide-Area Control Algorithm under Cyber and Physical Uncertainties

2.8.1 Modeling of WAPS under Network Imperfections

The linearized system dynamic considered for control design is given in eq. 1.14 where the system parameters A_y, B_y and D_y can be unknown. The system is continuous, but control inputs are updated in discrete-time. In order to analyze the WAPS with network imperfections, the system of (1.14) is sampled with a period of h. Without loss of generality, consider the k^{th} interval of [hk, $h(k+1)$]. Initially, the previously applied control signal u_{k-1} is carried over. u_{k-1} is kept being applied until the possible successful delivery of the updated control signal u_k, which may or may not happen. By defining the overall delay for control signal delivery as τ_k, there will be control update if $\tau_k<h$. For example, control signal is u_{k-1} during [hk, $hk+\tau_k$] and the control signal is updated to u_k during [$hk+\tau_k$, $h(k+1)$]. For long term delays or package dropouts ($\tau_k>h$), there will be no update on control signals during the k^{th} interval. Therefore, the discrete-time control model under network imperfections can be formulated as

$$\Delta y_{k+1} = \Psi \Delta y_k + \Gamma_{0,\tau k} \Delta u_k + \Gamma_{1,\tau k} \Delta u_{k-1} + D_k \tag{1.35}$$

where $\Psi = e^{A_y h} \subset \mathbb{R}^{n\times n}$, $\Gamma_{0,\tau_k} = \int_0^{h-\tau_k}(e^{A_y s}B_y)ds \subset \mathbb{R}^{n\times m}$, $\Gamma_{1,\tau_k} = \int_{h-\tau_k}^{h}(e^{A_y s}B_y)ds \subset \mathbb{R}^{n\times m}$, $D_k = \int_0^h \left[e^{A_y s}D_y(t)\right]ds \subset \mathbb{R}^{n\times 1}$, $\Delta u_k = [\Delta P_{m,k}^T\ \Delta E_{f,k}^T]^T$ is the control adjustment at step *k*, and Δu_{k-1} is the previous value of Δu_k.

Since random network imperfections are unavoidable, it is impossible to counteract their impacts perfectly [25]. Previous studies on NCS suggest that such random network imperfections can be effectively handled through statistical analysis [26]. Assuming that τ_k obeys the normal distribution at time step k^{th}, i.e. $\tau_k(\mathbb{E}_\tau, \sigma_\tau)$, in which $\mathbb{E}_\tau$ is the expectation and σ_τ is the standard deviation of τ_k. The random control model of (1.35) can be transformed into a deterministic control model with Γ_{0,τ_k} being replaced by $\Gamma_{0,\mathbb{E}_\tau} = \int_0^{h-\mathbb{E}_\tau}(e^{A_y s}B_y)ds$ and Γ_{1,τ_k} being replaced by $\Gamma_{1,\mathbb{E}_\tau} = \int_{h-\mathbb{E}_\tau}^{h}(e^{A_y s}B_y)ds$.

In order to simplify the following Q-learning based control design, the control model is transformed into an auxiliary augment form as shown in (1.36)

$$\Delta z_{k+1} = A_d \Delta z_k + B_d \Delta u_k \tag{1.36}$$

where $\Delta z_k = \begin{bmatrix} \Delta y_k \\ \Delta u_{k-1} \\ 1 \end{bmatrix}$, $A_d = \begin{bmatrix} \Psi^{n\times n} & \Gamma_{1,\mathbb{E}_\tau}^{n\times m} & D_M^{n\times 1} \\ \mathbf{0}^{m\times n} & \mathbf{0}^{m\times m} & \mathbf{0}^{m\times 1} \\ \mathbf{0}^{1\times n} & \mathbf{0}^{1\times m} & 1^{1\times 1} \end{bmatrix}$, $B_d = \begin{bmatrix} \Gamma_{0,\mathbb{E}_\tau}^{n\times m} \\ I^{m\times m} \\ \mathbf{0}^{1\times m} \end{bmatrix}$, $\mathbf{0}$ being a zero matrix, and *I* being an identity matrix.

According to the optimal control theory [20], the optimal control inputs for system (1.36) can be designed as

$$\Delta u_k^* = -(B_d^T P B_d + R)^{-1} B_d^T P A_d \Delta z_k \tag{1.37}$$

where $P \geq 0 \subset \mathbb{R}^{n\times n}$ is the Riccati equation solution [20] and $R \subset \mathbb{R}^{m\times m}$ is the positive-definite matrix.

Since the NCS suffers from network imperfections, the effective control signal (Δu_k) in (1.35) and (1.36) might be different from the current control signal calculated by the central controller (Δu_k^d). According to the assumption made in Subsection II-B, there is at least one successful control signal delivered in every *l* steps. The assumption can be formulated according to (1.38).

$$\begin{aligned} \Delta u_k &= p_k \Delta u_k^d + [(1-p_k)p_{k-1}]\Delta u_{k-1}^d + \cdots \\ &\quad + [(1-p_k)(1-p_{k-1})\cdots(1-p_{k-l+2})p_{k-l+1}]\Delta u_{k-l+1}^d \\ &= \sum_{i=1}^{l}\left[\prod_{j=1}^{i-1}(1-p_{k-j+1})\right] p_{k-i+1}\Delta u_{k-i+1}^d \end{aligned} \tag{1.38}$$

In (1.38), p_k is an indicator, where $p_k = 1$ stands for successful information delivery, and $p_k = 0$ stands for unsuccessful information delivery. Δu_k^d is the control signal calculated in control center at the k_{th} time step considering communication delay.

Similar to the above problem formulation, statistical analysis is introduced again in control design to counteract the effect of network imperfections. If the occurrence probability of on-time package delivery $P(p_k)|_{\mathbb{E}_p,\sigma_p}$ obeys the normal distribution in which $\mathbb{E}_p$ is the expectation of $P(p_k)$ and σ_p is the standard deviation, the designed control inputs u_k^d can be modified as [28]

$$\Delta u_k^d = \frac{1}{\mathbb{E}_p}\Delta u_k^* - \left[\left(1-\mathbb{E}_p\right)\mathbb{E}_p\right]\Delta u_{k-1}^* - \cdots - \left[\left(1-\mathbb{E}_p\right)^{l-1}\mathbb{E}_p\right]\Delta u_{k-l+1}^*$$
$$= \frac{1}{\mathbb{E}_p}\left[\Delta u_k^* - \sum_{i=2}^{l}\left(1-\mathbb{E}_p\right)^{i-1}\mathbb{E}_p\Delta u_{k-i+1}^*\right] \quad (1.39)$$

In (1.39), Δu_k^* and its previous values are calculated according to the Q-learning algorithm which is introduced in the next subsection. The model-free algorithm does not require physical system model, neither the statistical data on network imperfections. However, there is no guarantee that the calculated control signal Δu_k^* is effectively delivered. To further counteract the cyber uncertainties between the control center and the actuators, the instantaneous control signals Δu_k^*s calculated through Q-learning are weighted together in (1.39). The introduction of historic control signals can effectively counteract the previous impact of network imperfections on control signal delivery. In this way, the long term expectation on control performance can be expected to approach that under ideal conditions.

2.8.2 Q-Function Setup for Control Design

The control design in (1.37) requires known system dynamics to solve the Riccati equation as well as the optimal control inputs. To relax the requirements, Q-learning method is applied to solve the optimal control problem. An infinite-horizon value function [20] can be defined with Riccati equation solution P as quadratic in the state,

$$V_{k+1}^*(\Delta z_{k+1}) = \Delta z_{k+1}^T P \Delta z_{k+1} \quad (1.40)$$

The Bellman equation can be formulated accordingly as

$$Q^*(\Delta z_k, \Delta u_k^*) = \Delta z_k^T \Upsilon \Delta z_k + \Delta u_k^{*T} R \Delta u_k^* + V_{k+1}^*(\Delta z_{k+1}) \quad (1.41)$$

where $\Upsilon \subset \mathbb{R}^{n\times n}$ and $R \subset \mathbb{R}^{m\times m}$ are positive-definite cost matrixes.

By substituting (1.36) and (1.40) into the Bellman equation of (1.41), one can get

$$Q^*(\Delta z_k, \Delta u_k^*) = \Delta z_k^T \Upsilon \Delta z_k + \Delta u_k^{*T} R \Delta u_k^* + (A_d \Delta z_k + B_d \Delta u_k^*)^T P (A_d \Delta z_k + B_d \Delta u_k^*)$$

$$= \begin{bmatrix} \Delta z_k \\ \Delta u_k^* \end{bmatrix}^T \begin{bmatrix} A_d^T P A_d + \Upsilon & B_d^T P A_d \\ A_d^T P B_d & B_d^T P A_d + R \end{bmatrix} \begin{bmatrix} \Delta z_k \\ \Delta u_k^* \end{bmatrix} \tag{1.42}$$

Introduce a kernel matrix $H \in \mathbb{R}^{q \times q}$ as

$$H = \begin{bmatrix} A_d^T P A_d + \Upsilon & A_d^T P B_d \\ B_d^T P A_d & B_d^T P B_d + R \end{bmatrix} = \begin{bmatrix} H_{zz} & H_{zu} \\ H_{uz} & H_{uu} \end{bmatrix} \tag{1.43}$$

Then the Bellman equation of (1.42) can be rewritten as

$$Q^*(\Delta z_k, \Delta u_k^*) = \begin{bmatrix} \Delta z_k \\ \Delta u_k^* \end{bmatrix}^T H \begin{bmatrix} \Delta z_k \\ \Delta u_k^* \end{bmatrix} \tag{1.44}$$

Recall to (1.37), it yields the policy

$$\Delta u_k^* = -H_{uu}^{-1} H_{uz} \Delta z_k \tag{1.45}$$

Therefore, the optimal control gain can be obtained more conveniently by solving the kernel matrix H in (1.44) instead of using system dynamics A_d and B_d in (1.42). The brief derivation of numerical computing method to realize the online updating of H is given in the next subsection.

2.8.3 Model-Free Online Tuning of Control

To learn the kernel matrix H and approximate the optimal control signals, the Recursive Least Square (RLS) method is used in this paper [29]. First, one set of parametric structures $\hat{Q}(\bar{z}, h_i)$ and $\hat{u}_i(z)$ are selected to approximate the actual Q^* and u^* at the i^{th} iteration, respectively. It should be noted that i is the iteration step which is different from the time step k.

$$\hat{Q}_i(\Delta\bar{z}, h_i) = \Delta Z^T H_i \Delta Z = h_i^T \Delta\bar{z} \tag{1.46}$$

$$\Delta\hat{u}_i(\Delta z) = -H_{uu,i}^{-1} H_{uz,i} \Delta z \tag{1.47}$$

where $\Delta Z = [\Delta z^T \quad \Delta u^T]^T \in \mathbb{R}^q$, $\Delta\bar{z} = (\Delta Z_1^2, \dots, \Delta Z_1 \Delta Z_q, \Delta Z_2^2, \Delta Z_2 \Delta Z_3, \dots, Z_{q-1} Z_q, Z_q^2) \in \mathbb{R}^{q(q+1)/2}$ is the Kronecker product quadratic polynomial basis vector; $h = v(H)$ with $v(\cdot)$ being a vector function which is constructed by stacking the columns of the squared matrix into a one-column vector. Therefore, $v(\cdot)$ transforms a $q \times q$ matrix H into a $q(q+1)/2 \times 1$ vector h, and H can be solved as $H = v^{-1}(h)$ [23].

Then, to find h_{i+1}, the desired target function is written as

$$d(\bar{z}_k, h_i) = \Delta z_k^T \gamma \Delta z_k + \Delta \hat{u}_i^T(\Delta z_k) R \Delta \hat{u}_i(\Delta z_k) + Q_i\big(\Delta z_{k+1}, \Delta \hat{u}_{i+1}(\Delta z_{k+1})\big) \quad (1.48)$$

Due to the approximate error, the Bellman equation in (1.44) does not hold anymore. Then it can be defined as $h_{i+1}^T \Delta \bar{z}_k = d(\bar{z}_k, h_i) + e_k$, where e_k is the Bellman equation error. Therefore, h_{i+1} is found over a compact set Ω to minimize the Bellman equation error e_k in a least-square sense as

$$h_{i+1} = \arg\min_{h_{i+1}} \left\{ \int_\Omega \left| h_{i+1}^T \Delta \bar{z}_k - d(\bar{z}_k, h_i) \right|^2 d\Delta z_k \right\} \quad (1.49)$$

Then it can be solved as

$$h_{i+1} = \left(\int_\Omega \Delta \bar{z}_k \Delta \bar{z}_k^T d\Delta z_k \right)^{-1} \int_\Omega \Delta \bar{z}_k d(\bar{z}_k, h_i) d\Delta z_k \quad (1.50)$$

The kernel matrix H stops updating when Bellman equation error is less than certain small valve ε, e.g. $\|h_{i+1} - h_i\| < \varepsilon$. [29-30]. If the Bellman equation error e_k becomes zero, the system optimality is achieved. It should be mentioned that the quantity of the historic information (i.e. compact set Ω) required to solve (1.50) is dependent on the system dimension, i.e. the number of PMUs used in the NCS. The overall procedure of the proposed Q-learning based algorithm for wide-area control is summarized in table 2.1. One advantage of the algorithm is that it makes incremental improvements and the convergence of learning can be theoretically proved based on the mild assumptions as introduced in the paper. This means that it can avoid the abrupt/risky control adjustments while performance improvement can be guaranteed even before the optimal solution is found

Table 2.1: IMPLEMENTATION OF THE Q-LEARNING BASED CONTROL ALGORITHM

1) Initialize the system state set Δz, control action Δu, value function $Q(\Delta z, \Delta u)$, and kernel matrix H
2) **for** $i = 0$ to a given number iterations,
   if $\|h_{i+1} - h_i\| > \varepsilon$, **do**
   2.1) Observe the state Δz of the WAPS
   2.2) Calculate the least squares to solve the kernel matrix H_{i+1} (1.50)
   2.3) Perform policy update to approximate the optimal control signal $\Delta\hat{u}_i(\Delta z)$ (1.47)
   2.4) Implement the control signal and observe the state $\Delta z'$ (1.36)
   2.5) Update the Q-function (1.46)
3) **end**

2.9 Simulation Results of the Q-Learning Based Wide-Area Control Algorithm

It is a common sense that the practical WAPS model is complicated and highly nonlinear. Due to the complexity of the physical system and cyber uncertainties, it is impossible to model such a large system precisely. To solve the wide-area damping control problem effectively, a model-free control algorithm is proposed based on the Q-learning technique. In order to evaluate its real-world performance, the linear model-based control algorithm is tested with variable types of simplified linearized and detailed nonlinear WAPS models, i.e. IEEE 11-bus and 30-bus models [11].

To select the next control signal Δu_k replacing the currently effective control signal Δu_{k-1}, each of the most recent l successive control signals (Δu_k^d, Δu_{k-1}^d, ……, Δu_{k-l+1}^d) is assigned with a random probability $P|_{(\mathbb{E}_p,\sigma_p)} \subset [0,1]$ with expectation being $\mathbb{E}_p$ and deviation being σ_p. If the random probability P is larger than $\mathbb{E}_p$, the corresponding control signal will be successfully delivered (p=1), otherwise, the control signal will not be delivered in time due to network imperfections (p=0). The search of Δu_k starts from Δu_k^d to Δu_{k-l+1}^d. During the searching process, the first control signal with nonzero p will be selected as Δu_k. If none of the l control signals is delivered and the situation has already happened for l-1 times, one of the l signals will be randomly selected. This is because of the assumption that there is at least one successful control signal delivery in every l steps. To decide the instant of time when the new control signal Δu_kwill be deployed, similar statistical analysis is employed. A random number within the range of [0, h] is generated

to decide τ_k. The random number has an expectation of $\mathbb{E}_\tau$ and deviation of σ_τ. Once the τ_k is determined, the Δu_k will be deployed at the instant of $hk+\tau_k$ at the k^{th} step.

During simulation, h is set to 0.1s, l is set to 3, $\mathbb{E}_p$ is set to 0.9, σ_p is set to 0.05, $\mathbb{E}_\tau$ is set to $0.75h$, and σ_τ is set to $0.2h$. It should be noted that $\mathbb{E}_p$ is intentionally set to a small value (frequent network imperfection) to challenge the proposed control algorithm.

2.9.1 Simulation with Linearized 11-Bus Model

The initial large deviations are set up to 15% of the equilibrium operating points. In addition, up to 5% disturbances (D_k) are simulated to investigate the effectiveness of the designed algorithm under small and continuous system disturbances. The damping performance of the proposed algorithm under aforementioned conditions are shown in figure 2.15. Among the three plots, figure 2.15(a) shows the responses of bus voltage phase angle deviation ($\Delta\theta$), figure 2.15(b) shows the responses of frequency deviation (Δf), and figure 2.15(c) shows the responses of terminal bus voltage deviation (ΔV), all in per-unit values. The distribution of communication delay and package dropout during the simulation is shown in the figure 2.16. It can be seen that the wide-area oscillations get damped effectively by the proposed control algorithm under both cyber and physical uncertainties. Besides, the robustness of the proposed algorithm against the network imperfections is also demonstrated.

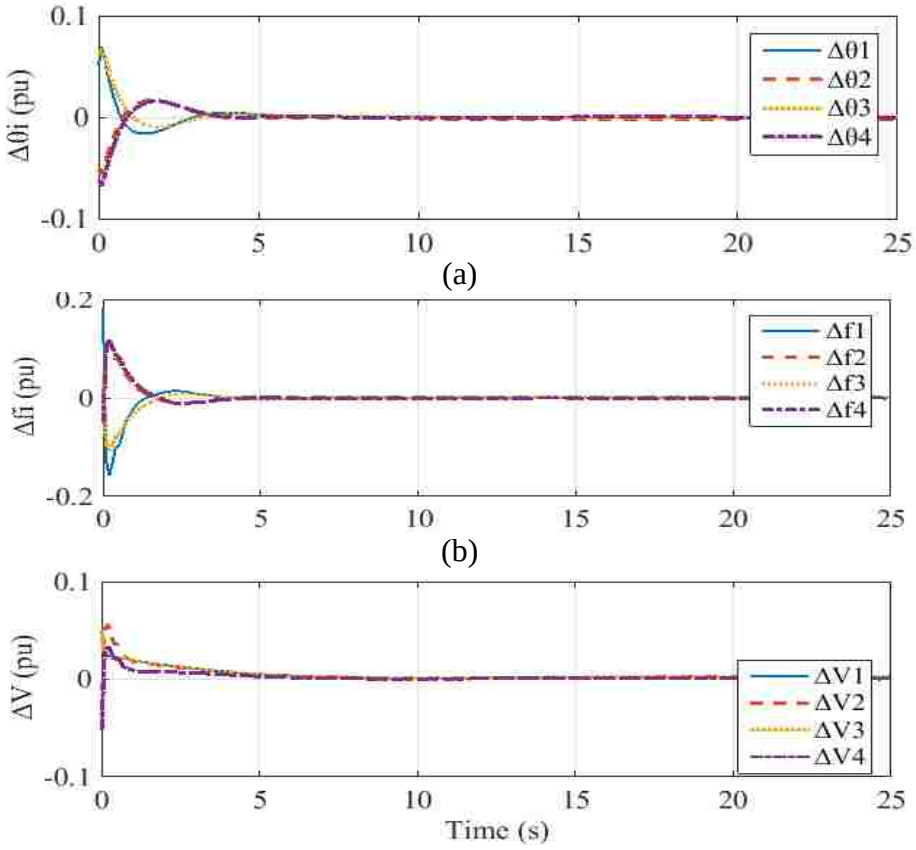

Figure 2.15 Simulation results of the proposed Q-learning controller with linearized 11-bus model: (a). Phase angle deviation ($\Delta\theta$); (b). Frequency deviations (Δf); (c). Terminal bus voltage deviations (ΔV).

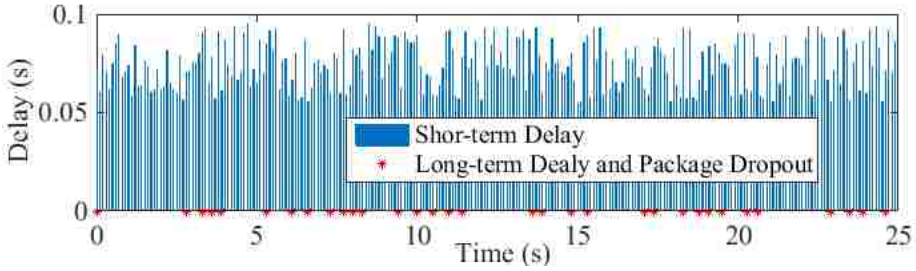

Figure 2.16 Distribution of communication delay and package dropout

The control signal responses are presented in figure 2.17. Because the control signals of the four subsystems are quite similar for small signal disturbance, only control inputs (ΔE_{f1} and ΔP_{m1}) of subsystem #1 are presented. Due to the continuous system disturbances, it can be seen that the control adjustments oscillate around zero. As illustrated in the figure 2.18, the Bellman equation error e_k converges to a small neighborhood of zero, which demonstrates achievement of the system optimality.

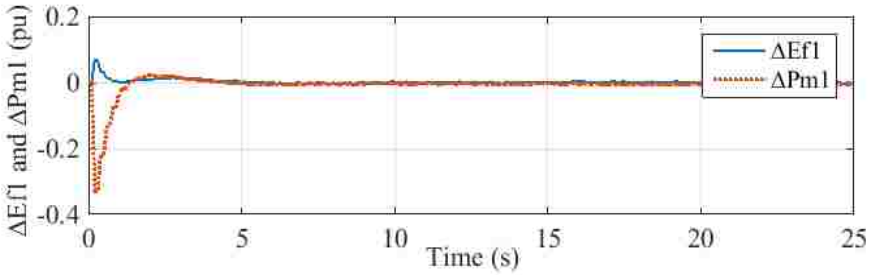

Figure 2.17 Wide-area damping control signals for generator #1 (adjustments of field voltage ΔE_{f1} and mechanical power input ΔP_{m1})

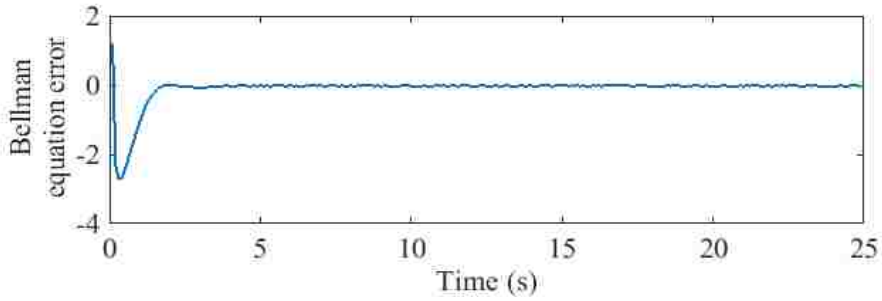

Figure 2.18 Bellman equation error e_k.

2.9.2 Simulation with Linearized 30-Bus Model

In order to further test evaluate the effectiveness of the proposed control algorithm on variable types of WAPS, a similar simulation is conducted on a linearized IEEE 30-bus system as shown in figure 2.19 [31]. The parameters of an IEEE 30-bus system can be found online at [31].

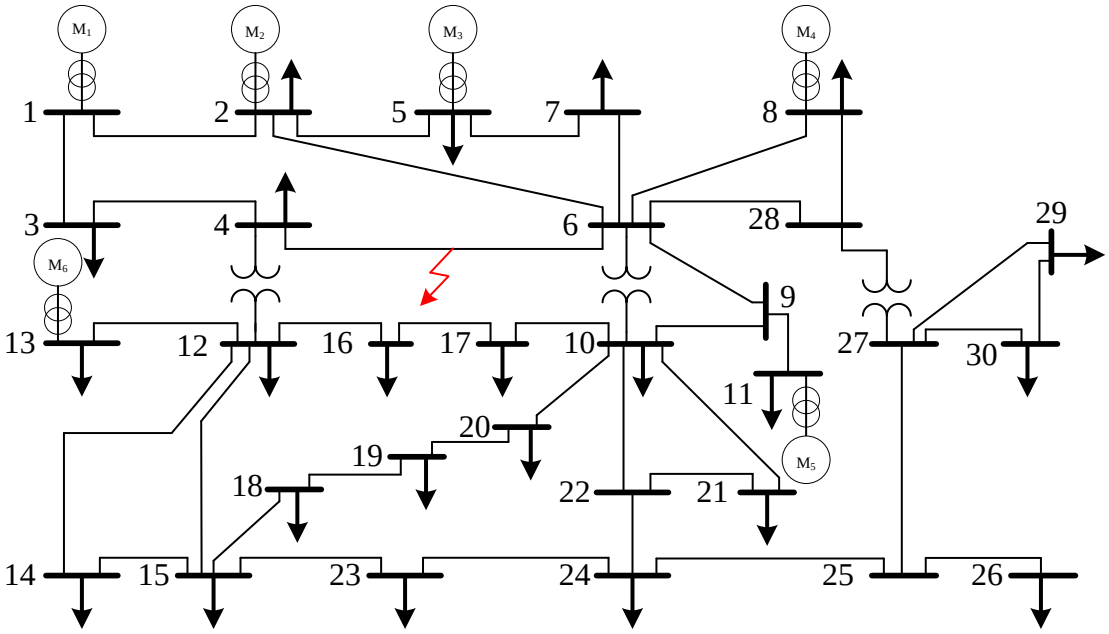

Figure 2.19 IEEE 30-bus WAPS

The damping performance of the proposed algorithm under aforementioned conditions are shown in figure 2.20. Among the three plots, figure 2.20(a) shows the response of bus voltage phase angle deviation ($\Delta\theta$), figure 2.20(b) shows the response of frequency deviation (Δf), and figure 2.20(c) shows the response of terminal bus voltage deviation (ΔV), all in per-unit values. The Bellman equation error e_k is shown in the figure 2.21. As can be observed, the proposed control algorithm can effectively damp the oscillation for a more complicated WAPS under network imperfections. Moreover, the proposed Q-learning is a novel online time-based learning technique. Compared with conventional offline policy or value iteration schemes, the time-based learning techniques are updating along with time online instead of iteration offline, which have been demonstrated as an effective method to overcome the issue from high computational complexity [32].

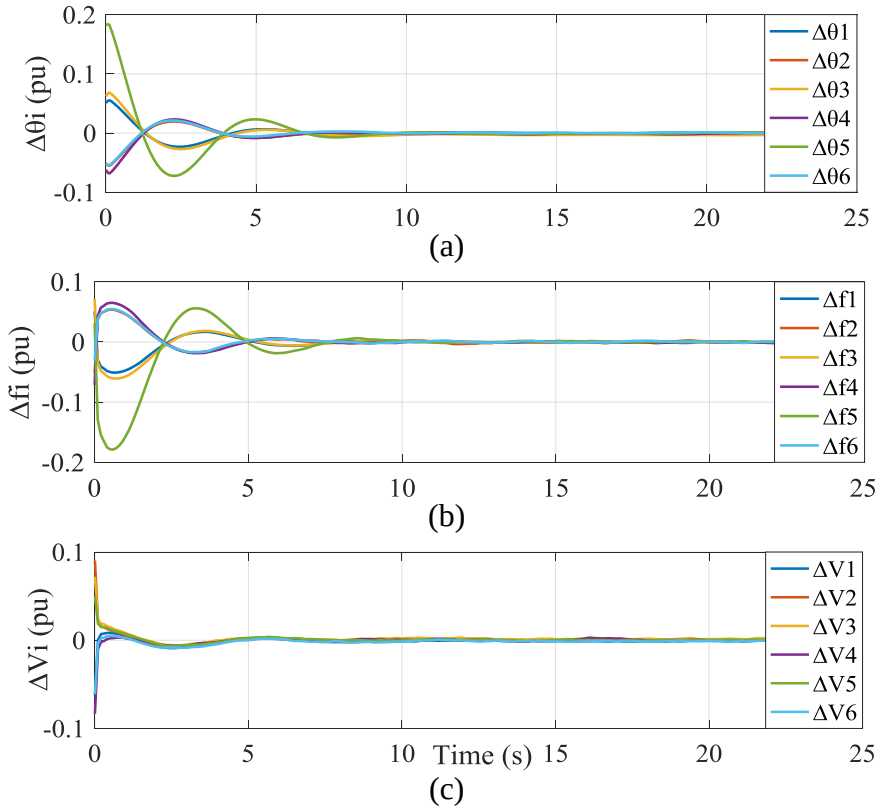

Figure 2.20 Simulation results of the proposed Q-learning controller with linearized 30-bus model: (a). Phase angle deviation ($\Delta\theta$); (b). Frequency deviations (Δf); (c). Terminal bus voltage deviations (ΔV).

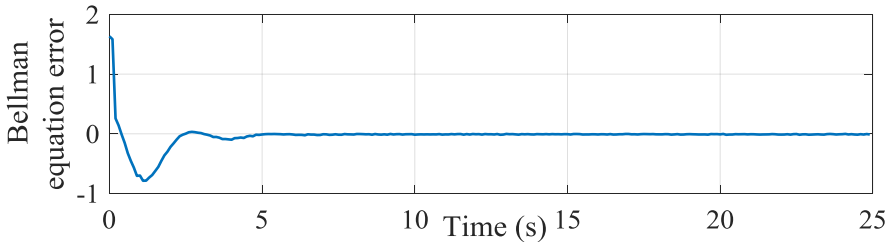

Figure 2.21 Bellman equation error e_k.

In addition, to better illustrate the influence of the network imperfections and to demonstrate the effectiveness of the proposed controller against this problem, the comparison results of frequency responses are shown in figure 2.22. The simulation is conducted on an IEEE 30-bus system with package dropout ($\mathbb{E}_p = 0.9$) and without package dropout ($\mathbb{E}_p = 1$) under the same communication delay ($\mathbb{E}_\tau = 0.75h$). It can be observed that the network imperfections have a tiny influence on damping performance of the proposed controller. However, the communication network quality, i.e. package

dropout and communication delay, if not properly considered, can result low frequency oscillations in WAPS.

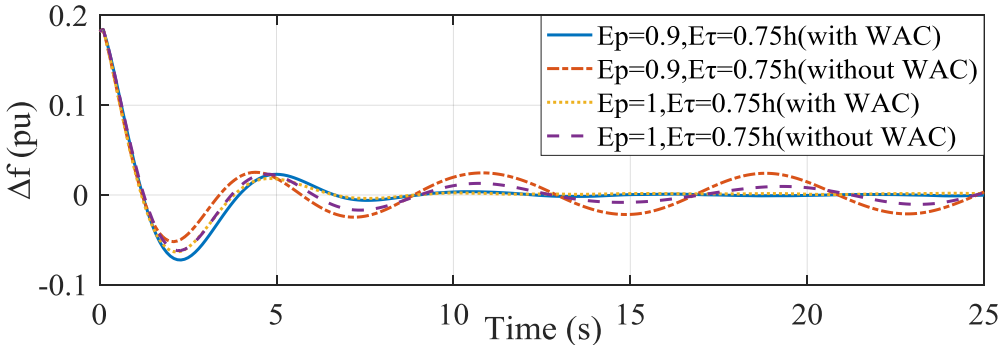

Figure 2.22 Frequency responses under different network imperfections with and without design considerations.

2.9.3 Simulation with Nonlinear Detailed 11-Bus Model

In this section, the detailed nonlinear WAPS model is used to evaluate the performance of the proposed control algorithm under the practical application. The simulation studies are conducted on the Simulink module that comes with the SimPowerSystem™ toolbox for inter-area oscillations [33]. The specific targets are focused on testing the algorithm performance under large system disturbances and network imperfections. In addition, the control performance is also compared against well-tuned CPSSs. The simulation settings of network imperfections are same as that in linear-model-based simulations in Subsection V-A. The implementation of the proposed control algorithm with the detailed WAPSs model is illustrated in fig 2.23.

It is known that two control signals ΔE_{fi} and ΔP_{mi} (physical quantities) have to be realized by the physical components (exciters and turbines). Because the electrical controller (exciter) has a fast response speed and the inertial delay can be ignored, only a gain $1/K_{Ei}$ is added after the filed voltage adjustment (ΔE_{fi}) [11]. However, the inertial of mechanical controller (turbine) introduces significant delay to ΔP_{mi}. Thus, a simple lead compensator as shown in figure 2.1 is designed based on the turbine dynamics to counteract the delay.

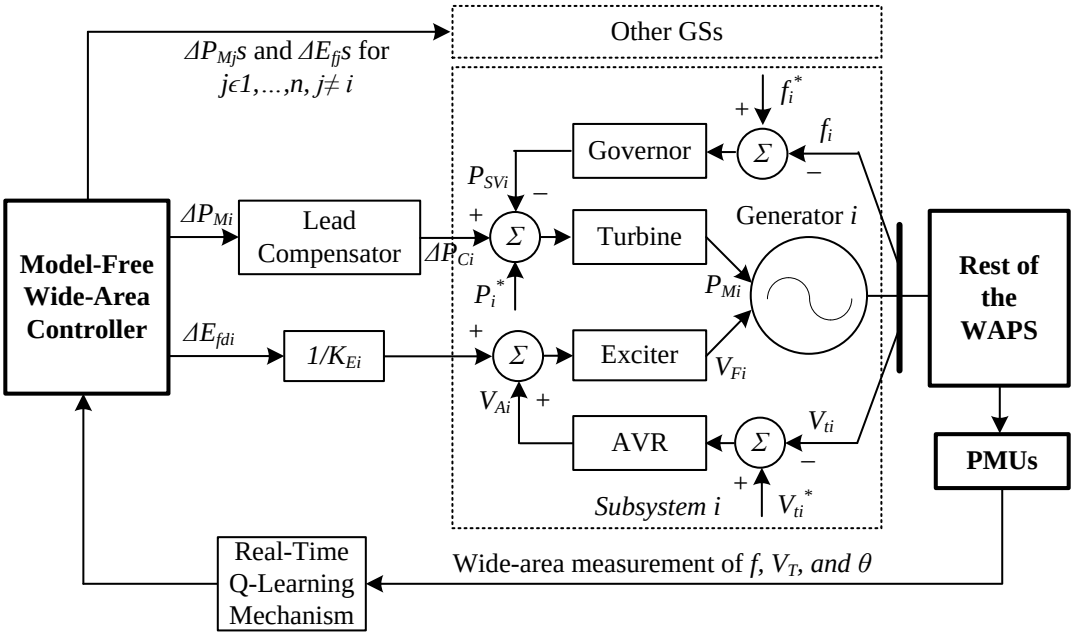

Figure 2.23 Implementation of the proposed control algorithm for WAPSs.

Because the generator internal voltages cannot be easily acquired, the generator terminal voltage measurements are used instead as an input to the wide-area controller. A series of different operating conditions are simulated in the study. Initially, the system is running stable. At time 3 second, a 200 MW step load increasing is performed at bus # 10 (from 967 MW to 1167 MW). At time 5 second, the load at bus #10 returns back to its original value (967 MW). At time 10 second, a three-phase short circuit is performed at the transmission line disconnecting bus #9 and bus #10. After 6 cycles, the fault is removed by opening the two circuit breakers located at both ends of the transmission line, as presented in figure 2.3. The total simulation time is set to 20 seconds.

In order to fully understand the performance of the proposed model-free control algorithm, it is compared with CPSSs which are simulated under the same power system scenarios. In the simulation, four well-tuned CPSSs from [11] are deployed at four generators respectively. It should be noted that the problem of network imperfections is not considered in CPSSs since they are local controllers.

The simulation results of frequency responses (f) under aforementioned circumstances are shown in figure 2.24, among which figure 2.24(a) presents the control performance using the proposed Q-learning networked controller and figure 2.24(b) is the damping result under CPSSs (without using the proposed controller), all in per units. Similarly, the

terminal voltages responses (V) are shown in figure 2.25, among which figure 2.25(a) presents the control performance using the proposed model-free networked controller and figure 2.25(b) is the damping result under CPSSs (without using the proposed controller), all in per units.

As introduced before, the proposed Q-learning method uses a linear WAPS model to approximate the optimal control of a nonlinear system. However, it can be observed from the figure 2.24(a) and figure 2.25(a) that the possible measurement deviations from a nonlinear model do not degrade the performance of the linear-based control design. It is because that the system dynamics with disturbances are able to be learned and updated online. Even if the CPSSs shown in figure 2.24 and figure 2.25 can also stabilize system under load change and fault situation, it takes 5 seconds to damp out oscillations caused by the line fault. While the proposed controller only takes less than 3 seconds to realize the system stabilization. It should be noted that the voltage drop in figure 2.25, is not a steady state error. It is because CPSSs cannot recover the low order frequency oscillations in a timely manner. If given sufficient time, the deviation under CPSSs will disappear. Because frequency f and voltage V of the designed control method are adjusted at the same time through coordination, the transient performance is much better than that under conventional controllers.

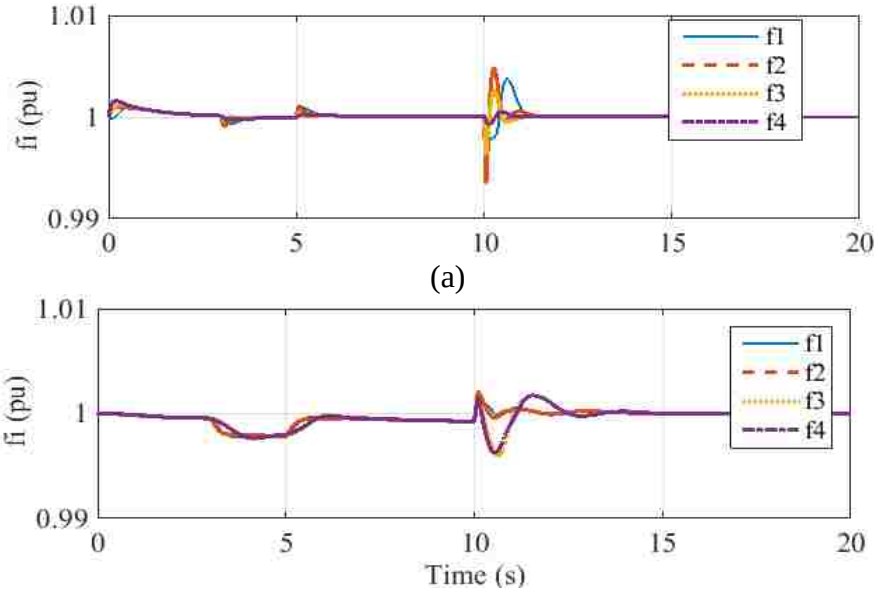

Figure 2.24 Frequency responses (f) under system disturbances, (a). The proposed Q-learning networked controller; (b). CPSS.

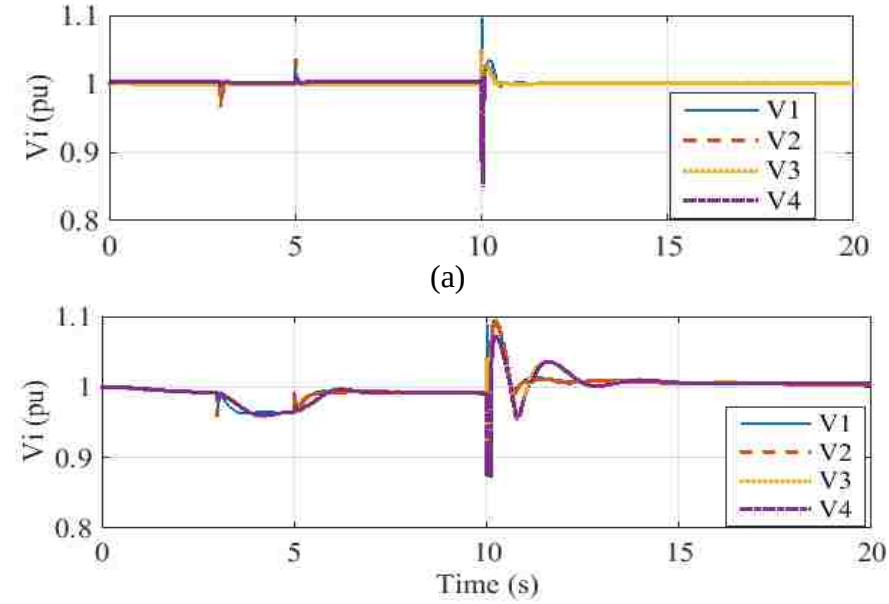

Figure 2.25 Terminal voltages responses (V) under system disturbances, (a). The proposed Q-learning networked controller; (b). CPSS.

The overall control inputs (P_{m1} and E_{f1}) to generator #1 are shown in figure 2.26. For protection purpose, ramp rates and bounds are applied to the overall control inputs. Although the practical control constraints further increases system uncertainties, control performance is not degraded.

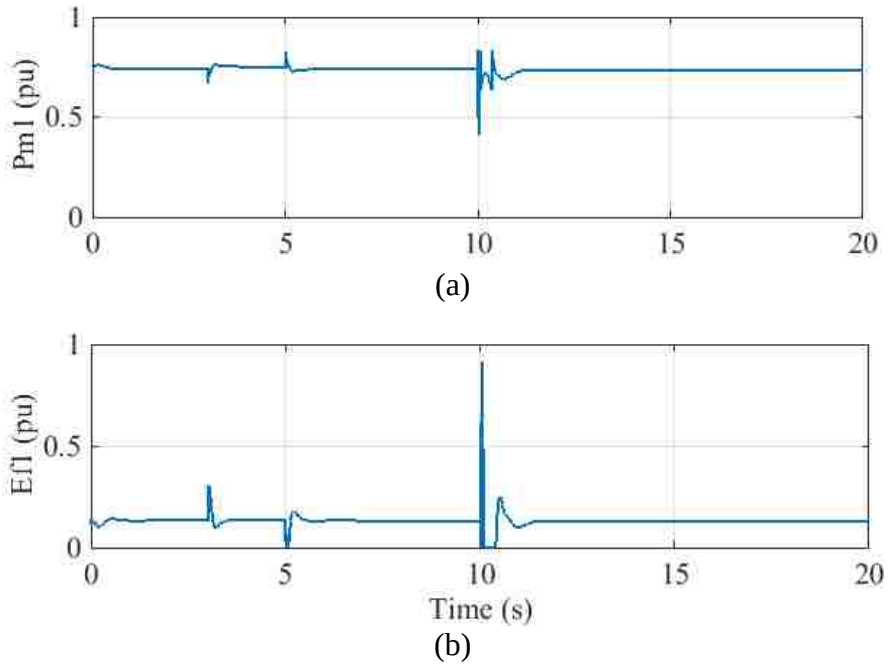

Figure 2.26 Overall control inputs to generator #1, (a). Mechanical input power P_{m1}; (b). Field voltage E_{f1}.

2.9.4 Simulation with Nonlinear Detailed 30-Bus Model

In this subsection, similar simulations are performed on a detailed IEEE 30-bus model as presented in figure 2.19. The performance of the proposed wide-area controller is compared with the behavior of CPSSs (without using the proposed controller). In order to make the paper condensed, only a three-phase self-clean fault is conducted between bus #4 and bus #6. The total simulation time is 15s and the fault happens at the 2s during the steady state. After 3 cycles, the fault is removed by opening the two circuit breakers located at both ends of the transmission line. The frequency responses of using the proposed wide-area controller and the CPSSs are shown in the figure 2.17(a) and figure 2.17(b), respectively. As can be observed, the proposed Q-learning controller can achieve the wide-area oscillation damping within 4s, while CPSSs have to take more than 8s to damp out the oscillations. Actually, the tuning process of CPSSs is full of difficulties, and the low-frequency oscillation is a common phenomenon when system operating condition changes. One major reason is that the CPSSs only use the local measurements. Therefore, WAMS has created a great opportunity to better manage WAPSs.

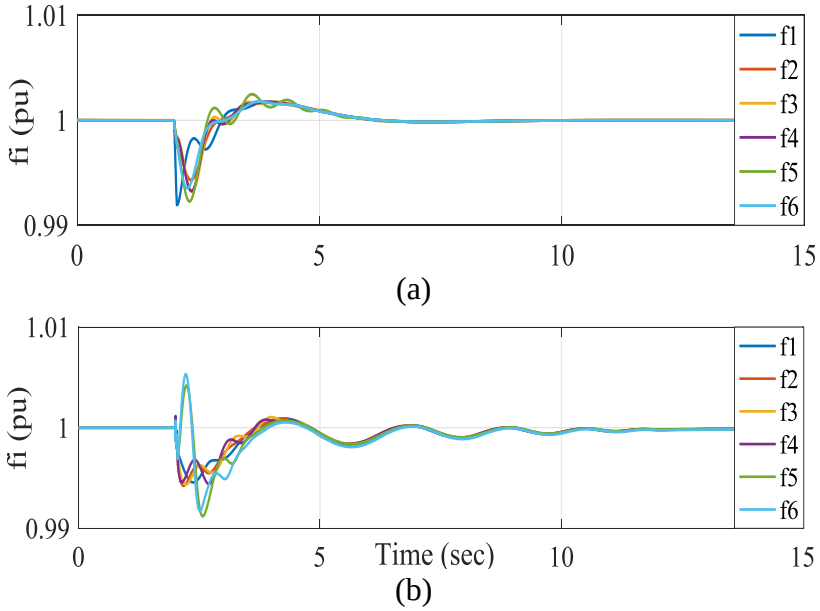

Figure 2.27 Frequency responses (f) under system disturbances, (a). The proposed Q-learning networked controller; (b). CPSS.

Above simulation results demonstrate the effectiveness of the proposed wide-area damping control algorithm. Usually, RL method requires significant time to obtain the desired knowledge, and the learning from scratch is difficult as shown in our previous paper [34]. In this work, once the initial knowledge is obtained, the incremental online learning afterward will be converged much faster. So the learning speed is not a problem since the utility can afford the cost of capable infrastructure. Besides, even though the design is linear-based, the obtained performance is not compromised. Practical control applications prefer such simple yet effective algorithms.

SHIPBOARD POWER SYSTEM CONTROL

3.1 Problem Description

A shipboard power system (SPS) consists of various loads for propulsion, service, warfighting and so on. Loads, such as electromagnetic guns, electromagnetic launch systems, and electron lasers, consume a large amount of power within a short period of time are called pulsed power loads (PPLs) [35]. Due to economic considerations, the capacity of an SPS is usually decided to mainly satisfy the needs of non-PPLs that are online most of the time, instead of meeting the possible peak demand of all loads [36]. Besides capacity limit, it is almost impossible to increase the generation of conventional synchronous generators (SGs) instantaneously during the deployment of PPLs. Large voltage sag in medium voltage DC (MVDC) SPS and large frequency droop in medium voltage AC (MVAC) SPS will occur when a large PPL is directly connected to an SPS. Consequently, not only sensitive loads might be tripped offline, but also the system-wide instability of SPS might occur [37].

In order to accommodate the high transient energy demand of PPLs, energy storage system (ESS) such as supercapacitor or flywheel is usually installed [38]. Once fully charged, ESS is disconnected from the SPS to supply PPLs alone so that the negative strikes during PPLs deployment are isolated. Thus, the problem of PPLs accommodation can be converted to charging control of ESS. Many issues such as large voltage and frequency disturbances, and even system instability possibly result from the improperly designed charging controller of ESS [39]. In this paper, the supercapacitor-type of ESS is adopted due to its advantages such as simple maintenance, high reliability, and high power density [40]. The concept can be extended to other types of ESS, but the controller might need to be redesigned if its properties are significantly different.

So far, there are not many solutions for PPL accommodation. In [41] and [42], authors present a limit-based control and a profile-based control algorithm, respectively. Both algorithms have been tested through hardware experiments with an MVDC testbed. These two algorithms generate charging current references based on the offline analysis. Since interactions between generations and charging controls as well as possible changes to

operating conditions are not considered, there is still room for performance improvement. To realize fast and smooth charging, it is desirable to design closed-loop control algorithms to better coordinate the generation and charging controls under dynamic operating conditions.

In [50], a proportional integral (PI) based algorithm and a feedback linearization (FL) based algorithm are presented. These algorithms are easy to implement and their effectiveness is demonstrated through both software simulations and power hardware-in-the-loop (PHIL) simulations with detailed SPS model. However, the performance of PI control is limited, whereas the FL is sensitive to parameter accuracy. To further improve the system performance, an adaptive critic design (ACD) based control algorithm is developed in [51]. Through interactive learnings of two neural networks (NNs) for cost-to-go function and optimal control, respectively, the near-optimal control can be realized. However, the ACD based algorithm requires a separately determined control references and the known system dynamics. Moreover, an initial admissible control policy is needed to maintain the system stability during NN learning. Finally, the system disturbance is simply considered as being bounded and the optimality of control is not rigorously proved.

To overcome the problems with existing solutions, both problem formulation and control design should be improved. The accurate model of SPS is very complicated, and the outermost control designs do not need to use very accurate model if the inner control loop is reasonably fast and accurate. But the balance between effectiveness and simplicity of SPS model has to be sufficiently considered, and the effectiveness of simplified model must be well tested. In addition, there are not many solutions to handle the disturbance in the existing control designs [50-51]. In general, using a static bound in control model to counteract the impact of disturbance results in a large ultimate bound [51]. Meanwhile, it is also very difficult to dynamically approximate the disturbance especially when system models are partially unknown. In this paper, the frequency dynamic is augmented with a damping term to better approximate the real-world conditions. The damping coefficient is treated as a disturbance that fluctuates throughout time. Such formulation can not only significantly improve the validness of the model, but can also maintain system simplicity.

A zero-sum game (ZSG) online-learning optimal NN control design is presented in this paper for the uncertain nonlinear system under disturbances. Two players of the game are

controller and disturbance, respectively. The controller aims at approximating the bound of disturbance based on system output, and then learning the optimal control under the disturbance through reinforcement learning. Due to its universal approximation capability [18], NNs are used to estimate the unknown system dynamics, approximate the solution of Hamilton-Jacobi-Isaac (HJI) equation (i.e. the optimal cost function for two-player ZSG), and learn the optimal control. Since the control objective is to optimize a predefined performance index, there is no need to separately provide the control references. Because ZSG is utilized to dynamically approximate the upper bound of disturbances, the impact of disturbances can be well addressed. The optimality of an MVAC SPS is guaranteed by using a time-based neuro dynamic programming (NDP) scheme. The usage of NN identifier avoids the requirement for knowledge of system model. Lastly, the controller does not require initial control being admissible and can be introduced at any initial state.

3.2 Modelling of SPS

The simplified SPS model for PPL accommodation consists of two subsystems that stand for the dynamics of the aggregated synchronous generator (SG) and the supercapacitor, respectively. Details of the model are introduced as follows.

To model the SG [12], the relationship between system frequency change and supply-demand mismatch can be formulated as

$$\dot{f} = k_1(P_M - P_E) + P_D = k_1(P_M - P_L - I_C V_C) + D_f(f_{ref} - f) \tag{3.1}$$

In (3.1), f is the system frequency and f_{ref} is the reference of f. k_1 is the constant decided by parameters of the generator. P_M is the mechanical power input to the SG, and $P_E = P_C+P_D+P_L$ is the electrical power output with P_C being the charging power of supercapacitor, P_D being the damping power, and P_L being all other loads and losses. Meanwhile, P_C is represented as $P_C = V_C I_C$ with V_C and I_C being the voltage and the charging current of a supercapacitor, respectively. $P_D = D_f(f_{ref} - f)$ represents the damping effect of the SPS where D_f is the damping factor.

Since only one equation (3.1) is used to represent the frequency dynamics of an SPS, the system modeling inaccuracy is unavoidable. The impact from unmodeled dynamics can be alleviated by assuming a time-varying damping factor D_f. In other words, the damping

factor D_f is introduced to improve the validness of the simplified model. Due to the complexity of the SPS and its wide-range of operating conditions, D_f keeps changing randomly within a certain range. During the control design, it is preferable to treat D_f in (2.1) as a bounded disturbance. To model the dynamics of a supercapacitor, the *i-v* characteristic of supercapacitor shown in (3.2) is used.

$$\dot{V}_C = k_2 I_C \tag{3.2}$$

where k_2 is the reciprocal capacitance of the supercapacitor. The objective of charging control is to charge a specific amount of energy to the supercapacitor as fast as possible. Since capacitor voltage V_C is an indicator of the stored energy, the control objective can be realized by generating charging current I_C based on the difference between the current V_C and its desired value V_{regf}. During the charging process, another control input P_M of SG is adjusted cooperatively to maintain the system stability and the desired dynamic performance. The objective of fast and smooth charging can be realized through optimal control.

Defining the system state vector as $x(t)=[x_1, x_2]^T=[f(t), V_C(t)]^T \subset \mathfrak{R}^{n\times 1}$ and control inputs vector as $u(t)=[u_1, u_2]^T=[P_M(t)-P_L(t), I_C(t)]^T \subset \mathfrak{R}^{m\times 1}$, the mechanical power control input can be calculated as $P_M=u_1+P_L$. In this paper, the load P_L is assumed to be measureable or can be indirectly calculated. The severe change or inaccuracy of P_L can be considered together with other uncertainties as disturbance D_f. The control reference vector $x_{ref} = [f_{ref}, V_{ref}]^T \subset \mathfrak{R}^{n\times 1}$ is constant, and $e(t) = [e_1\ e_2]^T = x(t)-x_{ref} \subset \mathfrak{R}^{n\times 1}$ is defined as the tracking error of states. Then, the tracking error dynamic of the simplified SPS model defined in (3.1) and (3.2) can be generalized as

$$\begin{cases} \dot{x}_1(t) = \dot{e}_1(t) = k_1 u_1(t) - k_1\left(e_2(t) + V_{ref}\right)u_2(t) - D_f(t)e_1(t) \\ \dot{x}_2(t) = \dot{e}_2(t) = k_2 u_2(t) \end{cases} \tag{3.3}$$

It is important to note that the system of (3.3) can be considered as a nonlinear continuous-time affine system. The tracking error dynamic of (3.3) can be further represented as

$$\dot{e}(t) = G\big(e(t)\big)u(t) + D\big(e(t)\big) \tag{3.4}$$

where $D(e(t)) = K(e(t))D_f(t)$ with $K(e(t)) = \begin{bmatrix} -e_1(t) \\ 0 \end{bmatrix} \subset \mathfrak{R}^{n\times 1}$, and $G(e(t)) = \begin{bmatrix} k_1 & -k_1\left(e_2(t)+V_{ref}\right) \\ 0 & k_2 \end{bmatrix} \subset \mathfrak{R}^{n\times m}$ is the control coefficient matrix.

The model of (3.4) has serval interesting properties from control perspectives such as nonlinearity, strong couplings of subsystems, and multiple-inputs-multiple-outputs formulation. It is true that accurate MVAC SPS model is usually difficult to acquire due to its physical complexity. Even if $D(e(t))$ can improve the performance, the SPS model is still inaccurate and unknown. Therefore, the artificial neural network (NN) [43] and ZSG techniques are adopted in this research.

3.3 Formulation of Two-Player Zero-Sum Game

Since the system optimality is preferable than stabilizing design, the optimal control design is exploited. In (3.4), the control input $u(t)$ and disturbance $D(e(t))$ in MVAC SPS can be considered as two players. Then, the existing ZSG theory [44-45] can be utilized to attain the optimal control input $u^*(t)$ under the worst disturbance $D^*(e(t))$ of the system [20], [46]. According to [44], [45] and [20], the optimal cost function $J^*(e, u, d)$ can be defined as

$$J^*\left[e(t),u(t),D\left(e(t)\right)\right]=\min_u\max_d\int_t^\infty r\left[e(t),u(t),D\left(e(t)\right)\right]dt \tag{3.5}$$

where the cost-to-go function $r(\cdot)$ is defined as

$$r\left[e(t),u(t),D\left(e(t)\right)\right]=e^T(t)Qe(t)+u^T(t)Ru(t)-\gamma^2D^T\left(e(t)\right)D\left(e(t)\right) \tag{3.6}$$

where R and Q are all positive definite weighting matrixes for the performance index, and $\gamma\geq\gamma^*>0$ with γ^* being the smallest γ when the system is stabilized [47]. In this differential game, $u(t)$ is the minimizing player and $D(e(t))$ is the maximizing player. According to game theory [44-45], this two-player optimal control problem has a unique solution if the Nash condition holds as $\min_u\max_d J(e(0),u,D)=\max_d\min_u J(e(0),u,D)$.

Similar to [44] and [20], the cost function is assumed to be continuously differentiable. Using Bellman's principle of optimality, one can have

$$\begin{aligned}&H\left[e(t),u(t),D\left(e(t)\right)\right]=0\\&=\min_u\max_d\left\{\frac{\partial J^{*T}\left(e(t)\right)}{\partial e(t)}\left[G\left(e(t)\right)u(t)+D\left(e(t)\right)\right]+r\left[e(t),u(t),D\left(e(t)\right)\right]\right\}\end{aligned} \tag{3.7}$$

which is a nonlinear partial-deferential-equation, and is also called as HJI equation. With the cost-to-go function $r(\cdot)$ in (3.6), a closed-loop expression of the optimal controller can be determined as

$$u^*(t) = -\frac{1}{2} R^{-1} G^T\left(e(t)\right)\left[\partial J^*\left(e(t)\right)/\partial e(t)\right] \tag{3.8}$$

$$D_f^*(t) = \frac{1}{2\gamma^2} K^T\left(e(t)\right)\left[\partial J^*\left(e(t)\right)/\partial e(t)\right] \tag{3.9}$$

Several important problems should be clarified to better understand the concept of the ZSG based control algorithm. During control process, the controller is trying to manipulate disturbance D_f. If D_f is adjustable, it should not be treated as a disturbance, but a control signal instead. Based on system responses, the controller is trying to estimate D_f^*, which is the time-varying upper bound of D_f. Since D_f^* is being continuously estimated, the impact of the time-varying disturbance can be effectively counteracted. Based on D_f^*, optimal control u^* in term of the predefined cost function of (3.5) can be approximated. It is important to note that the approximated D_f^* in (3.9) is not specifically used during the calculation and implementation of u^*. Actually, the term $\partial J^*\left(e(t)\right)/\partial e(t)$ used in u^* calculation of (8) can be explained as a function of the D_f^*. The optimality of control can be found in [47], [48] and in the original work on ZSG [45-46].

In order to obtain the optimal strategies in (3.8) and (3.9), system dynamics $G(e(t))$ and the solution of HJI equation (i.e. the optimal cost function J^*) in (3.7) are required. Obviously, the HJI equation is extremely difficult and even impossible to solve due to the nonlinearity. Therefore, an approximate solution is necessary to obtain the benefit from optimality. The NN has been demonstrated as a desirable technique to approximate the optimal solutions. Two NNs are designed during control development in the next section. One is used for system dynamics $G(e(t))$ identification, the other one is for HJI equation solution approximation. Using the novel NN design, the unknown parameters and unmolded system dynamics are identified together effectively.

3.4 Simulation Results of Zero-Sum Game based Control Design for PPL

In order to evaluate the performance of NDP based control algorithm, the multi-converter based PHIL simulation and the real-time simulations with simplified and detailed MVAC SPS models are carried out using Opal-RT. The detailed models are more complicated than the model in (3.4), which are suitable for testing the proposed solution with unknown model dynamics.

3.4.1 Real-Time Simulation with Simplified SPS Model

In this simulation, the proposed control algorithm is tested on a unified 94 MW-4 kV MVAC SPS model developed by ESRDC [49]. A fifth-order SG model has been used in the simulation [12]. The control objective is to charge an ESS with 0.12 per unit (pu) energy (53.156 MJ), which means that the voltage of an 18.75 F UC will be charged from 0.6 pu to 0.85 pu. At the same time, the frequency has to be maintained at 1 pu constantly. The weighting matrixes R and Q for the performance index are selected to be identity matrixes. For NNs setup, the inputs to the identifier NN are $x(t)$ with initial condition $x(0)=[1, 0.5]^T$ and $u(t)$ with $u(0)=[0, 0]^T$. The control parameters are selected to be $\alpha_I=0.6$, $\alpha_J=0.8$, $\alpha_s=0.5$ and $\gamma=100$, while identification and value function NN weights are both initialized between (0, 1). In order to better evaluate the control performance of the system under disturbances, a load change is also simulated. The total simulation time is 70 s with a sampling frequency of 200 Hz. The UC starts to be charged at 2 s and a load increasing occurs at 22 s. Considering the practical requirements of the SPS, the parameters of the charging circuit including the maximum charging current (maximum charging power) and the ramp rate of mechanical power are given in table 3.1.

Table 3.1: CONTROL CONSTRAINTS

Generator	P_M	UC	I_C
Ramp-up rate	0.02 pu/s	Upper bound	0.04 pu
Ramp-down rate	-0.02 pu/s	Lower bound	-0.04 pu

The responses of charging current (I_C) and voltage (V_C) of the UC-type of ESS are shown in figure 3.1 and figure 3.2, respectively. The charging process initiates at 2s and lasts about 20s. The system frequency responses (f) is shown in figure 3.3, which indicates that the system states (V_C and f) can well track their corresponding references. As can be seen, the sudden increasing of load (0.1 pu) at 20 s causes some disturbances on the frequency, but it has no impact on the charging circuit. Then, the mechanical power input (P_M) and the electrical output power (P_C+P_L) are shown in figure 3.4. It can be noticed that the mechanical power adjustments have no severe changes, which is able to provide a smooth charging process for the UC and decrease the frequency oscillation of the system. As the input mechanical power and the consumed electrical power become balanced, the system is

stabilized. Finally, the HJI equation error is shown in figure 3.5. As the HJI equation error converges to zero, it demonstrates the fact that the proposed control design indeed achieves optimality.

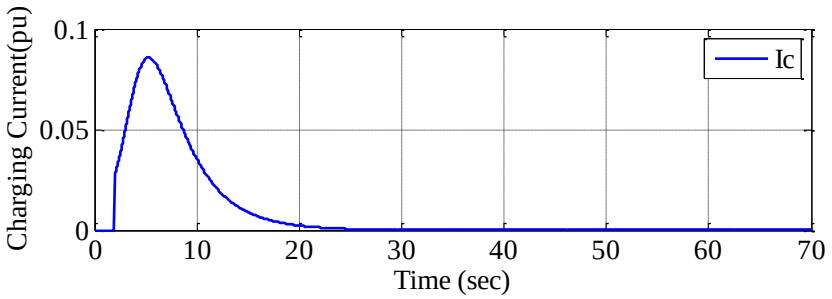

Figure 3.1 Charging current I_C

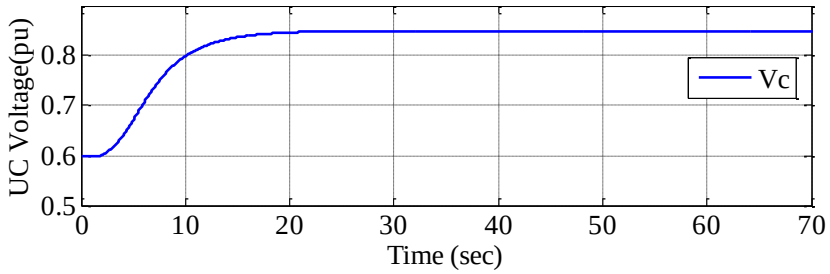

Figure 3.2 UC ESS voltage response V_C

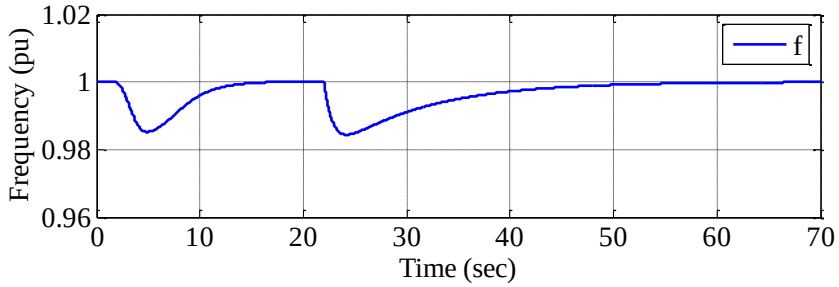

Figure 3.3 System frequency response f

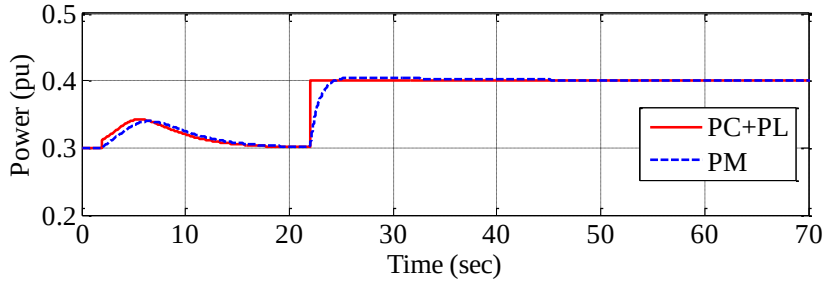

Figure 3.4 The mechanical power input and the electrical power output

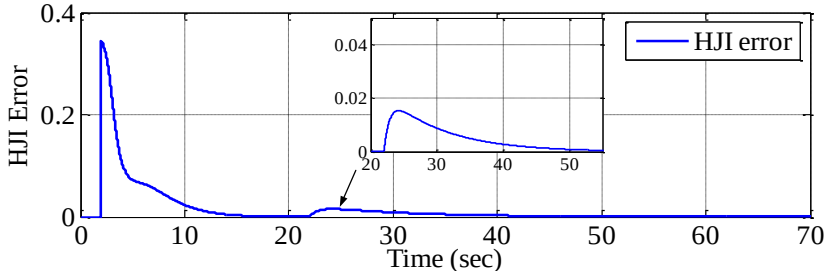

Figure 3.5 HJI equation error

3.4.2 Real-Time Simulation with the Detailed SPS Model

In order to better evaluate the effectiveness of the proposed controller, more simulations have been carried out on a detailed SPS model as shown in figure 3.6. Besides, the control performance has been compared with the conventional PI controller as introduced in [50]. All of the modules in the simulation are taken from the Simpowersystem toolbox in Matlab/Simulink, which can closely emulate the dynamic responses of a real SPS. In this system, one part of the electrical power output (P_E) is transmitted to the load center for normal load consumption (P_L) through the transmission line, while the other part (P_C) is used to charge the UC through an AC/DC inventor and a DC/DC converter. To better emulate the self-discharging problem of the UC, a two-branch model is used in the simulation [52]. During the simulation, the normal load is set to be 0.5 pu and a similar sudden load increase (0.1 pu) is tested at time 22 s to better evaluate the control performance under disturbances. The major parameter settings of the system are given in table 3.2.

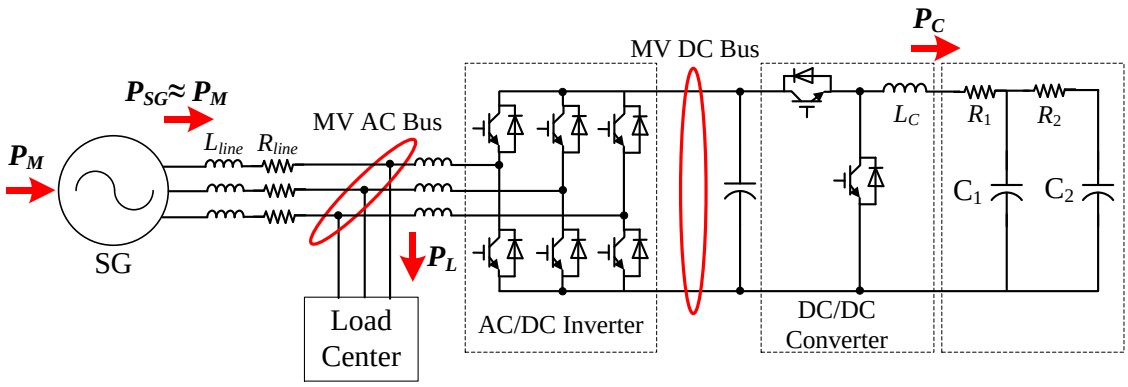

Figure 3.6 The schematic diagram of the detailed simulation model

Table 3.2: PARAMETERS FOR CHARGING CIRCUIT

Parameter	Value	Description
R_{line}	0.15 Ω	Line resistance
L_{line}	0.45 mH	Line inductance
L_C	4.7 mF	Converter inductance
C_1, C_2	18 F, 0.75F	UC
R_1, R_2	0.1 mΩ, 0.3 Ω	Self-discharging resistance
H	6.02 sec	Inertia coefficient of SG

The responses of the charging current (I_C) and the voltage (V_C) on the UC are shown in figure 3.7 and figure 3.8, respectively. The charging process initiates at 2 s and lasts about

25 s. The entire charging curve matches the results of the simplified simulation, but the charging time is increased due to the implementation of the mechanical devices and the power converters. The system frequency response is presented in figure 3.9. Similar to the previous case, both voltage (V_C) and frequency (f) can track well to their corresponding references even under system disturbances. Furthermore, it can be observed that the entire charging process of the proposed ZSM controller is much smoother than the conventional PI controller. Similarly, the HJI equation error is shown in figure 3.10. The mechanical power input (P_M) and the electrical power output (P_C+P_L) are shown in figure 3.11. As the HJI error converged to zero, the system optimality is achieved under the proposed control. In addition, to better illustrate the control performance of the proposed controller on a three-phase machine, the terminal voltage (V_m) and the output currents (in dq- coordinate system) of the SG are shown in figure 3.12, figure 3.13 and figure 3.14, respectively.

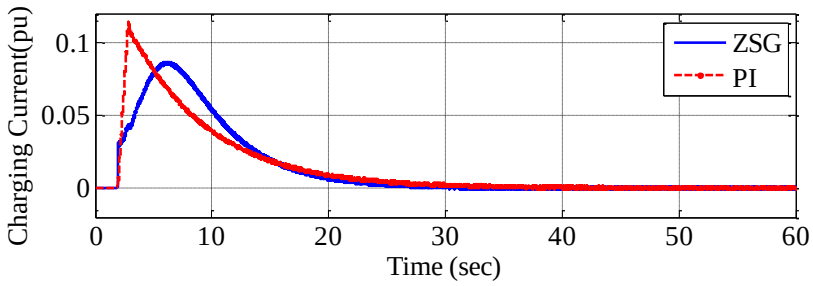

Figure 3.7 Charging current I_C

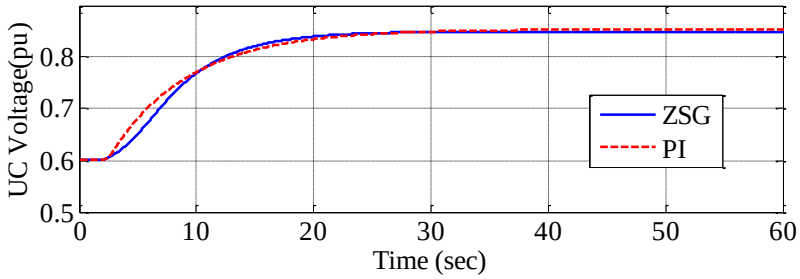

Figure 3.8 UC ESS voltage response V_C

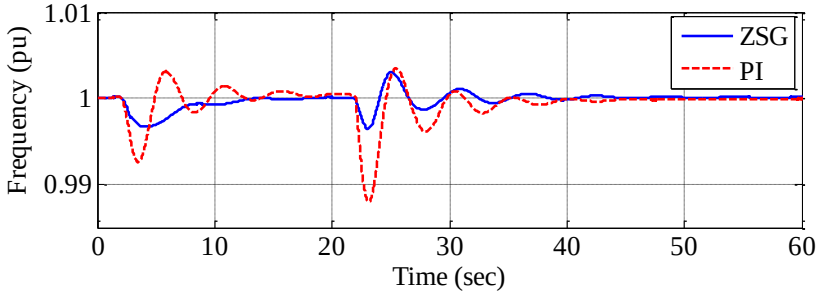

Figure 3.9 System frequency response f

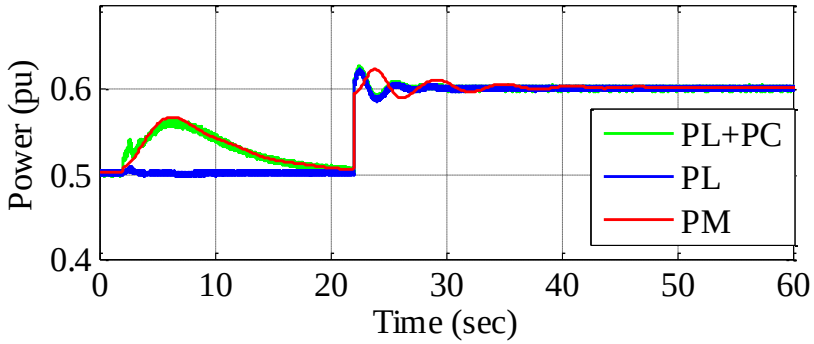

Figure 3.10 The mechanical power input and the electrical power output

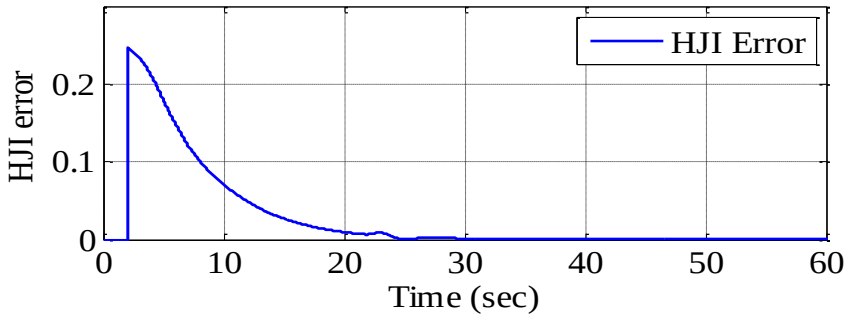

Figure 3.11 HJI equation error

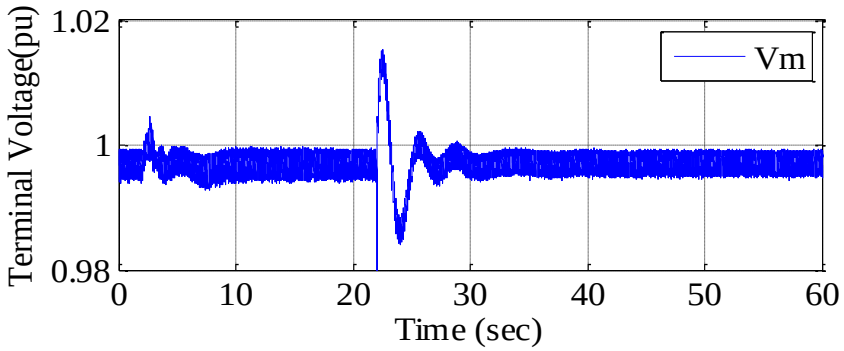

Figure 3.12 The terminal voltage of the SG

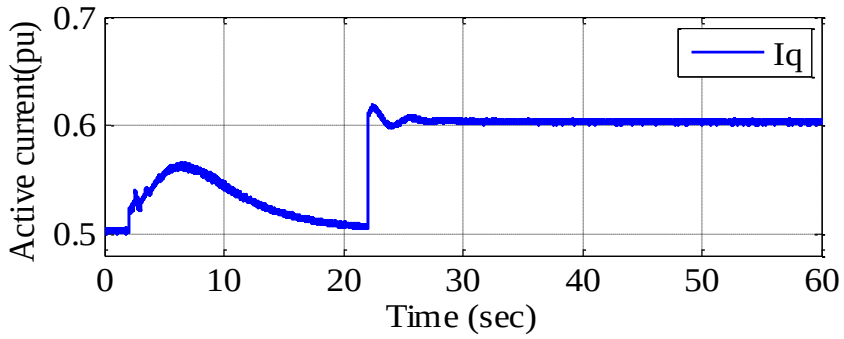

Figure 3.13 The output current I_q of the SG on q-axis

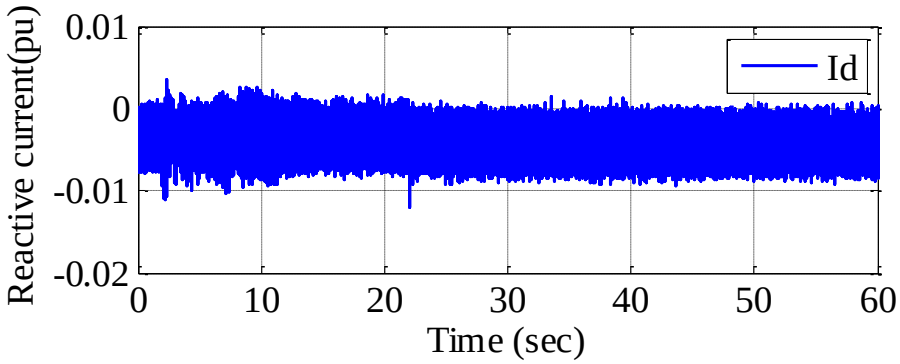

Figure 3.14 The output current I_d of the SG on *d*-axis

3.4.3 PHIL Simulation on a Power Electronics Emulated SPS

The configuration of the emulated SPS is shown in figure 3.15. First, a fifth order VSG is emulated using a three-phase inverter together with a programmable DC power supply [12]. Then, a buck converter is utilized to charge the UC. A pulse width modulation (PWM) rectifier is used as an interface between the VSG and the UC charging system. To limit initial charging current [53], the UC is pre-charged to certain voltage (24 V). During pre-charging, the input side of buck converter is switched to another DC power supply. By setting the duty ratio of the buck converter to a fixed value (i.e. 0.5) and slowly increasing the input voltage (&< 5 V/s), the voltage of the UC can be increased smoothly. As can see from figure 3.15, an AC load bank is connected to the AC bus to emulate PL and a DC load bank is used to discharge the UC during repeated experimentation.

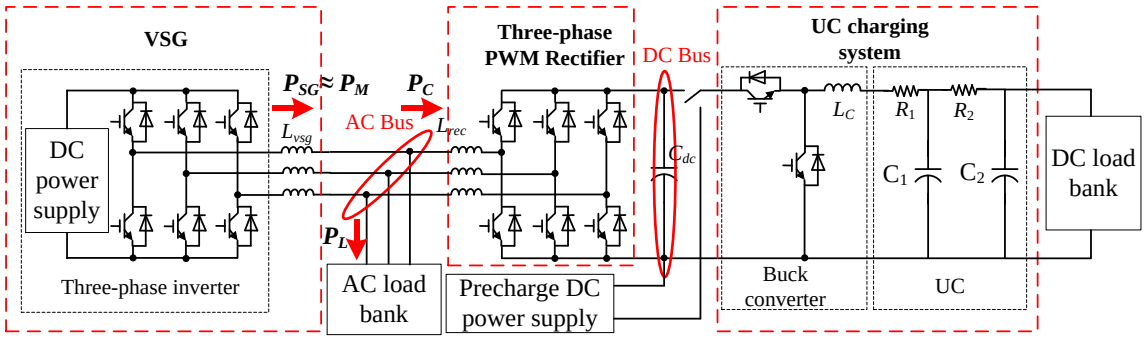

Figure 3.15 The configuration of the power electronics emulated SPS system

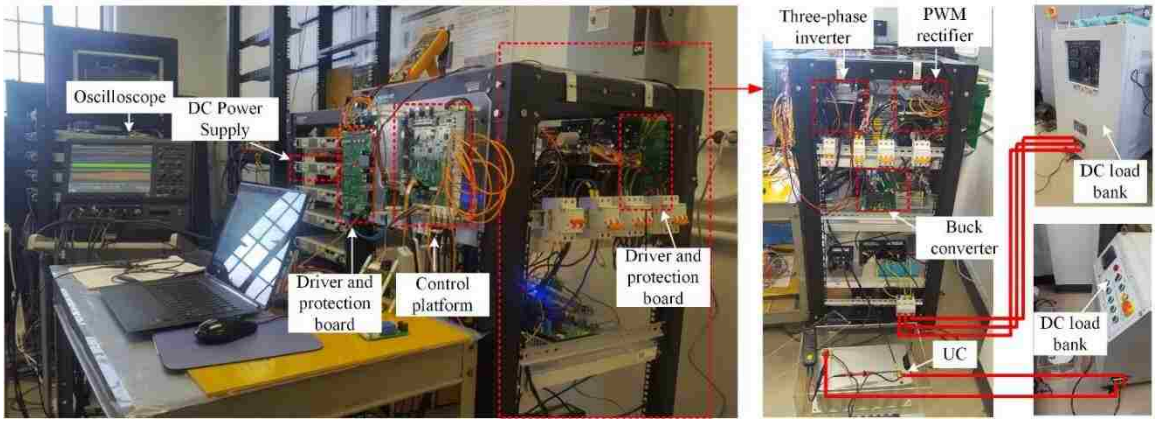

Figure 3.16 Testbed for PHIL simulation

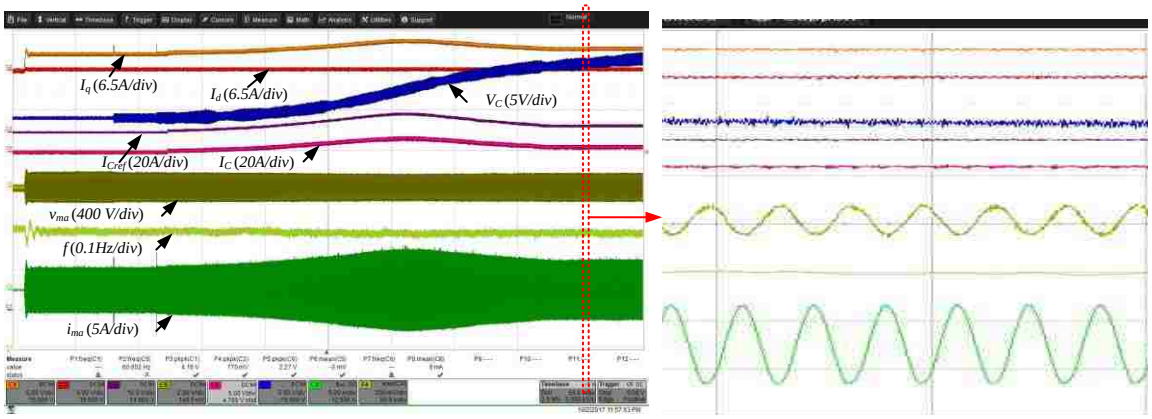

Figure 3.17 Simulation results

Figure 3.16 shows the corresponding experiment prototype of which the power circuit parameters are listed in table 3.3. The control board is equipped with both DSP (OMAP-L138) and FPGA (CYCLONE IV). The sampling and control implementation frequency is 12 kHz. Driver and protection boards are used to drive the semiconductors (i.e. Insulated Gate Bipolar Translators, IGBTs) and to protect the system once a fault is detected (i.e. overcurrent, etc.).

Table 3.3: PARAMETERS FOR THE POWER ELECTRONICS EMULATED SPS SYSTEM

Parameter	Value	Description
L_{vsg}	10mH	Output Inductance of the three-phase inverter
L_{rec}	5mH	Output inductance of the PWM rectifier
L_C	10mH	Inductance of the buck converter
C_1	165F	Capacitance of the UC

Table 3.4: EQUIVALENT ELECTRICAL AND MECHANICAL PARAMETERS OF VSG

Parameter	Value	Description
P_{sg}/Q_{sg}	1.5kW/1.5kVar	Rated active/reactive power
V_m	103V	Amplitude of the terminal voltage
$T_{d0}^{'}$	4.3s	Time constant of the generator damping
x_d	1.71	d-axis synchronous reactance
$x_d^{'}$	0.169	d-axis transient reactance
x_q	1.67	q-axis synchronous reactance
H	3.01s	Inertial
p	1	Number of pole pairs

The simulation results of the normal charging process are shown in figure 3.17. VSG is emulated by using the equivalent electrical and mechanical parameters listed in table 3.4. At t_1, the VSG is started. The initializing of the VSG lasts for about 15s. At t_2, The UC charging system is interacted with the VSG by operating the rectifier at the diode rectifier mode. At t_3, the PWM rectifier mode is turned on with the DC bus voltage stabilized at 110V. At t_4, the charging of the UC is started. The initial and desired UC voltage values are 24V and 30V, respectively. The responses of charging current (I_C) and voltage (V_C) of the UC are shown in figure 3.17. The charging process lasts about 350s. In order to better illustrate the control performance of the proposed controller on a three-phase machine, the *phase A* terminal voltage (v_{ma}), the *phase A* output current (i_{ma}) and the output currents in the *dq*-coordinate system of the VSG are shown in figure 3.17. The charging process introduces no overshoot on the VSG output currents and little impact on the amplitude of the VSG terminal voltages. Moreover, during this process, the system frequency response (f) shows little deviation. It directly reflects the significant advantage of the smooth charging process.

As can be seen from all of the above results, the effectiveness of the proposed controller has been demonstrated through extensive simulations.

DC MICROGRID CONTROL

4.1 Problem Description

DC microgrids have been widely used in many critical DC power applications such as shipboard power systems and aircrafts [54-55]. They are generally comprised of multiple distributed generators (DGs), distributed energy storage, and critical loads, etc. [56]. A DC microgrid greatly benefits from the integration of the emerging DC renewable energies (e.g., photovoltaic), DC storage units (e.g., batteries and supercapacitors) and DC loads (e.g., data centers) by avoiding additional AC/DC conversion stages [57]. Besides, DC microgrids also avoid the control challenges that exist in the AC microgrids, such as transformer inrush current, frequency synchronization, and reactive power control [58]. One typical structure of the DC microgrids is derived from connecting multiple convertor-interfaced DG sources in parallel, and then supplying DC power to multiple loads through a common DC bus [59]. Once the output voltage of the common bus is well maintained, the load sharing can be realized through adjusting the output current of each DG [60].

In order to achieve the safe as well as the efficient operation of a DC microgrid, two control objectives are usually considered. The first objective is to maintain the common bus voltage tracking a predefined reference under various loading conditions. The voltage tracking performance plays an important role for the loads. Conventional voltage regulation methods are mainly focused on the tracking performance during steady state and neglect the transient stability [61-62]. The outer disturbance such as a sudden load change may cause a large overshoot or drop on the transient voltage, which is harmful for the critical sensitive loads and may even result in unexpected false action of the protection system [63]. The second control objective is to realize fair load sharing according to the static capacities of DGs or the system operating cost [57]. The proper load sharing is important for DGs to avoid the overloading circumstance. Besides, the improved current regulation can also help to reduce the circulating current. Circulating currents, which are flowing back and forth among converters, can degrade the energy efficiency, cause unbalanced load sharing, and even damage the system components [64]. The circulating currents can be suppressed by regulating the output currents of DGs to the predefined

references. It is a great challenge to achieve theses control objectives well at the same time. Therefore, the designed controllers must be fast and accurate enough to provide the desired system performance under both transient and steady-state stages.

In [65], a centralized control system is proposed to coordinate the parallel operation of multiple converters in a DC microgrid. The model predictive control method is used for voltage regulation and load power sharing. The major problem of centralized control solutions is lack of flexibility and fault-tolerance capability. If the system topology changes, the entire control system has to be redesigned. Besides, the centralized control solutions are susceptible to the single-point-failures. Similar problem also exists in the master-slave control methods where the voltage regulation deteriorates in the case of any failure in the master control unit [66]. From this perspective, a hierarchical control structure as proposed in [67] is more reasonable where a centralized secondary/tertiary control and a decentralized droop-based primary control are used. However, the droop control has some significant drawbacks, for example the performance of voltage regulation degrades with the increase in load and the load sharing property becomes inaccurate with the inclusion of unbalanced system parameters [60]. Thus, an additional secondary controller is usually needed to make the adaptive adjustment on droop control as introduced in [68] and [69]. But it indirectly increases complexity of the control system. Other types of advanced non-droop control methods have also been studied in the past years. In [59], a robust controller is designed to maintain the stability of DC microgrid under the disturbance of a fault. The controller is designed based on a simplified small signal model with known constant power loads (CPLs). The assumption of measureable CPLs can be found in many fundamental studies of various DC power networks applications including automotive [70] and marine systems [55] etc. Different control techniques, e.g., synergetic control, feedback linearization, backstepping and linear quadratic Gaussian, are also applied and compared in the DC microgrids with CPLs [71, 72]. However, the assumption of known CPLs has a strong limitation and cannot cover all situations in the practical applications. If the load demand deviates from the set point, the neglecting of load change will affect both static and dynamic control performance.

Moreover, all of above existing methods has no controllability on the transient responses so that large disturbances can be seen during the normal operating change of system [64-

72], which leads to a big challenge for the protection system [63].In this paper, a novel decentralized control algorithm is designed for the DC microgrids. The proposed control scheme integrates the function of both secondary and primary control to realize the voltage regulation and proper load sharing at the same time. The output-constrained control problem of a DC microgrid is formulated to ensure that the tracking error of voltage is always within the predefined time-varying bounds. Besides, a fair load sharing can be realized according to the static capacities of DGs. During the control design, the original output constrained system is first transformed to an unconstrained one by using an error transformation technique. A voltage controller is then designed based on the transformed system using a backstepping method. According to the standard Lyapunov synthesis, if the convergence of the error tracking control of the transformed system can be guaranteed, the transient response of the original system will always be under bounded. Once the common bus voltage is maintained, the load sharing can be realized by adjusting the output currents of DGs. Considering the difficulty of measuring the dynamic load, the load current is estimated based on the measured output voltage responses. As the output currents reaching the corresponding references, the proper load sharing can be achieved and the circulating currents can be minimized.

4.2 Modeling of DC Microgrid

In this study, the converter-interfaced microgrid model with LC output filter is used [73]. The topology of a DC microgrid with *n* DGs is shown in figure 4.1. Several different DGs are connected to a common DC bus through power converters and supply electric power to various loads. Due to the fast dynamic responses of converters, the overall system dynamic can be reflected on the LC filters and expressed as

$$\begin{cases} \dot{v}_o = \dfrac{\sum_{j=1}^{n} i_j}{\sum_{j=1}^{n} C_j} - \dfrac{1}{\sum_{j=1}^{n} C_j} i_{load} \\ \dot{i}_j = -\dfrac{1}{L_j} v_o - \dfrac{R_j}{L_j} i_j + \dfrac{1}{L_j} v_j, \; j = 1,2,...,n \end{cases} \tag{4.1}$$

where v_o is the DC bus voltage of the system and i_{load} is the current of the loads in total. i_j is the current of output filter and v_i is the control input of converter #*j*. L_j and C_j are the

inductance, and capacitance of the LC output filter #j. R_j is the parasitic resistance of the inductors.

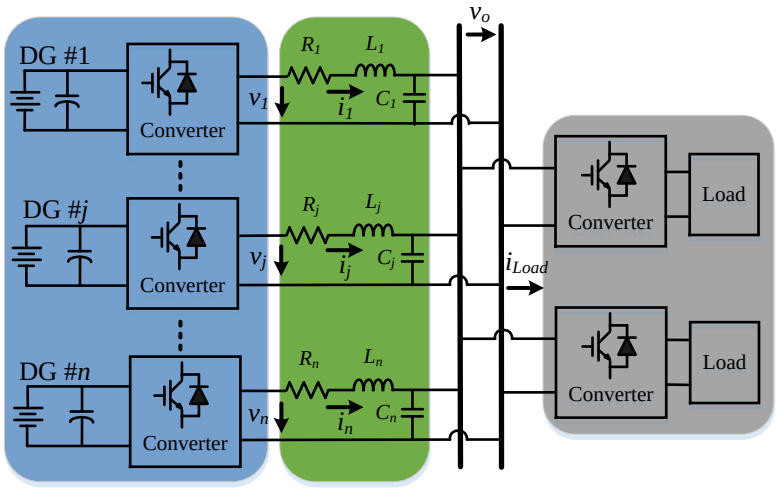

Figure 4.1 The topology of a typical DC microgrid.

One major control objective of this study is to ensure the output bus voltage v_o track a desired output trajectory v_{ref} during steady operating. More strictly, in order to maintain the designed voltage quality for varying loads during the transient time, the output voltage is required to stay within user-defined constraints, i.e.,

$$\underline{v}_o \le v_o \le \bar{v}_o \tag{4.2}$$

where $\underline{v}_o$ and $\bar{v}_o$ are the lower and upper bounds of the output voltage v_o, which can be arbitrarily selected depending on applications. Furthermore, it is worthwhile to mention that both bounds $\underline{v}_o$ and $\bar{v}_o$ can be set as either constants or time varying functions to satisfy certain system requirements.

Moreover, the load current i_{load} is also expected to be properly shared among n of DGs according to the predefined load sharing strategy, e.g., based on different DGs' capacities. The total generated current is finally equal to the total demand (i.e., $\sum_{j=1}^{n} i_j = i_{load}$) so that the circulating currents can be suppressed. In practical consideration, the following assumption is made in this paper.

Assumption 1: The load current i_{load} is unknown but is bounded as $|i_{load}| \le I$, where I is a known positive constant.

4.3 System Transformation

Because the conventional Lyapunov function based control methodologies cannot guarantee a bounded tracking error during the transient period [74], the constrained state-space model in (4.1) has to be transformed into an unconstrained one using a developed error transformation technique. It will be illustrated in next section that if the transformed system is stable, then the stability of the original system under the constraints satisfaction can be guaranteed.

First, for the transformation, define the tracking error as

$$e_v = v_o - v_{ref} \tag{4.3}$$

where the output voltage reference v_{ref} is a known constant. Since the derivative of a constant is zero ($\dot{v}_{ref} = 0$), the time derivative of the tracking error in (4.3) can be presented as

$$\dot{e}_v = \dot{v}_o = \frac{\sum_{j=1}^{n} i_j}{\sum_{j=1}^{n} C_j} - \frac{1}{\sum_{j=1}^{n} C_j} i_{load} \tag{4.4}$$

Then, the output bounds $\underline{v}_o$ and $\overline{v}_o$ can be transformed into the tracking error bounds $\underline{e}_v$ and $\overline{e}_v$ as

$$\underline{e}_v \le e_v \le \overline{e}_v \tag{4.5}$$

where $\underline{e}_v = \underline{v}_o - v_{ref}$ and $\overline{e}_v = \overline{v}_o - v_{ref}$. Next, the constrained tracking error e_v is transformed into a new variable ξ using a user-defined transfer function,

$$\xi = T(e_v, \underline{e}_v, \overline{e}_v) \tag{5.6}$$

This transfer function $T(\bullet)$ is designed to be smooth, strictly increasing with respect to e_v, and satisfy (4.7), which can be visualized in figure 4.2.

$$\begin{cases} \lim\limits_{e_v \to \overline{e}_v^-} \xi = +\infty \\ \lim\limits_{e_v \to \underline{e}_v^+} \xi = -\infty \\ T(0, \underline{e}_v, \overline{e}_v) = 0 \\ \text{For all } x \ge y,\ T(x, \underline{e}_v, \overline{e}_v) \ge T(y, \underline{e}_v, \overline{e}_v) \end{cases} \tag{4.7}$$

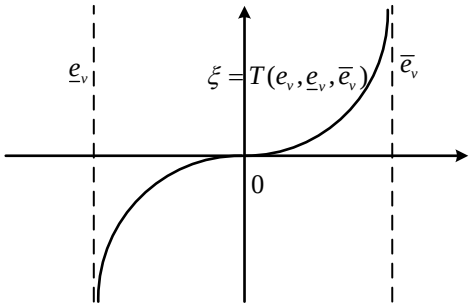

Figure 4.2 The demonstration of function $\xi = T(e_v, \underline{e}_v, \overline{e}_v)$.

In this paper, the transformation function is chosen as following for simplicity.

$$T(e_v, \underline{e}_v, \overline{e}_v) = \text{atanh}(\alpha) \tag{4.8}$$

where $\alpha = \dfrac{2e_v - \overline{e}(t) - \underline{e}(t)}{\overline{e}(t) - \underline{e}(t)}$. As can be seen, the transformation function in (4.8) satisfies all the requirements in (4.7). Moreover, by defining $T^{-1}(\bullet)$ as the inverse function of $T(\bullet)$ with respect to e_v, one can have

$$e_v = T^{-1}(\xi, \underline{e}_v, \overline{e}_v) \tag{4.9}$$

which has a unique solution when e_v is bounded according to (4.5). Therefore, as long as ξ exists, the output voltage tracking error e_v constraint in (4.5) is held. Notice that the transformation function (8) is differentiable on $e_v \in (\underline{e}_v, \overline{e}_v)$. If ξ exists, the time derivative of (5.6) can be expressed as

$$\dot{\xi} = a\dot{e}_v + b \tag{4.10}$$

where

$$\begin{cases} a = \dfrac{1}{1-\alpha^2} \dfrac{2}{(\overline{e}_v - \underline{e}_v)} \\ b = -\dfrac{1}{1-\alpha^2} \dfrac{(\dot{\overline{e}}_v + \dot{\underline{e}}_v)(\overline{e}_v - \underline{e}_v) + (2e_v - \overline{e}_v - \underline{e}_v)(\dot{\overline{e}}_v - \dot{\underline{e}}_v)}{(\overline{e}_v - \underline{e}_v)^2} \end{cases} \tag{4.11}$$

Recalling (4.10) and (4.4), the transformed system dynamics are given as

$$\begin{cases} \dot{\xi} = a\left(\dfrac{\sum_{j=1}^{n} i_j}{\sum_{j=1}^{n} C_j} - \dfrac{1}{\sum_{j=1}^{n} C_j} i_{load} \right) + b \\ \dot{i}_j = -\dfrac{1}{L_j} v_o - \dfrac{R_j}{L_j} i_j + \dfrac{1}{L_j} v_j, \; j = 1, 2, ..., n \end{cases} \tag{4.12}$$

Therefore, the original output constrained problem has been transformed into a typically unconstrained one, whose stability will be demonstrated in the following controller designs.

4.4 Performance Guaranteed Controller Design

In this section, the backstepping method [75] is utilized to develop the decentralized high-performance controllers for the DC microgrids. During the controller design, two control objectives are considered and achieved together coordinately. Then the system stability is proved via the standard Lyapunov synthesis. Since the proposed controller does not require to measure the accurate load current, the following reasonable assumption has been taken in this paper.

Assumption 1: the load current and its change rate are unknown but bounded as,

$$\begin{cases} \left| i_{load} \right| \le I_0 \\ \left| \dot{i}_{load} \right| \le I_1 \end{cases}$$

where I_0 and I_1 are positive constants.

4.4.1 Decentralized Control Design

According to the back-stepping principle, two steps are required to develop the controller based on the transformed system dynamics in (4.12).

In the first step, consider the following Lyapunov function candidate

$$V_1 = \frac{\sum_{j=1}^{n} C_j}{2} \xi^2 \tag{4.13}$$

Taking the time derivative of (4.13) and substituting (4.12), it becomes

$$\begin{aligned} \dot{V}_1 &= \sum_{j=1}^{n} C_j \xi \dot{\xi} = \xi \sum_{j=1}^{n} C_j \left(a\dot{e}_v + b \right) \\ &= \xi \left[a\left(\sum_{j=1}^{n} i_j - i_{load} \right) + b \sum_{j=1}^{n} C_j \right] \end{aligned} \tag{4.14}$$

Now, if we define the reference of demand current for DG #j as i_j^* after the corresponding load sharing, then the output current tracking error of DG #j can be defined as

$$e_{Lj} = i_j - i_j^* \tag{4.15}$$

Based on (4.15), the total demand current reference I^* ($I^* = \sum_{j=1}^{n} i_j^*$) can be designed as

$$I^* = -\frac{b}{a} C - k_i \frac{\xi}{a} + \hat{i}_{load} \tag{4.16}$$

where $C = \sum_{j=1}^{n} C_j$ and k_i is a positive constant. $\hat{i}_{load}$ is the estimation of the load current i_{load}, and its updating law follows the projection function in (4.17) as

$$\dot{\hat{i}}_{load} = \begin{cases} -\gamma_L a\xi, 0 < \hat{i}_{load} < I_0 \\ 0, \hat{i}_{load} = 0 \ and \ \xi > 0 \\ 0, \hat{i}_{load} = I_0 \ and \ \xi < 0 \end{cases} \tag{4.17}$$

where γ_L is a positive adaption gain.

According to (4.17), the current reference i_j^* for each DG #j can be redesigned as

$$i_j^* = p_j I^* \tag{4.18}$$

where p_j is a positive constant and satisfies $\sum_{j=1}^{n} p_j = 1$. It is worthwhile to mention that the current reference setting process does not require the extra measurements of loads. Instead, the total demand current reference I^* is calculated according to the system dynamic responses. Through the proper effort distribution, the overall load can be shared among the DGs. Thus, the detrimental influence of circulating currents can get minimized.

Remark 1: The proposed load sharing method is fully decentralized and does not require any communication among different DGs. Then the current reference tracking of i_j^* will be realized together with the voltage tracking design as follows. It will be demonstrated in the next subsections that as long as the output voltage v_o reaches the reference v_{ref}, the current tracking will be achieved, and the overall demand and supply balance ($\sum_{j=1}^{n} i_j^* = i_{load}$) will be guaranteed.

Based on (4.14-4.18), it yields that

$$\dot{V}_1 = -k_i \xi^2 + a\xi \sum_{j=1}^{n} e_{Lj} - a\xi \tilde{i}_{load} \tag{4.19}$$

In the second step, select a new Lyapunov function candidate as

$$V_2 = V_1 + \frac{1}{2\gamma_L} \tilde{i}_{load}^2 \tag{4.20}$$

Recalling (4.19), the time derivative of V_2 can be derived as

$$\dot{V}_2 = -k_i \xi^2 + a\xi \sum_{j=1}^{n} e_{Lj} - a\xi \tilde{i}_{load} + \frac{1}{\gamma_L} \tilde{i}_{load} \left(\dot{i}_{load} - \dot{\hat{i}}_{load} \right) \tag{4.21}$$

Based on the Assumption 1 and (4.17), it follows that

$$\dot{V}_2 \le -k_i \xi^2 + a\xi \sum_{j=1}^{n} e_{Lj} + \frac{2 I_0 I_1}{\gamma_L} \tag{4.22}$$

Next, consider the following augmented Lyapunov function V_3

$$V_3 = V_2 + \frac{1}{2}\left(\sum_{j=1}^{n} e_{Lj}\right)^2 \qquad (4.23)$$

Recalling (4.22), the first derivative of (4.23) can be written as

$$\dot{V}_3 \le -k_i\xi^2 + \frac{2I_0I_1}{\gamma_L} + \sum_{j=1}^{n} e_{Lj}\sum_{j=1}^{n}\left(\frac{a\xi}{n} - \frac{1}{L_j}v_o - \frac{R_j}{L_j}i_j + \frac{1}{L_j}v_j - \dot{i}_j^*\right) \qquad (4.24)$$

Based on (4.24), the controller for DG #*j* can be designed as

$$v_j = R_j i_j + v_o + L_j \dot{i}_j^* - k_v L_j e_{Lj} - \frac{1}{n} L_j a\xi \qquad (4.25)$$

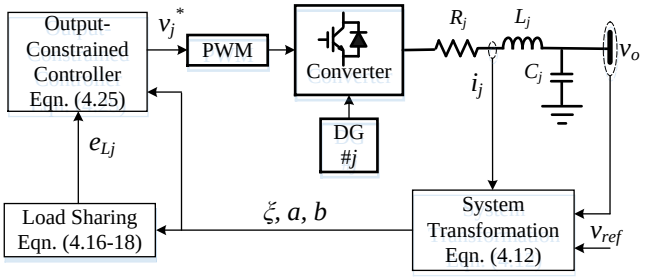

Figure 4.3 Closed-loop block diagram of the proposed control scheme

It should be noted that the control input in (4.25) is designed based on the global stability consideration of Lyapunov function in (4.24). The single item in (4.25) is able to guarantee the summation in (4.24) is negative definite. The closed-loop block diagram of the proposed DC microgrids control system is shown in the figure 3. For each local control #*j*, it first transforms an output-constrained system into an unconstrained one based on an error transformation technique. Then, a decentralized load sharing method is used to generate the output current reference based on the output voltage responses. Finally, an output-constrained controller is utilized to realize the desired load sharing as well as the high-performance voltage regulation. Because all the information needed by the controller can be measured locally, the overall control process can be realized without any communications.

4.4.2 Stability Analysis

Theorem 1 (Voltage Regulation and Load Sharing Control Design): Under the assumption 1, using the controller designed in (4.25), the voltage regulation and the load sharing (based on p_j) can be realized. Besides, the stability of the system can also be guaranteed.

Proof: First, substituting (4.25) into (4.24), one can have

$$\dot{V}_3 \le -k_i \xi^2 - k_v \sum_{j=1}^{n} e_{Lj}^2 + \frac{2I_0 I_1}{\gamma_L} \tag{4.26}$$

Then, recalling the Lyapunov functions in (13), (20), (23), it yields

$$V_3 = \frac{C}{2}\xi^2 + \frac{1}{2\gamma_L}\tilde{i}_{load}^2 + \frac{1}{2}\left(\sum_{j=1}^{n} e_{Lj}\right)^2 \tag{4.27}$$

Then it can be derived that

$$\dot{V}_3 \le -c_1 V_3 + c_2 \tag{4.28}$$

where $c_1 = \min\left\{\frac{2k_i}{C}, 2k_v\right\}$ and $c_2 = \frac{2I_0 I_1}{\gamma_L} + \frac{2c_1}{\gamma_L} I_0^2$.

According to the Lyapunov synthesis [74], one can conclude that all of signals in the closed-loop system (4.12) are bounded. Furthermore, the proposed control law (4.25) can guarantee that [74]

$$\lim_{t\to\infty} V_3(t) \le \frac{c_2}{c_1} \tag{4.29}$$

which implies that the transformed voltage error and current error can be made arbitrarily small by properly tuning of control gains. Combined with the definition of system transformation, the original voltage error is guaranteed to stay within the bounds. Therefore, both voltage regulation and load sharing can be achieved. ◊

4.5 Case Study of Performance Guaranteed Control in DC Microgrid

4.5.1 System Definition

The proposed control scheme is first tested on a 3 kW DC microgrid as shown in Fig.1. The simulation is conducted on both average and detail models of DC microgrids contain different numbers of DGs with RLC filters and DC loads using Simscape Power System toolbox of Matlab/Simulink. The total simulation is 0.25s under a sampling rate of 0.1ms. Instead of testing under a constant load, a larger step load change and a smaller step load change are simulated at time t=0.05s and t=0.15s, respectively, to evaluate the proposed control scheme under large disturbances. The output voltage reference v_{ref} is set to be 50 V constantly for DG #j. The system parameters and the control parameters are presented in table 4.1.

Table 4.1: PARAMETERS OF THE TEST SYSTEM

Item	Specification
Output resistors (R_1, R_2, R_3, R_4)	0.21, 0.2, 0.2, 0.19 Ω
Output inductors (L_1, L_2, L_3, L_4)	2.1, 2.0, 2.0, 1.9 mH
Output capacitors (C_1, C_2, C_3, C_4)	25, 25, 25, 25 μF
DC load	10 Ω (before 0.05s); 6 Ω (after 0.05s); 8 Ω (after 0.15s)
k_i	1
k_v	500
γ_L	400

The dynamic output error bounds are defined as:

$$\bar{e}_v = -\underline{e}_v = A + be^{-\frac{T}{\tau}} \tag{4.30}$$

where A, b and τ are user-defined constants. T is a transformed time variable, which satisfies the following conditions during the load change at time t=0.1s

$$\begin{cases} T = t, & 0 \le t < 0.05s \\ T = t - 0.05, & t \ge 0.05s \end{cases} \tag{4.31}$$

Next, two different cases, i.e., evenly load sharing condition and proportional load sharing condition, are conducted to evaluate the effectiveness of the proposed controller.

4.5.2 Case I: Evenly Load Sharing

In the first case, the even load sharing control condition is performed. Based on Table I, it means that four DGs would evenly share the 12.0 A load current before time t=0.05s, 20.0 A after t=0.15s, and 15.0 A after t=0.15s. Theoretically, under the even load sharing, each DG #j should generate an output current i_j=3.0 A before time t=0.05s, i_j=5.0 A after t=0.15s, and 3.75 A after t=0.15s. During the test, taking A=7, b=1 and τ=1/60 so that the voltage tracking error is bounded within ±8 V during the transient period.

In order to better evaluate the performance of the proposed controller, a droop-based PI controller proposed in [76] is utilized for comparison. The droop equation is given as

$$v_{ref} = v_n - d_j i_j + k_j i_{avr} \tag{2.26}$$

where v_n is the nominal voltage. $i_{avr} = \sum_{j=1}^{n} i_j / n$ represents the global average current. d_j and k_j are the positive droop gain which is decided by the load sharing property and satisfy d_j-k_j>0.

The control circuit diagram is shown in figure 4.4. It should be mention that although the control algorithm is claimed to be distributed, the communication between each controller is still required. Besides, the PI controllers have been well-tuned using the classic Ziegler-Nichols method combined with the try and error method [77]. The control parameters of PI controllers are given in table 4.2. Since the PI controller has no global situational awareness, it is very difficult to tune the appropriate gains of PI controllers to satisfy both steady state and transient requirements of microgrids.

Table 4.2: PARAMETERS OF THE DROOP-BASED PI CONTROLLER

Item	Specification
Proportional Gain of PI1	0.5
Integral Gain of PI1	80
Proportional Gain of PI2	0.5
Integral Gain of PI2	180
d_j	5
k_j (even load sharing)	1.25
k_j (proportional load sharing)	1.0, 1.0, 1.5, 1.5

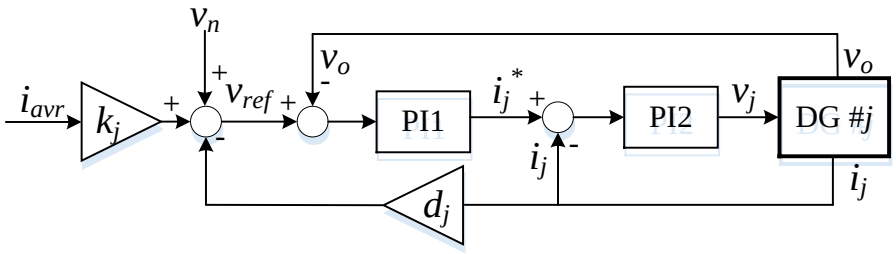

Figure 4.4 Block diagram of a droop-based PI controller

The system responses under droop-PI controller and the proposed output-constraint controller are shown in figure 4.5 to figure 4.7. Among which, the output voltage tracking error e_v is shown in the figure 4.5; the output currents i_js of DGs are given in figure 4.6; and figure 4.6 presents the load sharing error $\sum_{j=1}^{n} e_{Lj}$. As can be seen in figure 4.5, the severe load change introduces a large disturbance on the output voltage v_o. Even if the PI controller can achieve the desired control performance under steady-state stages, it has limited capability to manage the transient responses and the overshoot deviation is beyond 10 V. It is mainly because the voltage regulation and load sharing processes under PI control are not coordinated.

However, the voltage deviation under the proposed controller is much smaller and smoother during the transient period. Even under a larger disturbance, the voltage deviation e_v is still within the predefined bounds $\bar{e}_v$ and $\underline{e}_v$ rigorously. Then for a smaller disturbance, the voltage deviation e_v can always stay within the bounds as well. It is because the exact load current i_{load} has been delivered from DGs as shown in Figure 4.6. Thus, one can see that even though both controllers can realize the even load sharing, the output current i_js have better transient responses under the proposed controller. Therefore, the proposed controller is able to significantly suppress the circulating currents flowing back through the converters. It is true that such a big load change is a rare phenomenon in the reality, but it can be used to intuitively evaluate the effectiveness of the proposed controller. Moreover, the control inputs are presented in figure 4.7. Even though the proposed controller has stronger control efforts than that of PI controller, they are within a reasonable range and should be able to be applied in the practical equipment.

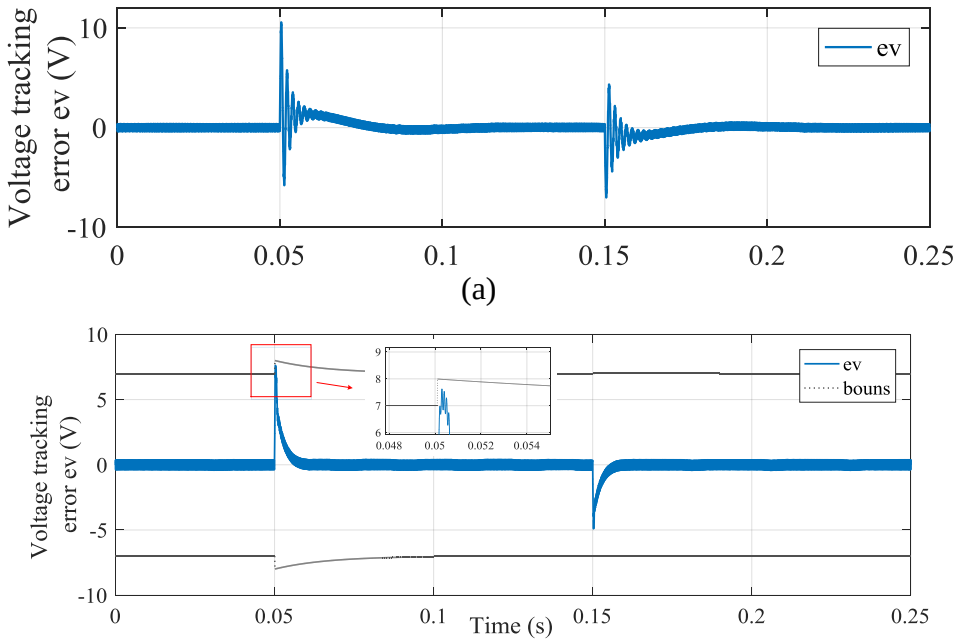

Figure 4.5 The responses of output voltage tracking error e_v under evenly load sharing condition: (a) PI controller; (b) proposed Controller

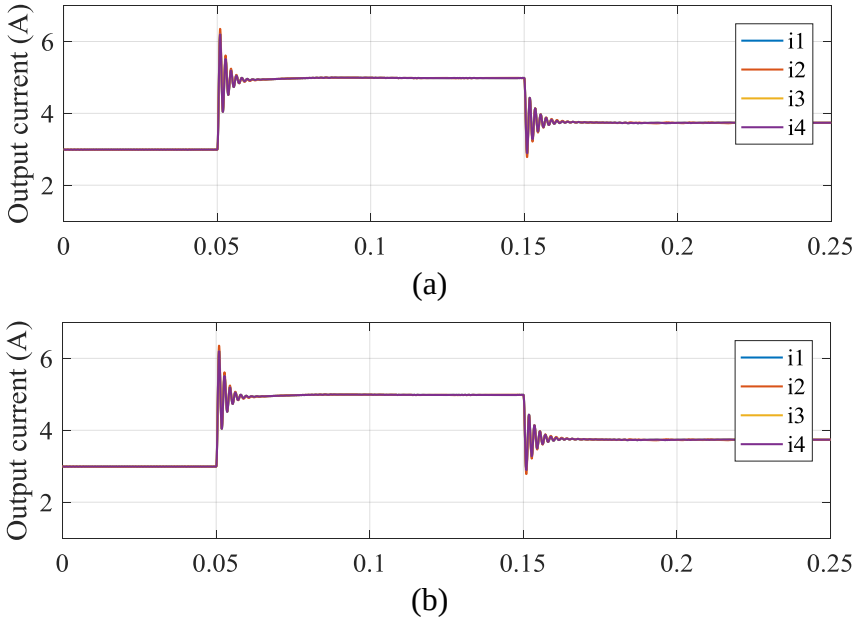

Figure 4.6 The responses of output current i_j under evenly load sharing condition: (a) PI controller; (b) proposed Controller

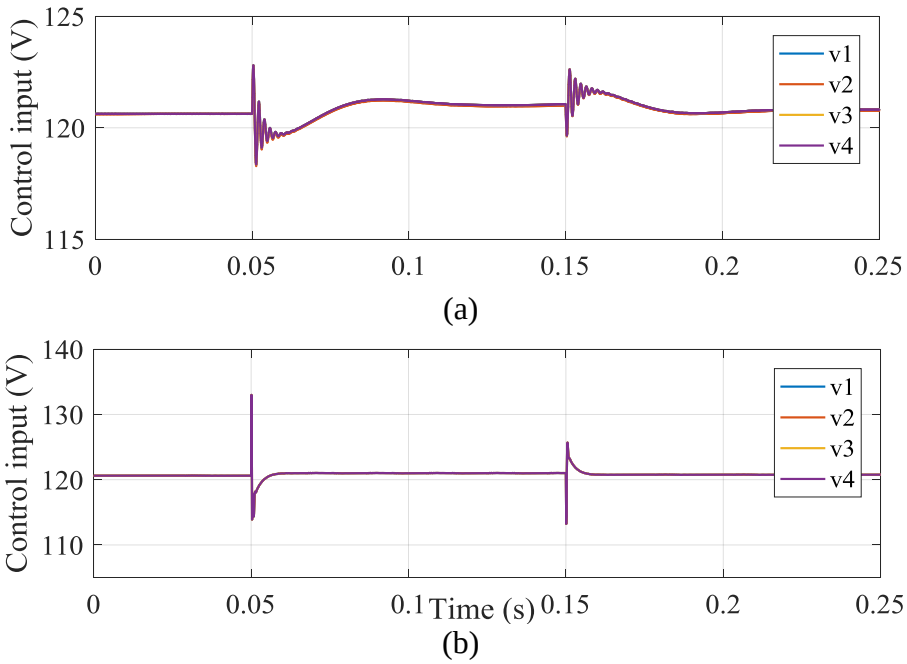

Figure 4.7 The responses of control input v_j under evenly load sharing condition: (a) PI controller; (b) proposed Controller

It has to be mentioned that the constraints placed on the voltage tracking error, i.e., $\bar{e}_v$ and $\underline{e}_v$, are usually determined by the physical constraints or practical requirements of a specific application. From the theoretical demonstration perspective, a series of experiments have been conducted over the operation point for different setups of $\bar{e}_v$ and $\underline{e}_v$ with the derivation of 0.2. The Main Sensitivity Index (MSI) in terms of the peak value $e_{v.\max}$ with respect to $\bar{e}_v$ and $\underline{e}_v$ is depicted in table 4.4. The observation can verify the robustness of the proposed controller. However, it is also worth mentioning that if $\bar{e}_v$ and $\underline{e}_v$ are made too close to 0, the system's stability might be compromised due to the limits on the control bandwidth.

Table 4.3: SENSITIVITY STUDY

$\bar{e}_v$ and $\underline{e}_v$ (V)	$e_{v,\max}$ (V)	MSI $e_{v,\max} / (\bar{e}_v - \underline{e}_v)$
7.9 and -7.9	7.2	45.6%
8.1 and -8.1	7.6	46.8%
8.3 and -8.3	7.5	45.3%
8.5 and -8.5	7.8	46.0%

4.5.3 Case II: Proportional Load Sharing

In the second case, the proportional load sharing control is performed. During the test, the capacity racial of four DGs are set to be 20%, 25%, 25% and 30%. Therefore, it means that the output current references i_j^* are 2.4 A, 3.0 A, 3.0 A and 3.6 A, respectively, before time t=0.05s; 4.0 A, 5.0 A, 5.0 A and 6.0 A, respectively, after time t=0.05s; and 3.0 A, 3.75 A, 3.75 A and 4.5 A, respectively, after time t=0.15s. During the test, taking A=7 and b=1 so that the voltage tracking error is bounded within ±8 V during the transient period.

The system responses under droop-PI controller and the proposed output-constraint controller are shown in figure 4.8 to figure 4.10. Among which, the output voltage tracking error e_v is shown in the figure 4.8 and the output currents i_js of DGs are given in figure 4.9. Again, the PI controller cannot provide the satisfactory transient performance during the load change, and a large voltage deviation can be observed in figure 4.8(a). Besides, it is important to notice that the droop-based PI controller has a slight steady-state error of output currents i_js under the proportional load sharing condition as shown in figure 4.9(a). This unavoidable error is due to the unbalanced system parameters, especially the resistors of the output filters, which has been well discussed in [78]. Even if this error can be compensated by tuning the droop gain based on the system parameters, it is not easy to be implemented and more complex algorithms might have to be used.

On the contrary, the proposed controller can still maintain the voltage deviation e_v within the predefined bounds $\bar{e}_v$ and $\underline{e}_v$ rigorously under the proportional load sharing condition as shown in figure 4.8(b). Besides, output currents i_js can achieve the proportional load sharing accurately as presented in figure 4.9(b). Then the control inputs comparison is shown in figure 4.10.

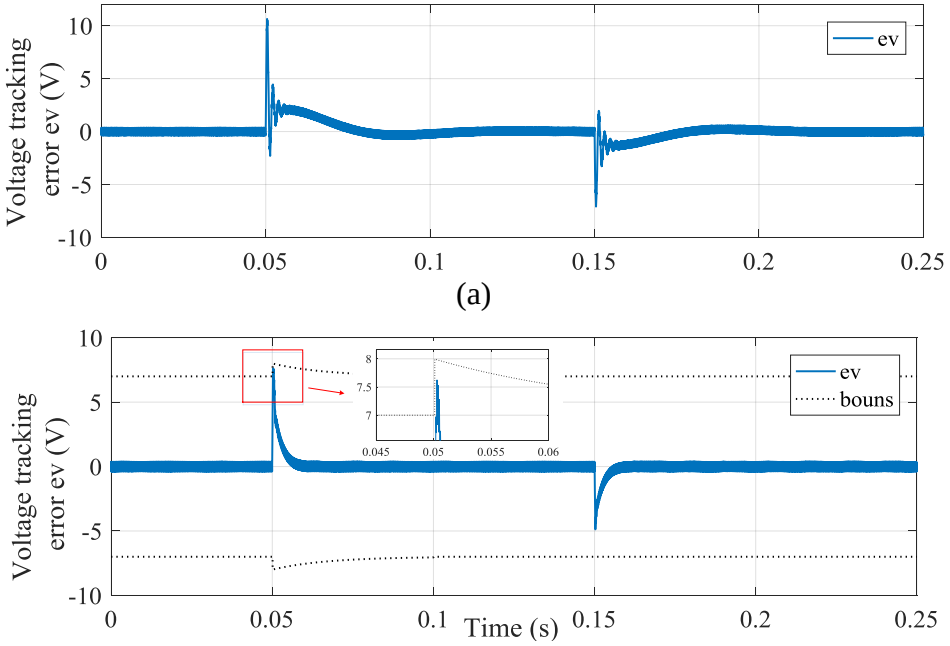

Figure 4.8 The responses of output voltage tracking error e_v under proportional load sharing condition: (a) PI controller; (b) proposed Controller

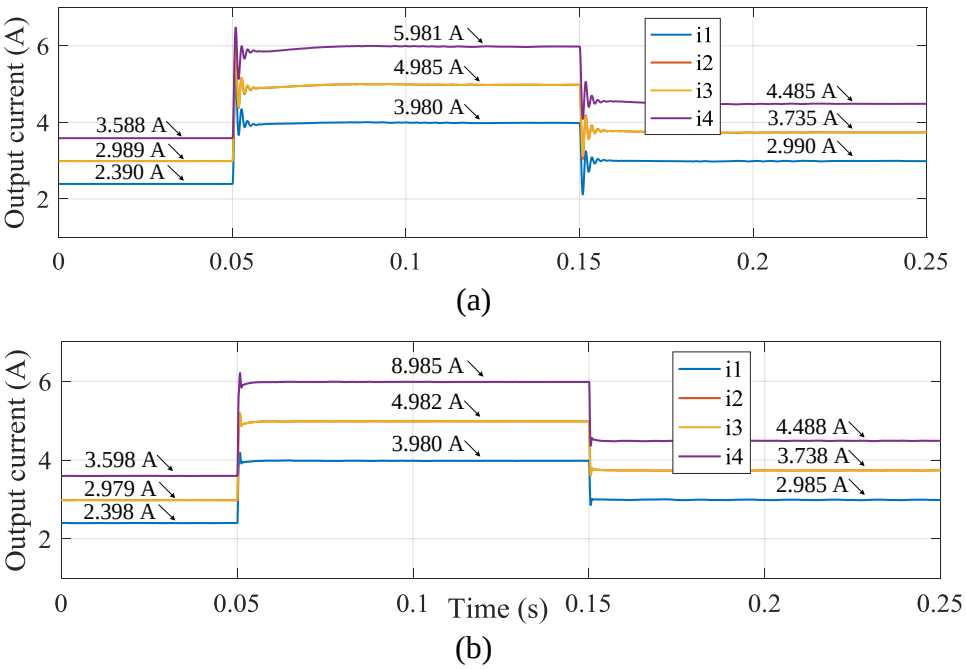

Figure 4.9 The responses of output current i_j under proportional load sharing condition: (a) PI controller; (b) proposed Controller

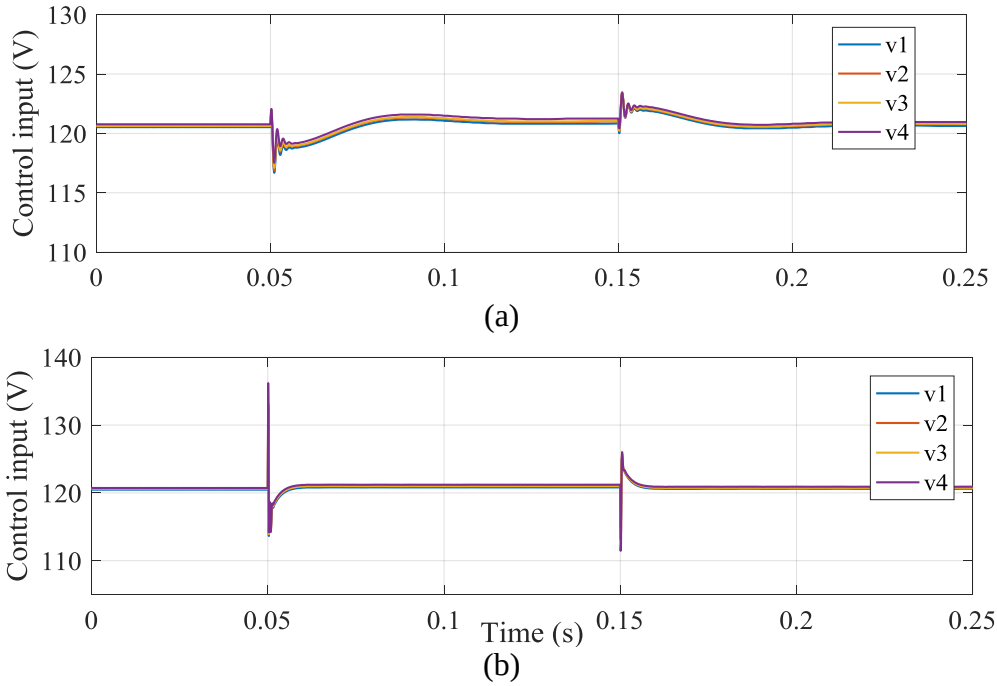

Figure 4.10 The responses of control input v_j under proportional load sharing condition: (a) PI controller; (b) proposed Controller

AC MICROGRID CONTROL

5.1 Problem Description

Inverter interfaced distributed generator (DG) is the basic building block of the rising microgrid paradigm [79]. Various types of DG such as photovoltaic, wind turbine and fuel cell are interfaced to the microgrid through power electronic converters/ inverters [80]. The inverter-interfaced DGs are flexible and have fast response speed. Such advantages make DGs easier to operate and control than conventional synchronous generators (SGs) [81]. However, controlling microgrids consisted of such DGs are challenging due to the negligible inertia, intermittent generations, together with severe load changes. If the challenges are not handled properly, the advantages and potentials of the inverter-interfaced microgrid cannot be fully unlocked. Since microgrid is one of the key components for the future smart grid, its performance somehow determines whether the successful deployment of smart grid can be achieved. Thus, operation and control of microgrids have been a hot research area over the last decade.

There are significant differences between traditional large- scale power systems and inverter-interfaced microgrids [82]. Traditional control solutions, which have been proven to be effective for large-scale power systems, cannot be introduced to microgrids without modifications [83]. The first and the easiest type of solutions is to increase the "virtual" inertia of the inverter-interfaced microgrids so that microgrids can behave similarly to the traditional power systems [84]. However, these solutions cannot fully unleash the potentials of microgrids in terms of flexibility and response speed. The second category of solutions is to model such microgrids as fully decoupled subsystems with impacts of neighboring subsystems formulated as measurable disturbances. At primary control level, droop and inner cascaded loops of proportional-integral (PI) controls are deployed to track the control references regulated by the upper secondary control level. Since microgrids are modeled similar to that of unmanned vehicle systems that have no physical connections among subsystems, many existing solutions in cooperative control [84-85], optimal control [85-87] and game theory [88-89] can be introduced. In the past years, there are many successful developments along this route. These works definitely promote researches on

microgrid controls and help to bridge the gaps among related societies, especially controls, power systems, and power electronics [84-89]. However, there are still many open problems that deserve further investigation.

In general, existing solutions that combine traditional primary control and advanced secondary control demonstrate comprised performance associated with several issues in modeling, control objective, and control strategy. First, the line dynamics should not be neglected during the modeling and control design process [91]. Most of the existing distributed control algorithms are based on the microgrid model with fully decoupled subsystems [93, 98]. However, the line impedances of microgrids are usually in the same range as the parameters of output filters of DGs [84, 91, 93]. Thus, merely ignoring the strong physical coupling to trade for achieving the distributed control design may result in large transient line current that could make the control ineffective and even trigger false protections. Secondly, the conventional control objective is always focused on regulating the capacitor voltage on the *LCL* output filters instead of the bus voltage where the loads are connected. Since the bus voltage is not under control directly, a small voltage deviation is unavoidable, which is undesired for the loads. Third, the droop-based primary control unnecessarily introduces the frequency deviations to the system [98]. For the conventional synchronous generator, there is a link between the electrical frequency and the mechanical rotating speed. However, such relationship does not exist in the inverter-interfaced DGs.

In order to better address the aforementioned challenges, several important factors have to be reconsidered for control design. Once the line impedances/dynamics are taken into the consideration during the control design, a microgrid can no longer be treated as an integration of fully decoupled subsystems. To improve the transient line currents performance of the interconnected subsystems, the basic communication among each control agent is necessary. The establishment of communication network renders the primary control not decentralized (communication-free) anymore. In fact, even though the conventional droop-based control methods are claimed to be decentralized, the centralized or inter-agent communications have been unavoidably used during the reference frame transformation as well as system frequency synchronization [91-93]. It has been demonstrated that moderate amount of inter-agent communications can greatly improve the control performance by introducing certain global situational awareness [100]. With

the rapid development of communication technologies, preference should not merely be given to the decentralized control designs. On the contrary, an appropriate balance should be evaluated between the control performance and the communication requirement.

In this section, two different methods are introduced to better coordinate the voltage and current regulation of inverter-interfaced microgrids. First, a switching mode control algorithm is developed, which can switch between the voltage control model and the current control mode based on the system requirements. Then, a consensus-based control algorithm is designed to indirectly reduce the transient line current while regulating the voltage.

5.2 Modeling of the Microgrid

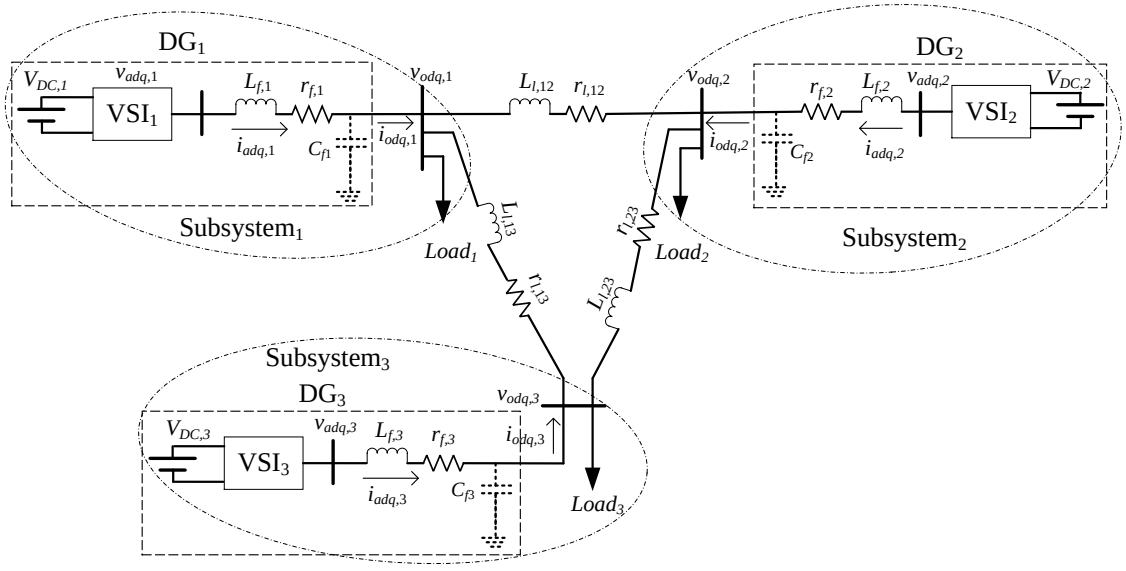

Figure 5.1 Schematic diagram of an inverter-interfaced microgrid.

Without loss of generality, figure 5.1 shows the schematic diagram of a microgrid consisted of three DGs with *L* or *LC* filters. For each DG, a voltage source inverter (VSI) is connected to a DC source that stands for the intermediate or direct output of a distributed renewable or traditional energy source. *L* or *LC* filter is connected between the inverter and the bus, and then connected to the rest of microgrids. The filters are important for current harmonic filtering and voltage stabilization [90]. Each DG may or may not have a load directly

connected to its output filter/bus. Multiple DGs and loads join together through power lines to form an integral inverter-interfaced microgrid.

Due to the fast response of power converters, the RLC components of output filter and power lines are actually dominating system's transient response. Thus, their dynamics should be included into the average control model, which is more suitable for control design and implementation than a switch-level model. For convenience, the model used in control design is summarized as follows.

The state equations governing the *L*-filter dynamics for i^{th} inverter are presented as:

$$\dot{i}_{ad,i} = -\frac{1}{L_{f,i}}(r_{f,i}i_{ad,i} + v_{od,i}) + \omega_n i_{aq,i} + \frac{1}{L_{f,i}}v_{ad,i} \tag{5.1}$$

$$\dot{i}_{aq,i} = -\frac{1}{L_{f,i}}(r_{f,i}i_{aq,i} + v_{oq,i}) - \omega_n i_{ad,i} + \frac{1}{L_{f,i}}v_{aq,i} \tag{5.2}$$

where $L_{f,i}$ is the inductance of *L*-filter; $r_{f,i}$ is the parasitic resistances of the inductor; ω_n is the nominal electrical angular velocity; $v_{od,i}$ and $v_{oqi,}$ are *dq*-components of the load bus voltage of the i^{th} subsystem ($v_{o,i}$); $v_{ad,i}$ and $v_{aq,i}$ are the *dq*-components of the output voltage of i^{th} DG ($v_{a,i}$).

Assuming that a power line is connecting buses *i* and *j*, its dynamics can be represented as:

$$\dot{i}_{ld,ij} = \frac{1}{L_{l,ij}}(-r_{l,ij}i_{ld,ij} + v_{od,i} - v_{od,j}) + \omega_n i_{lq,ij} \tag{5.3}$$

$$\dot{i}_{lq,ij} = \frac{1}{L_{l,ij}}(-r_{l,ij}i_{lq,ij} + v_{oq,i} - v_{oq,j}) - \omega_n i_{ld,ij} \tag{5.4}$$

where $r_{l,ij}$ represents the resistance of the power line linking buses *i* and *j*; $L_{l,ij}$ is the lumped inductance of the power line; $i_{ld,ij}$ and $i_{lq,ij}$ are the *dq*-components of line current ($i_{l,ij}$).

In order to roughly predict the load perturbation effects and obtain the representation of bus voltage for accurate voltage control [91], the virtual resistance method can be used as:

$$v_{od,i} = r_n(i_{ad,i} - i_{ld,i} - i_{Ld,i}) \tag{5.5}$$

$$v_{oq,i} = r_n(i_{aq,i} - i_{lq,i} - i_{Lq,i}) \tag{5.6}$$

where $i_{ld,i} = \sum_1^{n_i} i_{ld,ij}$ and $i_{lq,i} = \sum_1^{n_i} i_{lq,ij}$ are the *dq*-components of the overall line current leaving bus *i* ($i_{ldq,i}$) with n_i being the number of buses connected to bus *i*; $i_{Ld,i}$ and $i_{Lq,i}$ are the *dq*-

components of load current at bus i ($i_{L,i}$); and r_n is a large virtual resistance, whose value should be large enough to minimize any impact on system dynamics.

It worthies mentioning that if *LC* filters are used after DGs, the dynamic of bus voltage can be represented as

$$\dot{v}_{od,i} = \frac{1}{C_{fi}}(i_{ad,i} - i_{ld,i} - i_{Ld,i}) + \omega_n v_{oqi} \tag{5.7}$$

$$\dot{v}_{oq,i} = \frac{1}{C_{fi}}(i_{aq,i} - i_{lq,i} - i_{Lq,i}) - \omega_n v_{od,i} \tag{5.8}$$

Equations (5.1-5.8) represent the formulation of one subsystem, and a completed microgrid model is composed of multiple such subsystem models. Such model can represent a general class of microgrids whose loads are directly connected to the DG buses instead of intermediate buses. It should be noted that the above linear equations will result in a nonlinear control problem if the control objective is to regulate quantities that are represented as nonlinear functions of system states, e.g. output voltage ($V_{o,i}$) and active power.

5.3 Control Design Formulation

Currently, there are two popular control modes for microgrids, i.e. *V-f* control and *P-Q* control [92]. These two control modes target at different concerns or operating conditions. For *V-f* control, the control objective is to maintain the constant rms bus voltages and system frequency. For *P-Q* control, the control objective is to track the *P* and *Q* references that are calculated based on system-wide efficiency and static stability considerations. To counteract the impacts of unavoidable load change and inaccuracy during reference setting, adjustments based on predefined droop characteristics are usually deployed. The introduction of droop control may cause voltage and frequency deviations that have to request periodic correction by upper-level controller [81, 93].

There are significant differences between inverter-interfaced microgrids and SG-based large-scale power systems. For an SG, the physical rotor speed adjusts to charge or discharge its mechanical potential energy during supply-demand imbalance. The rotor speed reflects an electrical frequency based on the construction of SG. Since *f* is linked to *P*, it is necessary and reasonable to deploy *P-f* droop control in traditional power systems.

However, there is no such physical *P-f* coupling in the inverter-interfaced microgrids due to the decoupling of DC source and AC generation. Since the frequency of inverter-interfaced DG can be easily regulated around 60 Hz, using droop control to adjust frequency during load change unnecessarily increases frequency oscillations. If each subsystem adjusts its frequency reference separately, multiple frequencies will appear in the system during transient states. It not only disturbs the convergence of PLL, but also causes difficulty for frequency evaluation.

It is a common sense that energy efficiency (*P* and *Q* optimization) becomes secondary compared to stability (*V* and *f* regulation). In the proposed control design, the primary control objective is load bus voltage (*V*) regulations, and the secondary control objective is fair load-sharing (*P*). *f* reference is set to be a constant, and *Q* is not directly regulated. For the reference setting of bus voltage, the rms value is fixed and only phase angle is adjusted. In this way, the voltage can be well stabilized as the other critical quantity, i.e. *f*. The adjustment of the voltage phase angle considers both fair load-sharing and complexity of uncertain operating conditions. This control strategy full considers the priority of control objectives while trying to keep flexibility and efficiency. In order to guarantee fast and smooth tracking of the control references and avoid a surge of line current, novel control algorithm needs to be designed.

Based on above introduction, one can tell that the solution should have two control levels for larger time-scale and real-time coordination of subsystems, respectively. The upper-level secondary control is in charge of control reference setting while the lower-level primary control is responsible for control reference adjustment and tracking.

5.4 Distributed Control Design with Bounded Transient Line Current

5.4.1 Secondary Control Design

The objective of secondary control is to find the phase angles references (δ^*) of the bus voltages ($V_o \angle \delta$) based on operational constraints in a two-step procedure. First, generation references of the DGs (P_G^*) are decided based on a consensus-based distributed algorithm presented in [94]. Second, the generation references (P_G^*) together with desired bus

voltages (V_o^*) are used to decide the bus phase angles (δ^*). These two steps are separately introduced as follows.

As introduced in [94], the objective of fair load sharing is to find a common utilization level, which is decided according to the overall demand and maximum generation. The overall demand includes both demands of the loads and the estimated system-wide active power loss. The overall maximum generation is decided by the total predicted intermittent generations and the physical generation limit of non-intermittent generations. Since consensus algorithm can find the global average of distributed signals, it can be used to explore the average demand and average maximum generation through distributed communications. Once the DGs obtain these two quantities, they can calculate local utilization levels, which is same for all of DGs. By synchronizing the utilization level, fair load sharing can be realized and the impact of inaccurate generation prediction can be minimized.

After the generation references (P_G^*) are obtained, the corresponding voltage phase angles references (δ^*) have to be determined through power flow to realize the desired load sharing. To do that, the DG with the largest capacity is selected as the slack bus with flexible generations. Both AC and DC power flow can be realized in a distributed manner such as in [95]. Since slight inaccuracy is not as important as response speed, distributed DC power flow is a better choice for this purpose. In addition, DC power flow can be achieved within predetermined steps (time), which helps improve the reliability and certainty of solutions. Thus, it enables more timely control reference updating for large-scale microgrids.

5.4.2 Primary Control Design

Once the voltage phase angles are decided, the *dq*-components of the bus voltage references $v_{od,i}^*$ and $v_{oq,i}^*$ can be calculated according to (5.9).

$$\begin{cases} v_{od,i}^* = V_{o,i}^* \cos(\delta_i^*) \\ v_{oq,i}^* = V_{o,i}^* \sin(\delta_i^*) \end{cases} \tag{5.9}$$

where $V_{o,i}^*$ is the RMS voltage reference at bus *i*.

By tracking the control references ($v_{od,i}^*$, $v_{oq,i}^*$, and f^*=60 Hz), the primary control objectives (V and f regulation) can be well achieved and secondary control objective (P_G^*) can also be approached.

To better regulate the bus voltages, a feedback linearization based control algorithm is designed. The tracking errors of bus voltage can be defined as

$$\begin{cases} e_{od,i} = v_{od,i} - v_{od,i}^{*} \\ e_{oq,i} = v_{oq,i} - v_{oq,i}^{*} \end{cases} \tag{5.10}$$

Since $v_{od,i}^{*}$ and $v_{oq,i}^{*}$ are updated periodically, they can be treated as constants between control updating intervals. Based on (5.3-5.6), the dynamics of voltage tracking errors can be reformulated as

$$\begin{cases} \dot{e}_{od,i} = f(e_{od,i}) + B_{od,i} v_{ad,i} \\ \dot{e}_{oq,i} = f(e_{oq,i}) + B_{oq,i} v_{aq,i} \end{cases} \tag{5.11}$$

where $B_{od,i} = B_{oq,i} = \frac{r_n}{L_{f,i}}$, $f\left(e_{od,i}\right) = r_n \left\{ -\frac{1}{L_{f,i}}(r_{f,i} i_{ad,i} + v_{od,i}) + \omega_n i_{aq,i} - \omega_n i_{lq,i} - \frac{1}{L_{l,ij}}(-r_{l,ij} i_{ld,i} + v_{od,i} - v_{od,j}) - \dot{i}_{Ld,i} \right\}$

and $f\left(e_{oq,i}\right) = r_n \left\{ -\frac{1}{L_{f,i}}(r_{f,i} i_{aq,i} + v_{oq,i}) - \omega_n i_{ad,i} + \omega_n i_{ld,i} - \frac{1}{L_{l,ij}}(-r_{l,ij} i_{lq,i} + v_{oq,i} - v_{oq,j}) - \dot{i}_{Lq,i} \right\}$.

According to the theory of feedback linearization [96], the control signals can be designed as

$$\begin{bmatrix} v_{ad,i} \\ v_{aq,i} \end{bmatrix} = \begin{bmatrix} \frac{1}{B_{od,i}} \left[-f\left(e_{od,i}\right) - K_{od,i} e_{od,i} \right] \\ \frac{1}{B_{oq,i}} \left[-f\left(e_{oq,i}\right) - K_{oq,i} e_{oq,i} \right] \end{bmatrix} \tag{5.12}$$

where $K_{od,i}$ and $K_{oq,i}$ are positive design parameters.

Substituting designed control (5.13) into (5.11), the tracking errors can be represented as (5.13),

$$\begin{cases} \dot{e}_{od,i} = -K_{od,i} e_{od,i} \\ \dot{e}_{oq,i} = -K_{oq,i} e_{oq,i} \end{cases} \tag{5.13}$$

Since $K_{od,i}$ and $K_{oq,i}$ are positive design parameters, it is easy to demonstrate that tracking errors will converge to zeros asymptotically [97].

Above control algorithm is very similar to other feedback linearization based primary control algorithms that developed for microgrids control [98]. The only difference is with the control formulation (control model and control objectives). It is important to note that the algorithm is distributed in the sense that signals for subsystem control computation are all locally measurable.

Above control algorithm and most other primary control algorithms for microgrids have no control over transient line currents. Neither can any upper-level secondary control algorithms, which are only able to address steady-state constraints of line currents periodically at a larger time-scale. The unexpected transient line current surge makes tuning of protection system difficult and may cause huge losses due to false fault protections. For a well-designed microgrid, the line currents should always stay within their loadability limits during the normal operating conditions [99]. Thus the easiest solution for transient line current suppression is to restrict the line currents within reasonable constant bounds.

Based on current values of $i_{ld,ij}$ and $i_{lq,ij}$, their derivatives formulated as (5.3-5.4), and the selected time step (T_s), the next-step values of $i_{ld,ij}$ and $i_{lq,ij}$ can be estimated. Based on the estimated values, the line current constraint $i_{l,ij}^2 = i_{ld,ij}^2 + i_{lq,ij}^2 \le \bar{i}_{ij}^2$ is evaluated. Should the constraint be violated, the following control signals limitation is proactively activated.

A straightforward solution is to make the derivative of $i_{l,ij}^2$ negative. In this way, the combined range of the control inputs, i.e. $v_{ad,i}$ and $v_{aq,i}$, can be determined. The range is used to compare with the control signals calculated for voltage regulation (5.12). However, two vectors cannot be directly compared before certain norm function is introduced. Even after that, control adjustment based on norm comparison will still be a problem.

In order to perfectly solve this problem, complicated control algorithm has to be designed due to the strong coupling of subsystems. To reduce complexity, a simple heuristic solution is presented below. The control objective is not to limit $i_{l,ij}^2$, but to decrease the *dq*-components $i_{ld,ij}^2$ and $i_{lq,ij}^2$ simultaneously, while the line current constraint is not satisfied. It should be noted that the method is a sufficient condition rather than a necessary and sufficient condition. Deriving a necessary and sufficient condition is similar to find the perfect solution mentioned above, which is difficult for design and implementation. As can be seen later, the simplified method can generate the decouple bounds for control signals. Thus, subsequent control implementation becomes easy.

Based on (5.1-5.4), in order to lower/maintain $i_{ld,ij}^2$ and $i_{lq,ij}^2$ at the same time, the following two conditions need to be satisfied.

$$\begin{cases} d\left(i_{ld,ij}^2\right)/dt = 2i_{ld,ij}\dot{i}_{ld,ij} = f_{dl,ij}(\bullet) + g_{dl,ij}(\bullet)v_{ad,i} \le -\left|b_d\right| \\ d\left(i_{lq,ij}^2\right)/dt = 2i_{lq,ij}\dot{i}_{lq,ij} = f_{ql,ij}(\bullet) + g_{ql,ij}(\bullet)v_{aq,i} \le -\left|b_q\right| \end{cases} \tag{5.14}$$

where $f_{dl,ij}(\bullet) = -\frac{2r_{l,ij}}{L_{l,ij}}i_{ld,ij}^2 - \frac{2i_{ld,ij}}{L_{li,j}}\left(r_{f,i}i_{ad,i} - \omega_n L_{f,i}i_{aq,i} + L_{f,i}\dot{i}_{ad,i}\right) - \frac{2i_{ld,ij}}{L_{l,ij}}v_{od,j}$;

$f_{ql,ij}(\bullet) = -\frac{2r_{l,ij}}{L_{l,ij}}i_{lq,ij}^2 - \frac{2i_{lq,ij}}{L_{l,ij}}\left(r_{f,i}i_{aq,i} + \omega_n L_{f,i}i_{ad,i} + L_{f,i}\dot{i}_{aq,i}\right) - \frac{2i_{lq,ij}}{L_{l,ij}}v_{oq,j}$;

$g_{dl,ij}(\bullet) = \frac{2i_{lq,ij}}{L_{l,ij}}$; $g_{ql,ij}(\bullet) = \frac{2i_{ld,ij}}{L_{l,ij}}$, and $\left|b_d\right|$, $\left|b_q\right|$ are positive constants, and take 1.7 and 1.5, respectively.

Thus, the following two bounds on control signals need to be applied simultaneously to decrease transient line current.

$$\begin{cases} v_{ad,i} \le -g_{dl,ij}^{-1}(\bullet)\left[\left|b_d\right| + f_{dl,ij}(\bullet)\right] \equiv \bar{v}_{ad,i} \\ v_{aq,i} \le -g_{ql,ij}^{-1}(\bullet)\left[\left|b_q\right| + f_{ql,ij}(\bullet)\right] \equiv \bar{v}_{aq,i} \end{cases} \tag{5.15}$$

Based on the definitions of the $g_{dql,ij}$ and $f_{dql,ij}$, one can see that measurements of the local and neighboring subsystems are required to calculate the bounds of local control signals. This effort is necessary to restrict the transient line current. Once over line current is predicted, the bounds $\bar{v}_{ad,i}$ and $\bar{v}_{ad,i}$ of (5.15) are used to clamp the control signals calculated according to (5.12). In this way, transient line current can be restricted and this process does not have an excessive impact on voltage control performance.

5.4.3 Control Implementation

Implementation of the overall control solution is illustrated in figure 5.2. To initialize the consensus-based load sharing algorithm, load and maximum generation over the projected period are estimated. Finding the synchronized utilization level requires communications between subsystem controllers. After the convergence of the utilization level, generation references of all subsystems can be calculated. Based on generation references, bus voltage settings and power line parameters, distributed DC power flow is introduced to calculate the phase angle references of the bus voltages. The distributed operation also requires direct interactions of subsystem controllers. The phase angle references are adjusted in real-time based on a simple δ-P_G droop equation. The adjusted phase angle references together with RMS values of bus voltages are used to generate the *dq*-components of the bus voltage references.

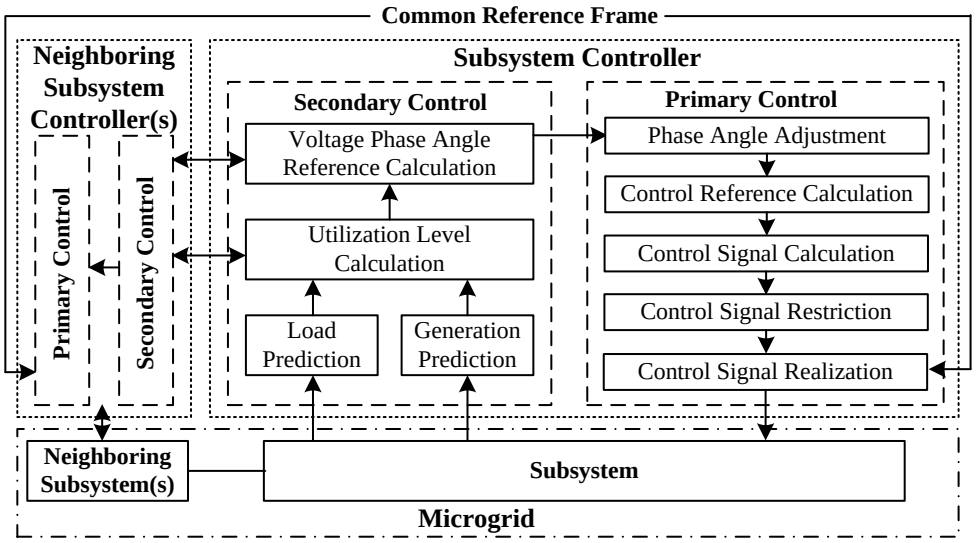

Figure 5.2 The flowchart diagram of the proposed microgrid control scheme.

During the normal operating conditions, the control objective is to make the bus voltages track the corresponding references. Whenever a line current bound violation is predicted, control signals are bounded to ensure an immediate decrease in line current. Then, *dq*-components of the control signals are converted to *abc*-components through *dq-abc* transformation. Based on a predefined common reference frame rotating at a constant frequency (60 Hz), the common phase angle reference can be found by the integration of frequency (ωt). Due to the fast response of inverter-interfaced DGs, the frequency reference track can be finished instantly. Therefore, each subsystem controller takes the general information of phase angle from the common reference frame to perform the *dq-abc* or *abc-dq* transformation. Finally, PWM signals are generated from the final control signals to realize the desired control performance.

To lower the computational complexity of the control algorithm, the next-step line current prediction can be replaced by simply comparing line current against a constant bound $\bar{i}_{ij}$. Once line current is larger than the bound, control signals will be bounded according to (5.15). It is true that this way of implementation will cause certain inaccuracy. However, the inaccuracy can be neglected due to several reasons. First, line current will not increase abruptly within a small time step T_s due to the inductance in the system. Second, the degrading of control performance is smaller than that due to imprecise model and uncertain operating condition. Third, the line current bound is usually set to a value slightly smaller

than the physical hard limit. Thus, the simplified method is implemented during the simulation evaluation.

5.5 Simulation Results

Table 5.1: PARAMETERS OF MICROGRID

Parameter	Value	Description
r_{f1}, r_{f2}, r_{f3}	0.50, 0.51, 0.52 Ω	Filter resistance
L_{f1}, L_{f2}, L_{f3}	4.21, 4.20, 4.215 *mH*	Filter inductance
r_{line12}, r_{line23}, r_{line31}	0.151, 0.152, 0.154 Ω	Line resistance
L_{line12}, L_{line23}, L_{line31}	0.42, 0.41, 0.414 *mH*	Line inductance
R_n	1000 Ω	Virtual resistance
K_p	1/1000 *rad/W*	Droop control gain
K_{od}	3.2	Control gain
K_{oq}	3.2	Control gain
ω_n	377 *rad/s*	Nominal angular velocity
T_s	$2e^{-5}$ *s*	Time step

In order to evaluate the performance of the proposed control solution, simulations with both the mathematical model and detailed model are carried out using Matlab/Simulink. Parameters of a 3-DG microgrid model and control gains are provided in table 5.1, which is modified based on [91]. The proposed solution is also compared to the conventional PI-based primary control algorithm [91]. In order to avoid the divergence and make the comparison illustrative, the PI-based primary control method is combined with the secondary control method proposed in this work.

5.5.1 Case I: Simulation with Mathematical Microgrid Model

During the primary control algorithm test, maximum generations are held fixed and a step change of constant load is simulated. Implementation details and performance of the secondary control algorithms can be found in the referred paper [94]. In this case, the secondary control algorithm is only activated once at the instant of time of load change.

The simulation starts from the steady state and a step load change is simulated at 0.1s. The maximum generations of three generator references are 1.30, 1.05, 0.90 per unit (*pu*) respectively, and held constant during the 3-second simulation. Three active power loads before and after the load change are 0.70, 0.60, 0.48 *pu* and 0.58, 0.80, 0.60 *pu*, respectively. The initial generation references are 0.712, 0.575, 0.492 *pu*, which is obtained based on the

estimated maximum generations. Based on DC power flow and the RMS voltage settings of 1.0, 1.0, 1.0 *pu*, the phase angles reference before load change are 0, 0.04, 0.01 *rad*. Under this simulation setting, the generation reference and phase angels reference after load change are 0.792, 0.636, 0.548 *pu* and 0.042, -0.028, 0.035 *rad*, respectively. After transients damped out under previous control, the actual generations with and without bound are 0.793, 0.640, 0.541 *pu* and 0.791, 0.660, 0.530 *pu*, respectively. The actual phase angels of both controllers (with and without bound) succeed in converging to the desired phase angle references after the load change (0.042, -0.028, 0.035 *rad*).

At first, the line current constraint is not applied. The corresponding responses of load bus voltages and power generation are shown in figure 5.3(a) and figure 5.3(b), respectively. As can be seen, both bus voltage and power generation are able to track their references well before and after the load change. In figure 5.3(c), a large line current surge (at $line_{12}$) can be observed at the beginning of load change. It is because current control only targets at voltage references tracking. Thus, in order to suppress the peak transient current, 1.5 *pu* can be selected as the line current bound for algorithm evaluation.

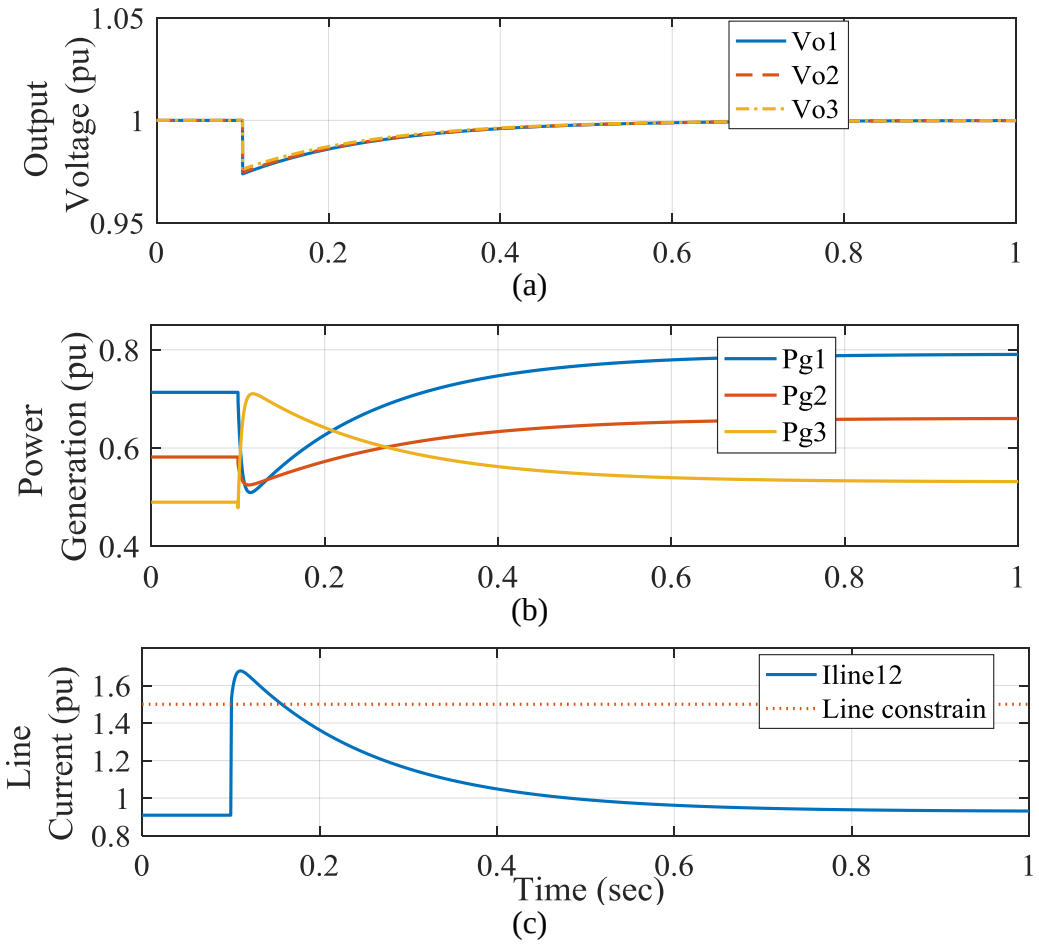

Figure 5.3 Simulation results of control scheme without considering line current constraint: (a). Load bus voltages ($v_{o,i}$); (b). Power generation ($P_{G,i}$); (c). Line current ($i_{l,i}$).

To maintain the transient line current i_{line12} within 1.5 *pu*, the corresponding control bound is applied on $v_{adq,1}$, which is in charge of the current limitation of this power line. The responses of bus voltage, power generation, line current, and control signals are shown in the four plots of figure 5.4, respectively. As can be noticed, both bus voltages and power generations succeed in tracking their corresponding references. Besides, the surge current on the power line gets significantly suppressed within 1.5 *pu*. As can be seen in the zoomed-in subplot of figure 5.4(c), the line current of i_{line12} touches the bound a few (about 20) times during the initial few time steps of load change. The period is so short that it cannot be noticed in the initial plot. Although the transient bus voltage has a larger drop comparing with the previous one, the overall performance is still within the acceptable range, e.g. 0.95~1.05 *pu* [96]. By comparing figure 5.4(b) and figure 5.3(b), one can see that generations converge in a different way under the line current limitation. It seems that

oscillations of generation are smaller due to the suppression of unnecessary current surges. The control signal $v_{ad,1}$ is subjected to the corresponding control bound $\bar{v}_{ad,1}$, and the related responses (dynamic bound, without bound, and with bound) are plotted in figure 5.4(d). It can be seen that the control bounds are triggered only about 20 times, which matches above observation with line current (i_{line12}). In addition to simplified microgrid model, the proposed control solution is also tested with a detailed microgrid model as shown in next subsection.

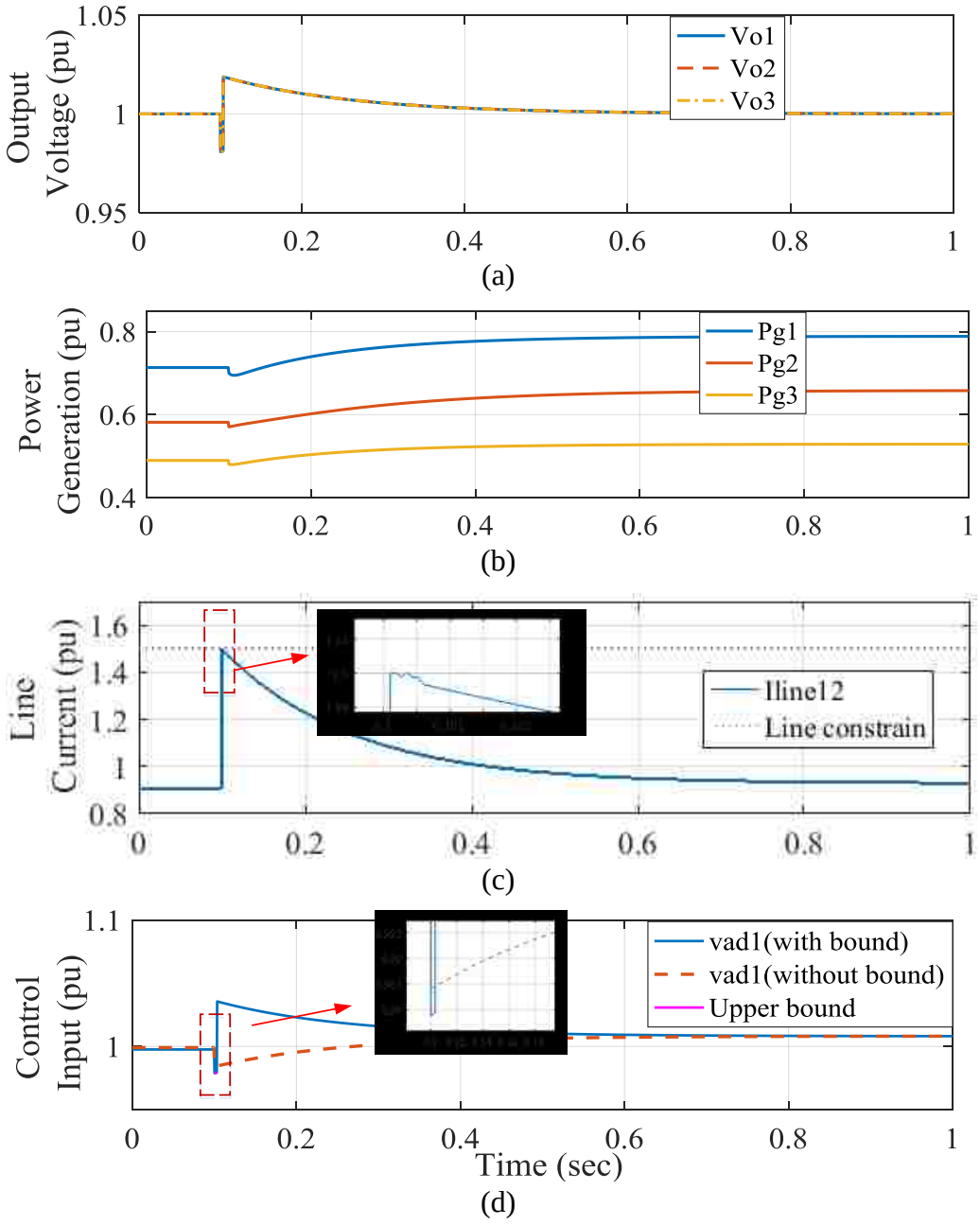

Figure 5.4 Simulation results of the proposed control scheme with considering line current constraint: (a). Load bus voltages ($v_{o,i}$); (b). Power generation ($P_{G,i}$); (c). Line current ($i_{l,i}$); and (d). Control signals.

5.5.2 Case II: Simulation with Switching-level Microgrid Model

In this case, more details are considered in the switching-level model, such as PWM generator, 2-level inverter and *dq-abc* transformation. In order to further reduce the total harmonic distortion (THD) of the system, LC filters are utilized in the simulation. Since the capacitor of the LC filter can be treated as one part of the load, there is no need to

modify the control algorithm. For some specific application, the decision on installation and size of the capacitor can be made based on actual loading condition and requirement on THD. In the simulation, LC filters with 20 μF capacitance are used. The control objectives remain to regulate the bus voltage while keeping the transient line current within 1.5 *pu*. The rest of system setting is also same as the previous cases. The simulation results including system frequency and line current are shown in figure 5.5, and the voltage responses are presented in figure 5.6, respectively. As can be seen, the simulation results on the detail switching level model match with those on the simplified model. The proposed controller is able to achieve the designed targets on voltage and current. In addition, due to the usage of LC filter, only a little bit harmonic appears in the detailed simulation. It also reflects the main advantages of the proposed control algorithm in terms of simplicity, generality, and flexibility.

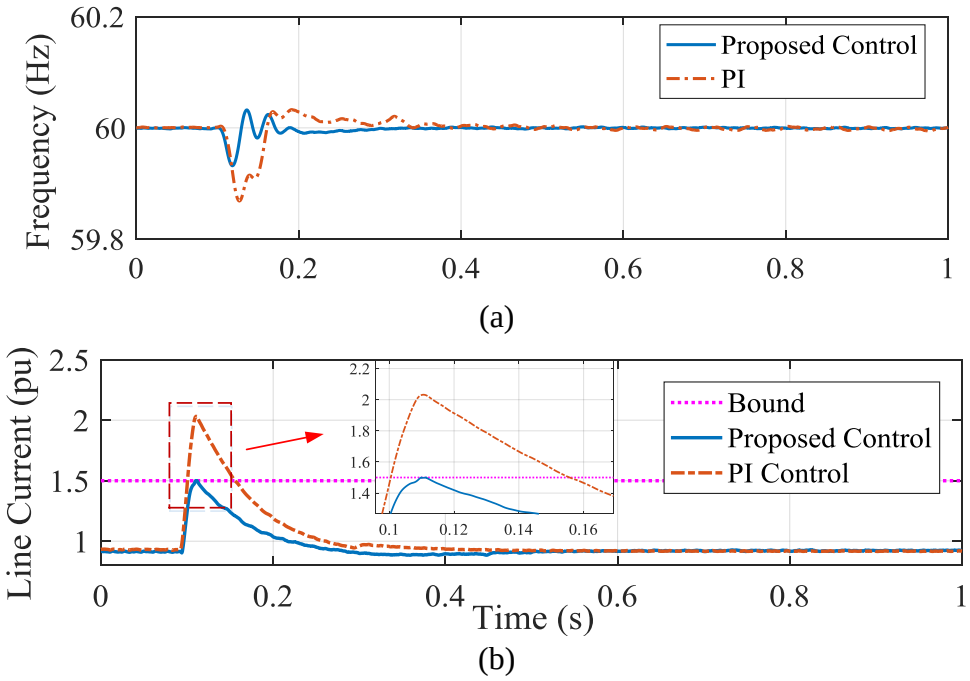

Figure 5.5 Simulation results on switching-level model: (a). System frequency (*f*); (b). Line current ($i_{l,i}$).

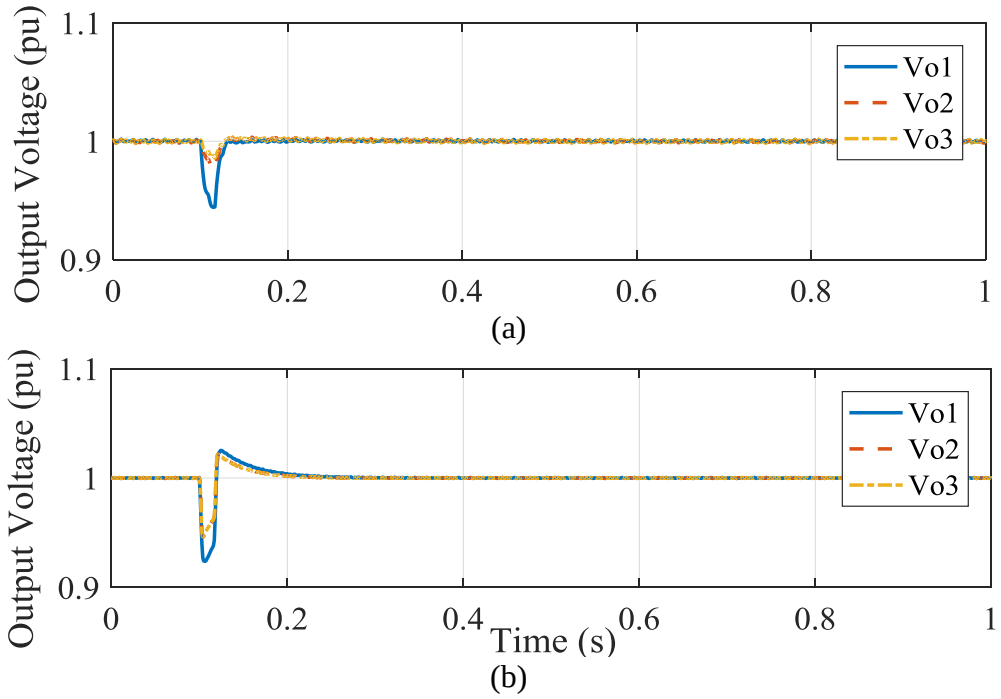

Figure 5.6 Bus voltage responses on switching-level model: (a). PI controller; (b). Proposed controller.

5.5.3 Case III: Simulation under System Fault

In this section, the proposed control algorithm is tested under the extreme system condition, i.e., system fault. In order to keep the system stable, as long as the voltage deviation is more than ±0.2 pu of the nominal value, the controller will be fixed in the voltage control mode. At the same time, the circuit breaker is supposed to be triggered to clear the fault line whenever the current is beyond 2.0 pu. The simulation results are presented in figure 5.7. There are several time-critical nodes that worth mentioning. At time 0.1s, a three-phase short circuit occurs between bus #1 and #2. Before time t_2, the controller has been switched to the current control mode and try to suppress the line current. At time t_2, the controller is fixed in the voltage control mode once the voltage deviation is beyond 0.2 pu. Circuit breakers are triggered at the point when line current reaches 2.0 pu at time t_1. After one cycle, at time t_3, circuit breakers of both ends are opened to clear the fault. As can be observed from the results, the proposed controller is able to well maintain the system performance even under the fault condition.

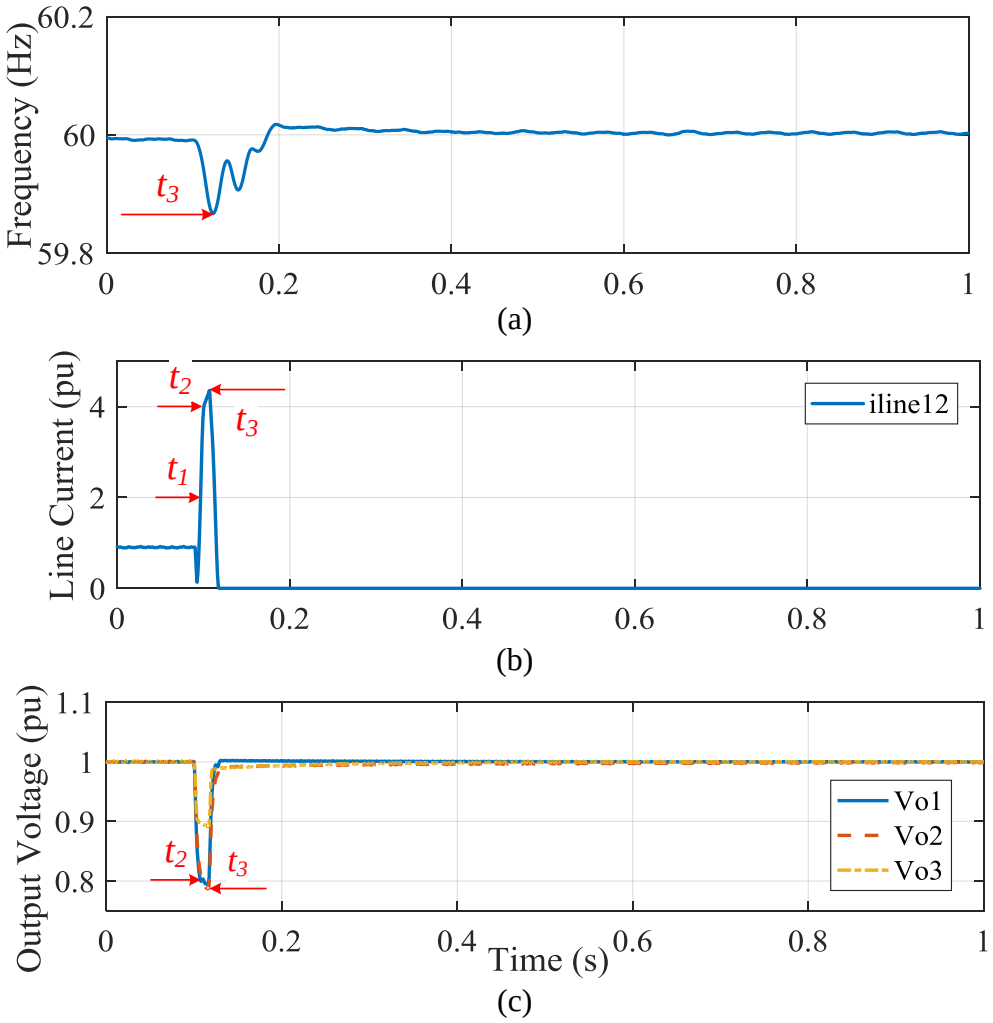

Figure 5.7 Simulation results on a switching-level model during system fault: (a). System frequency (f); (b). Line current ($i_{l,i}$); (c). Bus voltage ($v_{o,i}$).

Through the studies, the effectiveness of the proposed controller against model under model uncertainty is verified.

5.6 Consensus-based Primary Control Design

The primary control design as illustrated in Section 5.4 requires a forced switching of control mode during the transient period. This way of control implementation may cause unexpected disturbances, which is not preferred for microgrids operation. Therefore, a consistent consensus based controller without mode switching is developed in this section. Before proceeding, the relationship between line currents and bus voltage is analyzed first. The coordinated control design is then developed based on the theoretic basis.

5.6.1 Transient line current suppression.

Most of existing primary control algorithms for microgrids have no consideration of the transient line currents. Similar to most upper-level secondary control algorithms, which can only address the steady-state constraints in line currents periodically at a large time-scale [84, 98]. The unexpected transient line current surge raises the challenges to tune the protection system and may cause big losses due to the false action of protection devices. Therefore, when the primary controller is conducting the major control objectives of regulating the *V* and *f*, it should also be capable of suppressing the transient line current surge as much as possible. To ensure the transient line current limitation is satisfied, the Lyapunov stability analysis can be used to relate the line current $i_{l,ij}$ with output voltage $v_{o,i}$. Recall the linear dynamic (5.3) and (5.4), they can be rewritten as

$$\dot{i}_{ldq,ij} = A_{l,ij} i_{dq,ij} + e_{vdq,ij} \tag{5.16}$$

where $i_{ldq,ij} = \begin{bmatrix} i_{ld,ij} \\ i_{lq,ij} \end{bmatrix}$, $e_{vdq,ij} = \begin{bmatrix} v_{odi} - v_{odj} \\ v_{oqi} - v_{oqj} \end{bmatrix}$, $A_{l,ij} = \begin{bmatrix} -\frac{r_{l,ij}}{L_{l,ij}} & \omega_n \\ -\omega_n & -\frac{r_{l,ij}}{L_{l,ij}} \end{bmatrix}$.

Next, if selecting Lyapunov function candidate as $H(i_{ldq,ij}) = \frac{1}{2} i_{ldq,ij}^T i_{ldq,ij}$, the first derivative of the Lyapunov function candidate can be represented as

$$\dot{H}(i_{ldq,ij}) = \frac{1}{2} i_{ldq,ij}^T \dot{i}_{ldq,ij} + \frac{1}{2} \dot{i}_{ldq,ij}^T i_{ldq,ij} \tag{5.17}$$

Substituting (5.16) into (5.17), one can have

$$\begin{aligned} \dot{H}(i_{ldq,ij}) &= \frac{1}{2} i_{ldq,ij}^T (A_{l,ij} i_{dq,ij} + e_{vdq,ij}) + \frac{1}{2} (A_{l,ij} i_{dq,ij} + e_{vdq,ij})^T i_{ldq,ij} \\ &= \frac{1}{2} i_{ldq,ij}^T (A_{l,ij} + A_{l,ij}^T) i_{dq,ij} + \frac{1}{2} i_{ldq,ij}^T e_{vdq,ij} + \frac{1}{2} e_{vdq,ij}^T i_{dq,ij} \\ &\le -\frac{1}{3} \frac{r_{l,ij}}{L_{l,ij}} \left\| i_{l,ij} \right\|^2 + \frac{3 L_{l,ij}}{r_{l,ij}} \left\| e_{vdq,ij} \right\|^2 \end{aligned} \tag{5.18}$$

Assuming that the line currents need to be bounded as $\|i_{ldq,ij}\| \le i_{lB,ij}$, the line current constraint can be transferred into the bound of $e_{vdq,ij}$ based on the Lyapunov stability analysis as,

$$\left\| e_{vdq,ij} \right\| \le \frac{1}{3} \frac{r_{l,ij}}{L_{l,ij}} i_{lB,ij} \tag{5.19}$$

Note that the definition of $e_{vdq,ij}$ is the potential voltage difference between bus #*i* and bus #*j*. Therefore, equation (5.19) implies that the transient line currents can be suppressed if the terminal voltages (v_{oi} and v_{oj}) are converging along the same trajectory consistently. In this way, the $\|e_{vdq,ij}\|$ can be minimized with the transient line currents being suppressed significantly at the same time. Based on the above theoretical analysis, a consensus-based primary controller is designed in the next subsection. The output voltages are designed to converge in a consistent manner to suppress the transient line current.

5.6.2 Bus voltage regulation

To better regulate the bus voltages, a two-step feedback linearization based control algorithm is designed. According to (5.9), the tracking error of bus voltage can be defined as

$$\begin{cases} e_{vod,i} = v_{od,i} - v_{od,i}^{*} \\ e_{voq,i} = v_{oq,i} - v_{oq,i}^{*} \end{cases} \tag{5.20}$$

Since $v_{od,i}^{*}$ and $v_{oq,i}^{*}$ are updated periodically, they can be treated as constants between control updating intervals. Based on (5.7) and (5.8), the dynamics of voltage tracking errors can be reformulated as

$$\begin{cases} \dot{e}_{vod,i} = f(e_{vod,i}) + B_{vod,i} i_{ad,i} \\ \dot{e}_{voq,i} = f(e_{voq,i}) + B_{voq,i} i_{aq,i} \end{cases} \tag{5.21}$$

where $f\left(e_{vod,i}\right) = \frac{1}{C_{fi}}(-i_{ld,i} - i_{Ld,i}) + \omega_n v_{oqi}$, $B_{vod,i} = B_{voq,i} = \frac{1}{C_{f,i}}$ and $f\left(e_{voq,i}\right) = \frac{1}{C_{fi}}(-i_{lq,i} - i_{Lq,i}) - \omega_n v_{od,i}$. Then, using the feedback linearization technique, the voltage tracking controller can be derived as

$$\begin{cases} i_{adi}^{*} = B_{od,i}^{-1}\left\{\left[-f(e_{vod,i}) - K_{vd} e_{vod,i}\right] + \sum_j^n a_{ij}\left(e_{vod,i} - e_{vod,j}\right)\right\} \\ i_{aqi}^{*} = B_{oq,i}^{-1}\left\{\left[-f(e_{voq,i}) - K_{vq} e_{voq,i}\right] + \sum_j^n a_{ij}\left(e_{voq,i} - e_{voq,j}\right)\right\} \end{cases} \tag{5.22}$$

where K_{vd} and K_{vq} are positive control gains. n_i is the total number of DGs. a_{ij} is the coefficient of the information exchanged between agent #*i* and agent #*j*.

Based on a rigorous stability analysis, all of the voltage tracking errors will converge to the same value (i.e., zero) as long as the coefficients a_{ij} satisfy certain constraints [84-85]. The consensus items in (5.22) make sure that the output voltage of different DGs ($e_{vdq,ij}$)

converge in a consistent way, which is able to greatly decrease the surge of transient line currents. Next, targeting tracking of the *LC* filter current references i_{adi}^{*} and i_{aqi}^{*}, the current tracking errors can be attained as

$$\begin{cases} e_{iad,i} = i_{ad,i} - i_{ad,i}^{*} \\ e_{iaq,i} = i_{aq,i} - i_{aq,i}^{*} \end{cases} \tag{5.23}$$

The corresponding dynamics of the current tracking errors are

$$\begin{cases} \dot{e}_{iad,i} = \dot{i}_{ad,i} - \dot{i}_{ad,i}^{*} = f(e_{iad,i}) + B_{iad,i} v_{ad,i} \\ \dot{e}_{iaq,i} = \dot{i}_{aq,i} - \dot{i}_{aq,i}^{*} = f(e_{iaq,i}) + B_{iaq,i} v_{aq,i} \end{cases} \tag{5.24}$$

where $f\left(e_{iad,i}\right) = \frac{1}{L_{f1}}(-r_{fi} i_{adi} - v_{odi}) + \omega_n i_{aqi} - \dot{i}_{ad,i}^{*}$, $B_{iad,i} = B_{iaq,i} = \frac{1}{L_{f,i}}$ and $f\left(e_{iaq,i}\right) = \frac{1}{L_{fi}}(-r_{fi} i_{aqi} - v_{oqi}) - \omega_n i_{adi} - \dot{i}_{aq,i}^{*}$.

Then the practical control input can be designed as

$$\begin{cases} v_{ad,i} = B_{iad,i}^{-1}\left[-f(e_{iad,i}) - K_{id} e_{iad,i}\right] \\ v_{aq,i} = B_{iaq,i}^{-1}\left[-f(e_{iaq,i}) - K_{iq} e_{iaq,i}\right] \end{cases} \tag{5.25}$$

where K_{id} and K_{iq} are positive control gains.

The above design follows the similar procedure of other general feedback linearization based control algorithms that developed for microgrids [98]. The differences are with the control formulation (control model and control objectives) as well as the consideration of transient line currents. The flowchart shown in figure 5.8 illustrates how measurements and control input/output are transmitted and applied by the proposed control scheme. It is important to note that the algorithm is distributed in the sense that signals for subsystem control computation are all locally measured.

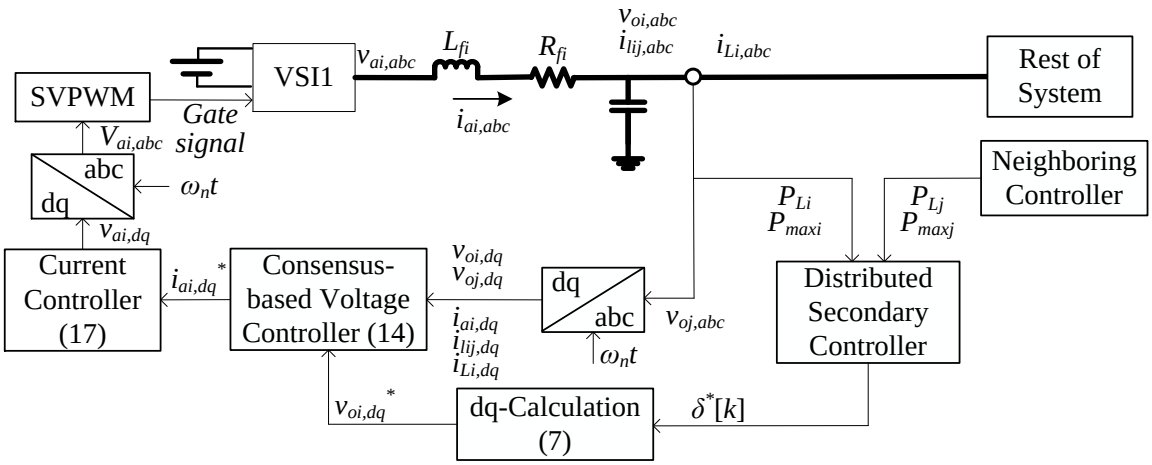

Figure 5.8 The flowchart of the control solution

5.7 Simulation Results of Consensus-Based Control Algorithm.

Table 5.2: PARAMETERS OF MICROGRID

Parameter	Value	Description
r_{f1}, r_{f2}, r_{f3}	0.50, 0.51, 0.52 Ω	Filter resistance
L_{f1}, L_{f2}, L_{f3}	4.21, 4.20, 4.215 *mH*	Filter inductance
C_{f1}, C_{f2}, C_{f3}	20, 20, 20 *uf*	Filter inductance
r_{l12}, r_{l23}, r_{l31}	0.151, 0.152, 0.154 Ω	Line resistance
L_{l12}, L_{l23}, L_{l31}	0.42, 0.41, 0.414 *mH*	Line inductance
K_{vd} , K_{vq}	250	Control gain
K_{id}, K_{iq}	25	Control gain
ω_n	377 *rad/s*	Nominal angular velocity
T_s	$2e^{-5}$ *s*	Sampling time

In order to comprehensively evaluate the performance of the proposed control solution, simulations are performed on both mathematical model and the detailed switch-level model using Matlab/Simulink. The detailed switch-level model is much more complicated than the mathematical model represented in (5.1-5.6) which makes it capable of testing the proposed solution under uncertain model dynamics. Parameters of a 3-DG microgrid model and control gains are provided in table 5.2, which is modified based on [91]. The proposed solution is also compared with conventional proportion-integration (PI) based primary control algorithm [91] through simulation.

5.7.1 Simulation with Mathematical Microgrid Model

During the primary control algorithm test, maximum generations are held fixed and a step change of constant load is simulated. Implementation details of the secondary control algorithms can be found in the referenced paper [94]. In this case, the secondary control algorithm is only activated once at the instant of time of load change.

The simulation starts from the steady state and a step load change is simulated at 0.5s. The maximum generations of three generator references are 0.9, 0.8, 1.0 per unit (*pu*), respectively and held constant during the 2.5-second simulation. Three active power loads before and after the load change are 0.51, 0.51, 0.60 *pu* and 0.61, 0.51, 0.60 *pu*, respectively. The initial generation references are 0.54, 0.48, 0.60 *pu*, which is obtained based on the estimated maximum generations. Based on DC power flow and the RMS voltage settings of 1.0, 1.0, 1.0 *pu*, the phase angles reference before load change are 0.006, 0.08, 0.0002 *rad*. Under this simulation setting, the generation reference and voltage phase angle references after load change are 0.58, 0.51, 0.64 *pu* and 0.001, 0.008, 0.06 *rad*, respectively.

Table 5.3: PARAMETERS OF PI CONTROLLER

	Voltage controller	Current controller
P gain	0.50	1.00
I gain	10.0	25.0

First, the PI-based controller presented in [91] is applied. The PI gains have been well-tuned using the classical Ziegler- Nichols method [77], and the PI gains of voltage and current controller are shown in table 5.3. Since the PI controller has no global situational awareness, it is very difficult to tune the appropriate gains of PI controllers to satisfy both local (bus voltage) and system-level (line currents) requirements of microgrids. The corresponding responses of load bus voltages v_o and power generation P_G of DGs are presented in figure 5.9(a) and figure 5.9 (b), respectively. As can be observed, both v_o and P_G are able to track their references before and after the load changes. The convergence of the reactive power demonstrated that the developed secondary control can also work together with the conventional primary control. In figure 5.9 (c), a large line current surge (at line_{12}) can be observed at the beginning of load change. The overshoot is during the transient stage over 0.65 *pu*, which might lead certain troubles to the protection system. In addition, both power generation and line current take a quite long time to converge due to

the interaction of each subsystem. Therefore, the only control objective of voltage regulation for the conventional controllers greatly limits their performance. The overall control inputs are given in figure 5.9 (d).

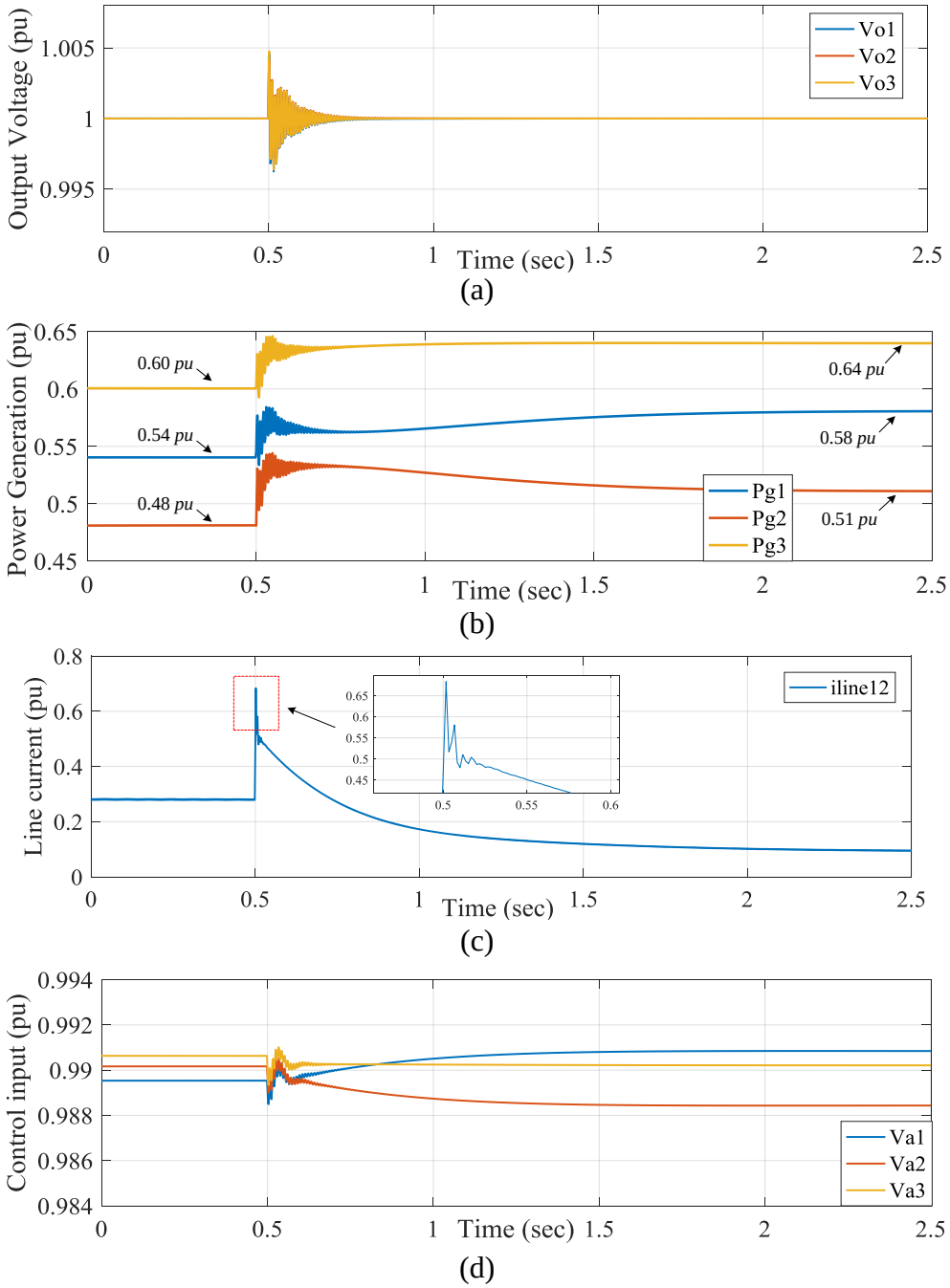

Figure 5.9 Simulation results of PI-based control scheme: (a). Load bus voltages (v_o); (b). Power generation (P_G); (c). Line current (i_l). (d). control inputs (v_a).

Next, the proposed controller is used under the same loading conditions. The responses of bus voltage, power generation, line current, and control signals are shown in the four plots of figure 5.10, respectively. It can be noticed that both voltages and power generations are able to track their corresponding references. In addition, the surge currents on the power lines get significantly suppressed. As can be seen in the zoomed-in subplot of figure 5.10(c), different consensus weight a_{ij} can reduce the transient line current surge to the distinct degrees. The overshoot of the transient line current is similar to the PI-based controller if a_{ij} =0, which means no consensus component is included in the primary control. But it can be reduced under 0.5 *pu* when a_{ij} =0.7. A comparison analysis of transient line current and bus voltage of using different control parameters are given in table 5.4. From simulation results, one can see that the overshoot of bus voltage just increases by 0.3% while the line current overshoot can be reduced as much as 20%. Since the improved control over line currents means a wider range of operating conditions and less faulty triggering of the protection system, the performance improvement is considered to be significant and the slight compromise over voltage regulation is worthful.

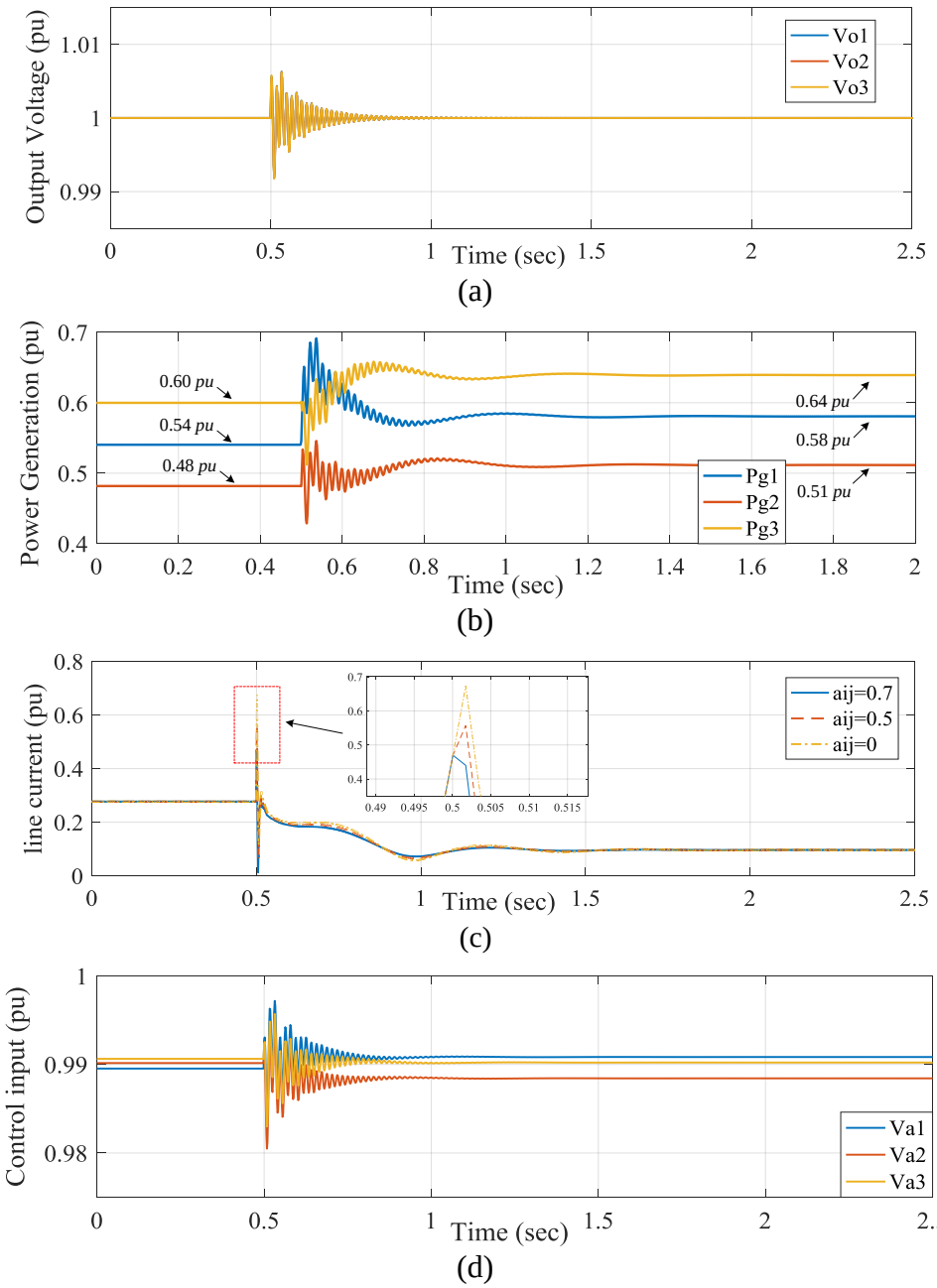

Figure 5.10 Simulation results of the proposed control scheme: (a). Load bus voltages (vo); (b). Power generation (PG); (c). Line current (i_l); and (d). Control signals.

Table 5.4: THE CONTROL PERFORMANCE COMPARISON RESULTS

PI controller		
Max. mag. of transient line current		Max. mag. of transient bus voltage
0.68 pu		0.005 pu
Proposed controller		
Weight a_{ij}	Max. mag. of transient line current	Max. mag. of transient bus voltage
0.3	0.67 pu	0.008 pu
0.5	0.56 pu	0.008 pu
0.7	0.47 pu	0.008 pu
0.9	0.46 pu	0.008 pu
0.3	0.67 pu	0.008 pu

By comparing figure 5.9(b) and figure 5.10(b), one can see that the power generations converge differently. The consensus-based primary controller not only suppresses the line current surge, but also accelerates the converging speed of the power generations. The control inputs are shown in the figure 5.10(d). It is true that the control inputs of the proposed controller have more severe changes compared with the PI controller. Therefore, it is necessary to evaluate whether such control inputs can be realized by the practical power inverters. In the next subsection, the proposed control algorithm is tested on a detailed switch-level model.

5.7.2 Simulation with Detailed 6-DG Microgrid Model

In this case, a larger-scale detailed microgrid model shown in figure 5.11 is used to evaluate the performance of the proposed control algorithm. More details are considered in the switching level model, such as the PWM, 2-level inverter and *dq-abc* transformations. This system consists of 6 DGs including 5 inverter-interfaced DGs and 1 SG. For the inverter-interfaced DGs, the proposed secondary/primary control method is used as in the previous cases. For the SG, a detailed genset model from Simscape Power Systems toolbox is applied including a turbine governor, an automatic voltage regulator, an exciter, and a power system stabilizer. Since this work is mainly focused on the inverter-interfaced microgrid control, only small percentage of generation from the SG is tested and the dynamic coordination problem of two different generation units is neglected. In order to better test the effectiveness of the proposed control algorithm, different line parameters given in Table 5.5 are used [91]. The rest of system settings are same as the previous cases.

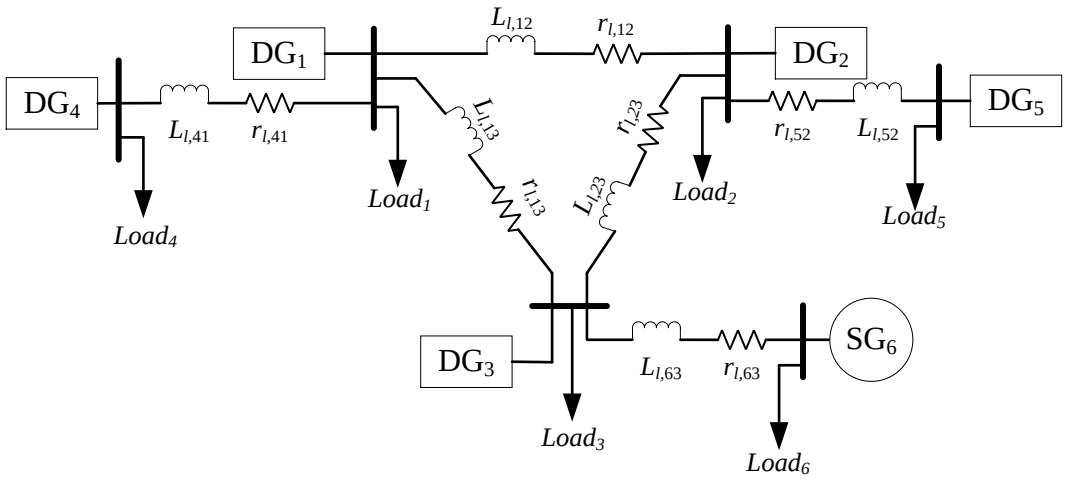

Figure 5.11 The topology of a 6-DG microgrid.

Table 5.5: PARAMETERS OF MICROGRID

Parameter	Value
r_{l12}, r_{l23}, $r_{l31,}$ r_{l41}, r_{l52}, r_{l63}	0.15, 0.16, 0.14, 0.17, 0.10, 0.20 Ω
L_{l12}, L_{l23}, $L_{l31,}$ L_{l41}, L_{l52}, L_{l63}	0.42, 0.35, 0.30, 0.45, 0.4, 0.41 *mH*

In order to better evaluate the effectiveness of the proposed control algorithm, a series of load changes including sudden and smooth load changes are conducted. At time 0.5 s, $load_1$ has a step change from 0.75 pu to 0.85 pu. Then, from time 1.5 s to 2.5 s, $load_2$ has a ramp up change from 0.52 pu to 0.60 pu. The overall load consumption of each subsystem is measured and shown in figure 5.12, and the maximum generation capacity of each local DG is assumed to be 1 pu, 0.8 pu, 0.8 pu, 0.6 pu, 0.6 pu and 0.2 pu. Based on the local load measurement and the predicted power generation, the utilization level shown in figure 5.13(a) is updated every 0.2 s incrementally using the distributed secondary control scheme as described in Section 5.4.1 [94-95]. Then, the references of phase angle δ_i^* acquired through the load flow are shown in the figure 5.13(b), which will be used to generate the bus voltage references $v_{od,i}^*$ and $v_{oq,i}^*$ on *dq*-axis. The fully distributed secondary control process can significantly increase the flexibility and stability of the system. The simulation results of the proposed primary controller are shown in the figure 5.14. As can be seen from figure 5.14(a) and figure 5.14(b), both system frequency and bus voltage can track the corresponding references well. Finally, the line current between DG_1 and DG_2 is shown in the Fig. figure 5.14(c). Similar to the previous cases, the proposed control algorithm can

effectively suppress the transient line current. Throughout the studies, the effectiveness of the proposed controller is verified.

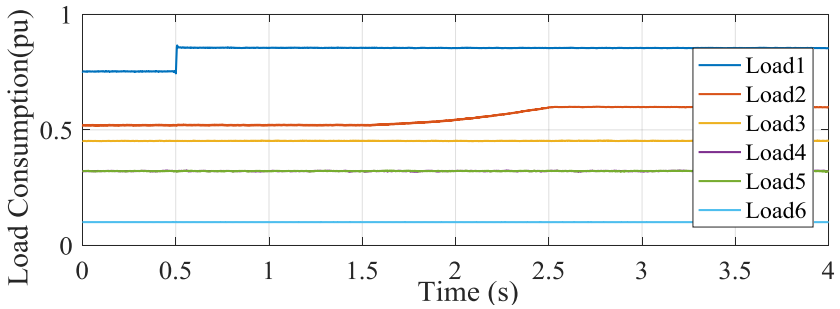

Figure 5.12 Load consumption change of each subsystem.

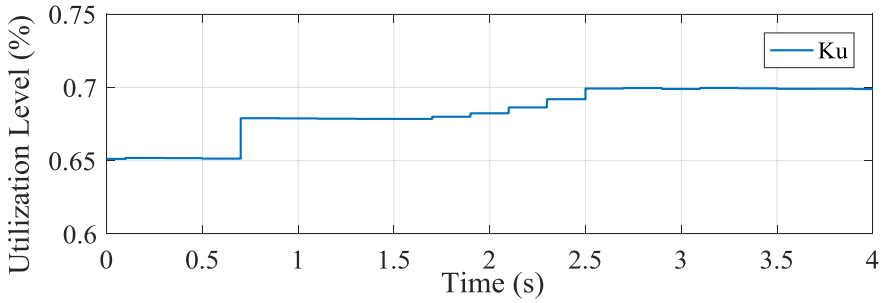

(a)

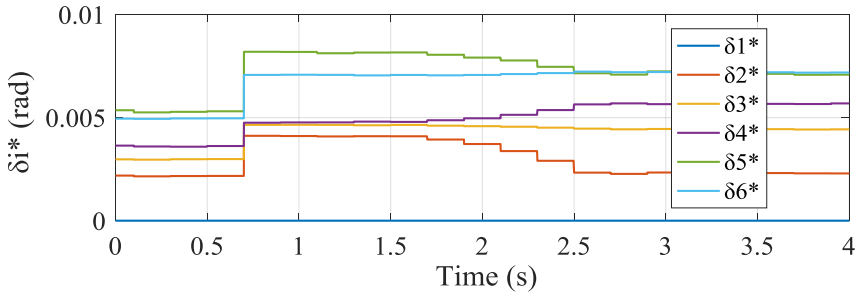

(b)

Figure 5.13 Evaluation of the secondary control: (a). Utilization level (%) of each DG; (b) Phase angle references δ_i^*.

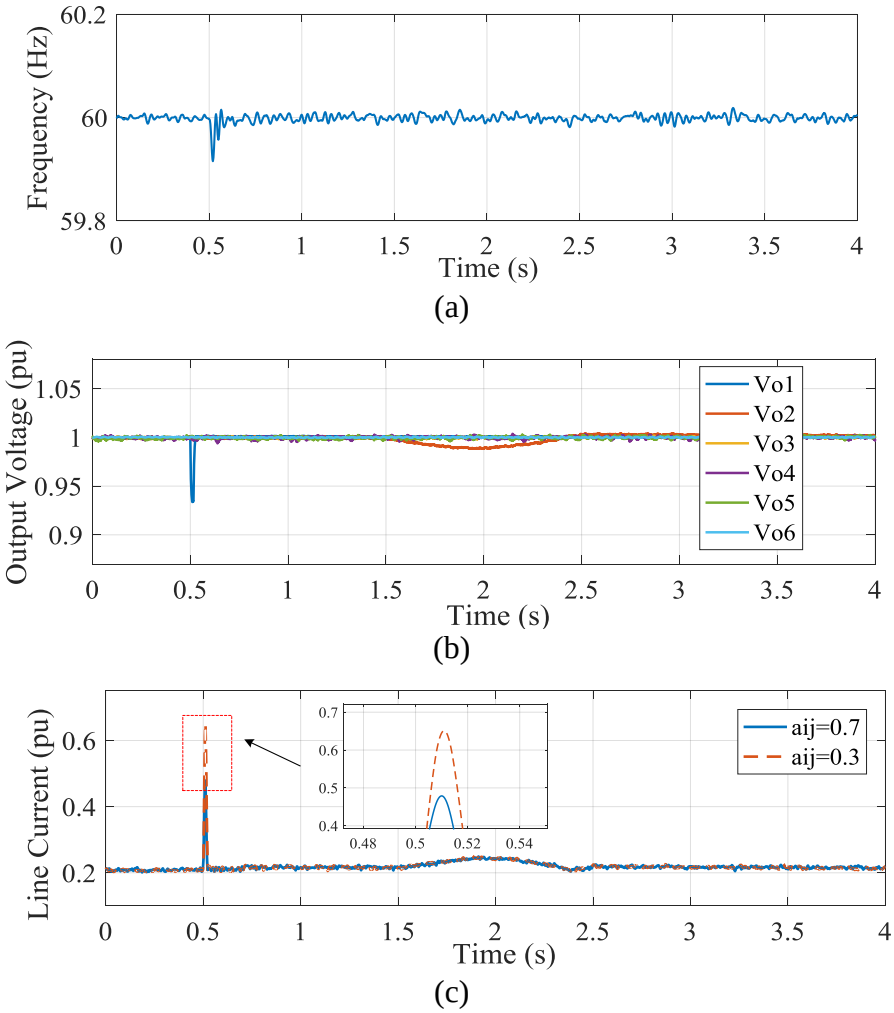

Figure 5.14 Simulation results of the proposed control scheme on 6-DG microgrid: (a). System frequency (f); (b). Load bus voltages (v_o); (c). Line current (i_l).

CONCLUSION

In our research, the advanced control problems of various energy systems including WAPS, SPS and DC/AC microgrids are explored. First, in order to proactively reduce the communication and computation burden of WAPS, an event-triggered control algorithm and a self-triggered control algorithm are proposed. Instead of updating measurements and controls periodically as the traditional control scheme, the proposed control schemes only require such updates when certain condition is triggered. Then, targeting at wide-area damping control of WAPS under both physical and cyber uncertainties, a learning-based networked control algorithm is presented. The problems of network imperfections and physical uncertainties are properly addressed through the model-free Q-learning based control algorithm. Besides, statistical analysis based control law is also designed to passively counteract the cyber uncertainties.

Considering the huge challenge of evaluating the proposed control methods on a real WAPS, the next research is more focused on the smaller system such as SPS and microgrids. Based on ZSG theory, a NDP based optimal control solution is proposed to solve the PPL accommodation problem of SPS with unknown system dynamics.

Next, a high-performance control scheme is proposed for the DC microgrids. The developed control algorithm is decentralized. Through a novel model transformation technique, the original output constrained model is transformed into an unconstrained one. By using the backstepping method, a voltage regulator is designed which can guarantee the transient tracking error always staying within user-defined time-varying bounds. At the meantime, the proper load sharing can be achieved as the output voltage converges.

Finally, in order to solve the control difficulties of inverter-interfaced microgrids such as the fast dynamics, uncertainties, and a wide range of operating conditions, two different control schemes are proposed. The proposed control solution can not only realize desired voltage and frequency regulation and also suppress the transient line current. By properly adjusting phase angles of bus voltages, both fair load sharing and variable uncertain operating conditions are addressed. The requirement of inter-subsystem communication is also not difficult to be realized with nowadays communication techniques.

REFERENCES

[1] C. Lu, Y. Zhao, K. Men and L. Tu, "Wide-area power system stabiliser based on model-free adaptive control," *IET Control Theory & Application*, vol. 9, no. 13, pp. 1996-2007, 2015.

[2] C.W. Taylor, D.C. Erickson, K.E. Martin, R.E. Wilson, and V. Venkatasubramanian, "WACS-wide-area stability and voltage control system: R&D and online demonstration," *Proceedings of the IEEE*, vol.93, no. 5, pp.892-906, 2005.

[3] A. Chakrabortty, "Wide-area damping control of power systems using dynamic clustering and TCSC-based redesigns," *IEEE Transactions on Smart Grid*, vol. 3, no. 3, pp. 1503-1514, 2012.

[4] J. Ma, T. Wang, and J. Wu, "Design of global power systems stabilizer to damp inter-area oscillations based on wide-area collocated control technique," on *IEEE Power and Energy Society General Meeting*, pp. 1-7, 2011.

[5] A. Chakrabortty, J.H. Chow, and A. Salazar, "A measurement-based framework for dynamic equivalencing of large power systems using wide-area phasor measurements," *IEEE Transactions on Smart Grid*, vol. 2, no. 1, pp. 68-81, 2011.

[6] F. Dorler, M.R. Jovanovic, M. Chertkov, and F. Bullo, "Sparsity-promoting optimal wide-area control of power networks," *IEEE Transactions on Power Systems*, vol. 29, no. 5, pp. 2281-2291, 2014.

[7] A. Chakrabortty and P.P. Khargonekar, "Introduction to wide-area monitoring and control," on *American Control Conference (ACC)*, pp. 6758-6770, 2013.

[8] N. Kishor, L. Haarla, J. Turunen, and M. Larsson, "Controller design with model identification approach in wide area power system," *IET Generation, Transmission & Distribution*, vol. 8, no. 8, pp. 1430-1443, 2014.

[9] J.B. Zhang, C.Y. Chung, and Y.D. Han, "A novel model decomposition control and its application to PSS design for damping inter-area oscillations in power systems," *IEEE Transactions on Power Systems*, vol. 27, no. 4, pp. 2015-2025, 2012.

[10] A.E. Leon, J.M. Mauricio, A. Gomez-Exposito and J.O. Solsona, "Hierarchical wide-area control of power systems including wind farms and FACTS for short-term frequency regulation," *IEEE Transactions on Power Systems*, vol. 27, no. 4, pp. 2084-2092, 2012.

[11] P. Kundur, *Power Systems Stability and Control*, McGraw-Hill, 1994.

[12] G. Andersson, *Dynamics and Control of Electric Power Systems.* Zurich, Switzerland: EEH- Power Systems Lab., ETH Zurich, 2012.

[13] N. Kishor, L. Haarla, J. Turunen, and M. Larsson, "Controller design with model identification approach in wide area power system," IET Generation, Transmission & Distribution, vol. 8, no. 8, pp. 1430-1443, 2014.

[14] N. Hui, G.T. Heydt and L. Mili, "Power system stability agents using robust wide area control," *IEEE Transactions on Power Systems*, vol. 17, no. 4, pp.1123-1131, 2002.

[15] X.Q. Xiao, F.F. Wang, and H.S. Zhao, "Application of self-triggered control in power system excitation control," International Conference on *Electrical and Control Engineering (ICECE)*, pp. 577 – 580, 2011.

[16] S. Wen, X.H. Yu, Z.G. Zeng, and J. J. Wang, "Event-triggering load frequency control for multi-area power systems with communication delays," *IEEE Transactions on Industrial Electronics*, vol. pp, no. 99, pp. 1-9 2015.

[17] W. Dib, R. Ortega, A. Barabanov, F. Lamnabhi-Lagarrigue, "A globally convergent controller for transient stability of multi-machine power systems using structure preserving models," *IEEE Transactions on Automatic Control*, vol. 54, no. 9, pp 2179-2185, 2009.

[18] E. Garcia and P. J. Antsaklis, "Model-based event-triggered control with time-varying network delays" IEEE Conference on Decision and Control and European Control Conference, pp. 1650-1655, 2011.

[19] S. Hu, X. Yin, Y. Zhang and E.G. Tian, "Event-triggered guaranteed cost control for uncertain discrete-time networked control systems with time-varying transmission delays". *IET Control Theory and Applications*, vol.6, no.8, pp.2793-2804, 2012.

[20] F.L. Lewis, D. Vrabie, and V. Syrmos, *Optimal Control*, 3rd edition, John Wiley and Sons, New York, 2012.

[21] F.L. Lewis, S. Jagannathan and A. Yesildirek, *Neural Network Control of Robot Manipulators and Nonlinear Systems*, Taylor & Francis, London, UK, 1999.

[22] A. Sahoo, H. Xu and S. Jagannathan, "Neural network-based event-triggered state feedback control of nonlinear continuous-time systems," *IEEE Transactions on Neural Networks and Learning Systems*, vol. 27, no. 3, pp. 497-509, 2016.

[23] F. Okou, L. A. Dessaint, and O. Akhrif, "Power systems stability enhancement using a wide-area signals based hierarchical controller," *IEEE Transactions on Power Systems*, vol. 20, no. 3, pp. 1465-1477, 2005.

[24] A. Chakrabortty and P.P. Khargonekar, "Introduction to wide-area monitoring and control," on *American Control Conference (ACC)*, pp. 6758-6770, 2013.

[25] S. Wang, X. Meng, and T. Chen, "Wide-area control of power systems through delayed network communication," *IEEE transactions on Control Systems Technology*, vol. 20, no. 2, pp. 495-503, 2011.

[26] C. Lu, X. Zhang, X. Wang, and Y. Han, "Mathematical expectation modeling of wide-area controlled power systems with stochastic time delay," *IEEE transactions on Smart Grid*, vol. 6, no. 3, pp. 1511-1519, 2015.

[27] Z. Wei, M.S. Branicky, and S.M Philips, "Stability of networked control systems," *IEEE Control System*, vol. 21, no. 1, pp. 84-99, 2022.

[28] J. L. Myers, A. Well, and R. F. Lorch, *Research Design and Statistical Analysis*, 3rd Edition, Routledge, 2010.

[29] P.J.G. Teunissen, *Dynamic Data Processing: Recursive Least-Squares*, VSSD, 2009.

[30] A.T. Asma, and A.K. Murad, "Model-free Q-learning designs for linear discrete-time zero-sum games with application to $\mathcal{H}\infty$ control," *Automatica*, vol.43, no.3, pp. 473-481, 2007.

[31] Power Systems Test Case Archive: Available: http://www2.ee.washington.edu/research/pstca/pf30/pg_tca30bus.htm

[32] H. Xu, Q. Zhao, and S. Jagannathan, "Finite-horizon near optimal output feedback neural network control of quantized nonlinear discrete-time systems with input constraint," *IEEE Transactions on Neural Network and Learning Systems*, vol. 26, no. 8, pp. 1776-1788, 2015.

[33] Performance of Three PSS for Inter-area Oscillations, Available: http://www.mathworks.com/help/physmod/sps/examples/performance-of-three-pss-for-interarea-oscillations.html

[34] Y. Xu, W. Zhang, W. Liu, and F. Ferrese, "Multiagent based reinforcement learning for optimal reactive power dispatch," *IEEE Transactions on Systems, Man, and Cybernetics, Part C: Applications and Reviews*, vol. 42, no. 6, pp. 1742-1751, November 2012.

[35] V. Salehi, B. Mirafzal, and O. Mohammed, "Pulse-load effects on ship power system stability," in *36th Annual Conference on IEEE Industry Electronic Society*, 2010, pp. 3353-3358.

[36] J. J. a. van der Burgt, P. van Gelder, and E. van Dijk, "Pulsed power requirements for future naval ships," in *12th IEEE International Pulsed Power Conference*, vol. 2, pp. 1357-1360, 1999.

[37] M. Falahi, K. L. Butler-Purry, and M. Ehsani, "Reactive power coordination of shipboard power systems in presence of pulsed loads," *IEEE Transactions on Power Systems*, vol. 28, no. 4, pp. 3675-3682, 2013.

[38] X. Feng, K. L. Butler-Purry, and T. Zourntos, "A multi-agent system framework for real-time electric load management in MVAC all-electric ship power systems," *IEEE Transactions on Power Systems*, vol. 30, no.3, pp. 1327-1336, 2015.

[39] F. Scuiller, "Study of a supercapacitor energy storage system designed to reduce frequency modulation on shipboard electric power system," in *38th Annual Conference on IEEE Industry Electronic Society*, pp. 4054-4059, 2012.

[40] J. P. Kelley, D. A. Wetz, and J. A. Reed, "The impact of power quality when high power pulsed DC and continuous AC loads are simultaneously operated on a microgrid testbed," *IEEE Electric Ship Technologies Symposium*, pp. 6-12, Apr. 2013.

[41] E. Cassimere, B., Valdez, and C. R., Sudhoff, "System impact of pulsed power loads on a laboratory scale integrated fight through power (IFTP) system," *IEEE Electric Ship Technologies Symposium*, pp. 176–183, 2005.

[42] J. M. Crider and S. D. Sudhoff, "Reducing Impact of Pulsed Power Loads on Microgrid Power Systems," *IEEE Transactions on Smart Grid*, vol. 1, no. 3, pp. 270–277, Dec. 2010.

[43] A. Yesildirak, F. L. Lewis, and S. Jagannathan, *Neural network control of robot manipulators and nonlinear systems*. New York: Taylor & Francis, 1999.

[44] T. Basar, and G. J. Olsder, *Dynamic Noncooperative Game Theory*, 2nd Ed. Philadelphia: Society for Industrial and Applied Mathematics, 1995.

[45] T. Basar, and P. Bernard, *H∞ Optimal Control and Related Minimax Design Problem*. Boston, MA: Nirkhauser, 1995.

[46] A. Al-Tamimi, F. L. Lewis, and M. Abu-Khalaf, "Model-free Q-learning designs for linear discrete-time zero-sum games with application to H-infinity control," *Automatica*, vol. 43, no.3, pp. 473-481, 2007.

[47] A. J. van der Schaft, "L2-gain analysis of nonlinear systems and nonlinear state feedback H-infinity Control," *IEEE Transactions on Automatic Control*, vol. 37, no. 6, pp. 770-784, 1992.

[48] K. G. Vamvoudakis and F. L. Lewis, "Online solution of nonlinear two-player zero-sum games using synchronous policy iteration," in *49th IEEE Conference on Decision and Control*, 2010, pp. 3040-3047.

[49] ESRDC report, "ESRDC ship notional baseline Medium Voltage Direct Current (MVDC) architecture thermal simulation and visualization," December. 2010. https://dspace.mit.edu/handle/1721.1/78666#files-area

[50] W.S. Im, C. Wang, L. Tan and W. Liu, "Cooperative controls for pulsed power load accommodation in a shipboard power system," *IEEE Transactions on Power System*, vol. 31, no. 6, pp. 5181-5189, 2016.

[51] Y. Diab, P. Venet, H. Gualous, and G. Rojat, "Self-discharge characterization and modeling of electrochemical capacitor used for power electronics applications," *IEEE Transactions on Power Electronics*, vol. 24, no. 2, pp. 501-517, 2009.

[52] T. Kim , H. Adeli , A. Stoica , and B.H. Kang, *Retraction Note to: Control and Automation, and Energy System Engineering*, vol 256(2017), Springer, Berlin, Heidelberg.

[53] L. Tan, Q. Yang, W. Im, C. Wang, and W. Liu, "Adaptive critic design based cooperative control for pulsed power loads accommodation in shipboard power system," *IET Generation, Transmission & Distribution*, vol. 10, no. 11, pp. 2739-2747, 2016.

[54] D. Bosich, G. Giadrossi, and G. Sulligoi, "Voltage control solutions to face the CPL instability in MVDC shipboard power systems," in *AEIT Annual Conference*, Trieste, Italy, Sept. 2014, pp. 1-6.

[55] P. Magne, B. Nahid-Mobarakeh, and S. Pierfederici, "Active stabilization of DC microgrids without remote sensors for more electric *aircraft*," *IEEE Transactions on Industry Applications*, vol. 49, no. 5, pp. 2352-2360, 2013.

[56] W. Su, and J. Wang, "Energy management systems in microgrid operations" *The Electricity Journal*, vol. 25, no. 8, pp. 45–60, 2012.

[57] Y. Chen, Y. Wu, C. Song, and Y. Chen, "Design and implementation of energy management system with fuzzy control for DC microgrid systems," *IEEE Transactions on Power Electronics*, vol. 28, no. 4, pp. 1563-1570, 2013.

[58] R. Balog, W. Weaver, and P. Krein, "The load as an energy asset in a distributed DC smart grid architecture," *IEEE Transactions on Smart Grid*, vol. 3, no. 1, pp. 253-260, 2012.

[59 L. Herrera, W. Zhang, and J. Wang, "Stability analysis and controller design of DC microgrids with constant power *loads*," *IEEE Transactions on Smart Grid*, Early Access, 2015.

[60] A. Tah and D. Das, "An enhanced droop control method for accurate load sharing and voltage improvement of isolated and interconnected DC microgrids," *IEEE Transactions on Sustainable Energy*, vol. 7, no. 3, pp. 1194-1204, 2016.

[61] A. Khorsandi, M. Ashourloo, and H. Mokhtari, "A decentralized control method for a low-voltage DC microgrid," *IEEE Transactions on Sustainable Energy*, vol. 7, no. 3, pp. 1194-1204, 2016.

[62] B. Fan, Q. Yang, K. Wang, J. Xu, and Y. Sun, "Transient stability enhancement control of power systems with time-varying constraints," *IET Generation, Transmission & Distribution*, vol. 10, no. 13, pp. 3251-3263, 2016.

[63] C. Christopoulos, and A. Wright, *Electrical Power System Protection*, Springer Science & Business Media, 1999

[64] T. Wu, Y. Chen, and Y. Huang, "3C strategy for inverters in parallel operation achieving an equal current distribution," *IEEE Transactions on Industrial Electronics*, vol. 47, no. 2, pp. 273-281, 2000.

[65] K. *Tan*, X. Peng, P. So, Y. Chu, and M. Chen, "Centralized control for parallel operation of distributed generation inverters in microgrids," *IEEE Transactions on Smart Grid*, vol. 3, no. 4, pp. 1977-1987, 2012.

[66] S. K. Mazumder, M. Tahir, and K. Acharya, "Master-slave current sharing control of a parallel dc-dc converter system over an RF communication interface," *IEEE Transactions on Industrial Electronics*, vol. 55, no. 1, pp. 59-66, *2008*.

[67] J. *Guerrero*, J. Vasquez, J. Matas, L. Vicuna, and M. Castilla, "Hierarchical control of droop-controlled AC and DC microgrids-A general approach toward standard," *IEEE Transactions on Industrial Electronics*, vol. 58, no. 1, pp. 158-172, 2011.

[68] A. *Khorsandi*, M. Ashourloo, H. Mokhtari, and R. Iravani, "Automatic droop control for a low voltage DC microgrid," *IET Generation, Transmission & Distribution*, vol. 10, no. 1, pp. 41-47, 2016.

[69] Y. Gu, X. Xiang, W. Li, and X. He, "Mode-adaptive decentralized control for renewable DC microgrid with enhanced reliability and flexibility," *IEEE Transactions on Power Electronics*, vol. 29, no. 9, pp. 5072-5080, 2014.

[70] A. *Emadi*, A. Khaligh, C. Rivetta, and G. Williamson, "Constant power loads and negative impedance instability in automotive systems: Definition, modeling, stability, and control of power electronic converters and motor drives," *IEEE Transactions on Vehicular Technology*, vol. 55, no. 4, pp. 1112-1125, 2006.

[71] M. Cupelli, M. Moghimi, A. Riccobono, and A. Monti, "A comparison between synergetic control and feedback *linearization* for stabilizing MVDC microgrids with constant power load," in *IEEE PES Innovative Smart Grid Technologies,* Istanbul, Turkey, Oct. 2014, pp. 1-6.

[72] M. Cupelli, M. Mirz, and A. Monti, "A comparison of backstepping and LQG control for stabilizing MVDC microgrids with *constant* power loads," in *2015 IEEE Eindhoven PowerTech*, Eindhoven, Netherlands, July 2015, pp. 1-6.

[73] K. Low, and R. Cao, "Model predictive control of parallel-connected inverters for uninterruptible power supplies," *IEEE Transactions on Industrial Electronics*, vol. 55, no. 8, pp. 2884 – 2893, 2008.

[74] P. Giesl, *Construction of Global Lyapunov Functions Using Radial Basis Functions*, Springer Berlin Heidelberg, 2007.

[75] M. Krstic, P. Kokotovic, and I. Kanellakopoulos, *Nonlinear and Adaptive Control Design*. John Wiley & Sons, Inc., 1995.

[76] S. Anand, B. Fernandes, and J. Guerrero, "Distributed control to ensure proportional load sharing and improve voltage regulation in low-voltage DC microgrids," *IEEE Transactions on Power Electronics*, vol. 28, no. 4, pp. 1900-1913, 2013.

[77] F. A. Salem and A. A. Rashed, "PID controllers and algorithms: selection and design techniques applied in mechatronics systems design," *International Journal of Engineering Sciences*, vol. 2, no. 5, pp. 191-203, 2013.

[78] W. Yao, M. Chen, J. Matas, J. Guerrero, and Z. Qian, "Design and analysis of the droop control method for parallel inverters considering the impact of the complex impedance on the power sharing," *IEEE Transactions on Industrial Electronics*, vol. 58, no. 2, pp. 576 – 588, 2011.

[79] J. Rocabert, A. Luna, F. Blaabjerg and P. Rodriguez, "Control of power converters in AC microgrids," *IEEE Transactions on Power Electronics*, vol. 27, no. 11, pp. 3353-3358, 2012.

[80] Y. Li, D. M. Vilathgamuwa, and P. C. Loh, "Design, analysis and real-time testing of controller for multibus microgrid system," *IEEE Transactions on Power Electronics*, vol. 19, no. 5, pp. 1195-1204, 2004.

[81] N. Pogaku, M. Prodanovic, and T. C. Green, "Modeling, analysis and testing of autonomous operation of an inverter-based microgrid," *IEEE Transactions on Power Electronics*, vol. 22, no. 5, pp. 613-625, 2007.

[82] D. E. Olivares, and A. M. Sani, "Trend in microgrid control," *IEEE Transactions on Smart Grid*, vol. 5, no. 4, pp. 1905-1919, 2014.

[83] J. Zhao, and X. Lyu, "Coordinated microgrid frequency regulation based on DFIG variable coefficient using virtual inertia and primary frequency control," *IEEE Transactions on Energy Conversion*, vol. 31, no. 3, pp. 833-845, 2016.

[84] H. Cai, G. Hu, F. L. Lewis, and A. Davoudi, "A distributed feedforward approach to Cooperative control of AC microgrid," *IEEE Transactions on Power Systems*, vol. 31, no. 5, pp. 4057-4067, 2016.

[85] D. He, D. Shi, and R. Sharma, "Consensus-based distributed cooperative control for microgrid voltage regulation and reactive power sharing," in *IEEE PES Innovative Smart Grid Technologies*, Europe, pp. 1-6, 2014.

[86] H. Xin, Y. Liu, Z. Qu, and D. Gan, "Distributed estimation and control for optimal dispatch of photovoltaic generations," *IEEE Transactions on Energy Conversion*, vol.29, no.4, pp.988-996, 2014.

[87] A. Maknouninejad, Z. Qu, F. Lewis, and A. Davoudi, "Optimal, nonlinear, and distributed designs of droop controls for DC microgrid," *IEEE Transactions on Smart Grid*, vol.5, no.5, pp.2508-2616, 2014.

[88] V. Nasirian, M. Modares, F. Lewis, and A. Davoudi , "Active loads of a microgrid as players in a deferential game," in *IEEE 7th International Symposium on Resilient Control Systems*, 2015, pp. 1-6.

[89] L. Fan, V. Nasirian, H. Modares, F. Lewis, Y. D. Song, and A. Davoudi, "Game-theoretic control of active loads in DC microgrids," *IEEE Transaction on Energy Conversion*, vol. 31, no. 3, pp. 882-895, 2016.

[90] L. Zhou, Y. Chen, A. Luo, J. M. Guerrero, and X. Zhou, "Robust two degrees-of-freedom single-current control strategy for LCL-type grid-connected DG system under grid-frequency fluctuation and grid-impedance variation," *IET Power Electronics*, pp, 1-19, 2016.

[91] M. Rasheduzzaman, J. A. Mueller, and J. W. Kimball, "An accurate small-signal model of inverter dominated islanded microgrids using dq reference frame," *IEEE Journal of Emerging and Selected Topics in Power Electronics*, vol. 2, no. 4, pp. 1070-1080, 2014.

[92] W. Guo, L. Mu, and X. Zhang, "Fault models of inverter-interfaced distributed generators within a low-voltage microgrid," IEEE Transactions on Industrial Electronics, pp. 1-9, 2016.

[93] V. Nasirian, Q. Shafiee, J. M. Guerrero, and F. L. Lewis, and A. Davoudi, "Droop-free distributed control for AC microgrid," IEEE Transactions on Power Electronics, vol. 31, no. 2, pp. 1600-1617, 2016.

[94] W. Zhang, Y. Xu, W, Liu, F. Ferrese, and L. Liu, "Fully distributed coordination of multiple DFIGs in a microgrid for load sharing," *IEEE Transactions on Smart Grid*, vol. 4, no. 2, pp. 806-815, 2013.

[95] W. Zhang, Y. Ma, W, Liu, S. Ranade, and Y. Luo, "Distributed optimal active power dispatch under constraints for smart grids," *IEEE Transactions on Industrial Electronics*, pp. 1-10, 2016.

[96] J. J. Slotine, and W. Li, Applied nonlinear control, Prentice-Hall Press, Englewood Cliffs, NJ, 1991

[97] C. T. Chen, *Linear System Theory and Design*, 3rd edition, Oxford University Press, New York, NY, 1999

[98] A. Bidram, A. Davoudi, F. L. Lewis, and J. M. Guerrero, "Distributed cooperative secondary control of microgrids using feedback linearization," *IEEE Transactions on Power Systems*, vol. 28, no. 3, pp. 3462-3470, 2013.

[99] A R. Khezri, S. Shokoohi, S. Golshannavaz, and H. Bevrani, "Intelligent over-current protection scheme in inverter-based microgrids," in *Smart Grid Conference*, Tehran, Iran, 2015, pp. 53-59.

[100] K. S. Narendra and S. Mukhopadhyay, "To Communicate or Not to Communicate: A Decision-Theoretic Approach to Decentralized Adaptive Control," in *2010 American Control Conference Marriott Waterfront*, Baltimore, USA, pp. 6369-6376, 2010.

VITA

Jiajun Duan

EDUCATION BACKGROUND

2014-2018: **Ph.D.**, **Electrical and Computer Engineering**, Lehigh University, GPA: 3.85
2013-2014: **M.Eng**, **Electrical and Computer Engineering**, Lehigh University, GPA: 3.80
2009-2013: **B.Eng**, **Power Systems and Automation**, Sichuan University (Honor College), GPA: 3.70

PROJECT & INTERNSHIP EXPERIENCE

Power Electronics and Microgrid Projects, SMRT-Lab, Lehigh University - *Research Assistant*
01/2015-present

- Developed an adaptive microgrid management systems. The secondary and primary controllers are designed in a decentralized way to realize proper load sharing and plug-and-play functions with unknown system parameters. The proposed control can guarantee the desired generation references of tertiary control to be fully achieved.
- Reduced the overshoot of transient voltage/current up to 30% for AC/DC microgrids with inverter-interfaced DGs based on advanced control designs. Performed the switch-level real time simulation using RT-Lab.
- Resolved the optimal coordinative control of energy storage system in shipboard power system by applying the Zero-Sum Game Theory. Accomplished both real time simulation and hardware-in-the-loop experiments.

16.5 MW PV System Project in MA, Conti Corp Inc. - *Associate Field Engineer*
05/2016-08/2016

- Collaborated in designing a hybrid PV panel deployment solution and reduced the total cost by over $9 million, with consideration of shading, power balancing and converter matching constraints.
- Managed and monitored timeline of the program. Worked with over 10 subcontracting companies to achieve the project milestones. Generated daily status report and presented to the leadership.
- Mapped over 70,000 barcodes including solar panels, inverters, and optimizers into 1,603 subsystem drawings with AutoCAD, and composed placed-in-order letters and safety reports.

Wide-Area Power System Project, CNet-Lab, TAMU-CC -*Visiting Scholar*
06/2015-02/2016

- Collaborated with faculties in TAMU-CC to develop the novel energy management system and low frequency oscillation damping control system for wide-area power systems against cyber-physical uncertainties.
- Aiming at reducing the communication and computation burden over 50%, while increasing the system robustness even with the packet drop rate and delay rate as high as 70%. Designed and implemented Reinforcement Learning, Optimal, Event-Triggering, and Adaptive control algorithms etc. into wide-area power systems.
- Performed the real time simulation of IEEE-14 bus, IEEE-30 bus and IEEE-118 bus systems using PowerWorld and RT-Lab to test the developed control algorithms.

Fault Location of Microgrid, Long-Lab, Lehigh University - *Research Assistant*
09/2013-01/2015

- Designed and developed a manageable DC microgrid testbed including a PV system, a wind turbine and a hydro turbine. Programed the control and monitor system using Labview.
- Independently revealed the approximated linear relation between the magnitude of transient voltage signals and the fault distance in single-phase micro-grids by using EMTP and MATLAB.
- Successfully developed an appropriate algorithm for fault location based on the newly discovered electrical characteristics with a fault location estimation error under 9%.

HONORS & CERTIFICATE

- "Best Graduate Student Teaching Assistant Award 2017" of Lehigh University
- Rossin Doctoral Fellows of Lehigh University 2017
- "Best Reviewers 2016 and 2017" of IEEE Transaction on Smart Grid (http://ieeexplore.ieee.org/document/7792798/)

U.S. PATENT & PUBLICATIONS

- One pending **U.S. patent** "Method and System for Fault Location in Single-phase Micro-grids" (LU103014-01).

1. **J. Duan,** C. Wang, H. Xu, Y. Xue and W. Liu, "Distributed control of inverter-interfaced microgrids based on consensus algorithm with improved transient performance," *IEEE Transactions on Smart Grid*, 2018.
2. **J. Duan,** H. Xu, and W. Liu, "Distributed control of inverter-interfaced microgrids with bounded transient line currents," *IEEE Transactions on Industrial Informatics*, 2018.
3. **J. Duan,** H. Xu, and W. Liu, "Event-triggered and self-triggered wide-area damping control designs under uncertainties," *Transactions of the Institute of Measurement and Control, 2017.*
4. **J. Duan,** H. Xu, and W. Liu, "Q-learning based damping control of wide-area power systems under cyber uncertainties," *IEEE Transactions on Smart Grid, 2017.*
5. **J. Duan,** H. Xu, and W. Liu, "Zero-sum game based control design for onboard pulsed power load and experiment with multiple converters," *IEEE Transactions on Industrial Informatics* (under review).
6. **J. Duan,** C. Wang, Q. Yang and W. Liu, "Decentralized high-performance control of DC microgrids," *IEEE Transactions on Smart Grid* (under review).
7. **J. Duan**, H. Xu and W. Liu, "A Fully Distributed Adaptive Control for Inverter-Interfaced Microgrids with Uncertain System Dynamics and Cyber Imperfections," (in preparation).
8. **J. Duan**, L. Cheng, and K. Zhang, "A novel method of fault location in single-phase microgrids," *IEEE Transactions on Smart Grid,* 2015.
9. W. Liang, K. Wu, Y. Xie and **J. Duan**, "TDCM: an IP watermarking algorithm based on two dimensional chaotic mapping," *Computer Science and Information Systems*, 2015.